Numerical modeling of turbulent flows in arbitrarily complex natural streams

A DISSERTATION

SUBMITTED TO THE FACULTY OF THE GRADUATE SCHOOL

OF THE UNIVERSITY OF MINNESOTA

BY

Seok Koo Kang

IN PARTIAL FULFILLMENT OF THE REQUIREMENTS

FOR THE DEGREE OF

DOCTOR OF PHILOSOPHY

Professor Fotis Sotiropoulos

August, 2010

Acknowledgements

I wish to thank my advisor, Professor Fotis Sotiropoulos, for not only giving me the opportunity to study at the Saint Anthony Falls Laboratory (SAFL), University of Minnesota, but also for his guidance and support throughout the course of my research. I would also like to thank Professors Christopher Paola, John S. Gulliver and Vaughan R. Voller for reviewing this dissertation and for their valuable feedback and discussion. This dissertation could not be completed without help of Dr. Anne Lightbody and Craig Hill who measured and processed the velocity and bed topography data in the Outdoor StreamLab. I am grateful to all former and present Computational Hydrodynamics and Biofluids research group members and friends at the SAFL. Funding for this research was provided by the National Science Foundation (NSF) grants EAR-0120914 (as part of the National Center for Earth-Surface Dynamics) and EAR-0738726. Computational resources were provided by the University of Minnesota Supercomputing Institute (MSI).

I wish to deeply thank Professor Tae Hoon Yoon at Hanyang University, Seoul, South Korea, who encouraged me to go abroad to do further studies.

I am grateful to all my family, in particular, to my wife, Seungwon Lim, for her love and support to me. Her unconditional support helped me complete my Ph.D. program earlier than I expected. I thank my little son, Jiwon Kang, for bringing happiness into my life. I am also grateful to my parents-in-law, Han Sung Lim and Hyun Joo

Jang, who respected my decision to study abroad. I thank my older brother, Kyung In Kang, for taking care of our parents while I was in USA and also for his support and encouragement from the other side of the Earth. Finally, I would like to express my deepest thanks to my parents, Sin Gak Kang and Soon Hee Ryu, for their endless support and encouragement. They raised my brother and me with love and sacrificed their lives for us. I am glad to graduate now, but at the same time I feel deep sadness and regret. My father, who had been eagerly looking forward to my graduation, passed away suddenly two months ago. One day in the spring of 2010 I had a video call with my father and talked to him that I was going to graduate soon, and he was very, very pleased with that news. I know he always had been missing and looking forward to seeing his son, daughter-in-law and grandson even though he never explicitly mentioned it to me. I also know he was very proud of his sons. I regret much that I never said I loved him. I wish my father knew how much my brother and I did love and care him. The fact that I will not be able to see him in the rest of my life truly breaks my heart. I miss him everyday.

Dedication

To my beloved mother and father.

My father, Sin Gak Kang, passed away suddenly on June 19, 2010 at the age of 60. He was always an active and industrious man full of passion.

ABSTRACT

An efficient and versatile numerical model is developed for carrying out high-resolution simulations of turbulent flows in natural meandering streams with arbitrarily complex, albeit fixed, bathymetry and instream hydraulic structures. The numerical model solves the three-dimensional, unsteady, incompressible Navier-Stokes and continuity equations in generalized curvilinear coordinates. This model can handle the arbitrary geometric complexity of natural streams by using the sharp-interface curvilinear immersed boundary (CURVIB) method. To enable efficient simulations on grids with tens of millions of nodes in long and shallow domains typical of natural streams, the algebraic multigrid method (AMG) is used to solve the Poisson equation for pressure. Free-surface is treated either with the rigid-lid approach or modeled using a two-phase flow approach implemented using level-sets. Depending on the desired level of resolution and available computational resources, the numerical model can either simulate turbulence via direct numerical simulation (DNS), large-eddy simulation (LES) or unsteady Reynolds-averaged Navier-Stokes (URANS) simulation. The numerical model is validated by simulating several test cases for which good quality laboratory data or benchmark simulations are available in the literature. The potential of the model as a powerful tool for simulating energetic coherent structures in turbulent flows in natural river reaches is demonstrated by applying it to carry out LES and URANS simulations in a field scale natural-like meandering stream, Outdoor StreamLab, at resolution sufficiently fine to capture vortex shedding from cm-scale roughness elements on the bed. Comparisons between the simulated mean velocity and turbulence kinetic energy fields with field-scale measurements are reported and show that the numerical model can capture all features of the measured flow with high accuracy. Furthermore, the simulated flowfields

are analyzed to elucidate the multi-faceted physics of the flow in a natural stream with pool-riffle sequences and to uncover the underlying physical mechanisms. The simulations provide new insights into the role of large-scale roughness in flow through riffles and elucidate the three-dimensional structure, interactions and governing mechanisms of the inner and outer bank secondary flow cells and recirculation zones in the pools. Moreover, the simulations underscore the role of turbulence anisotropy throughout the stream and suggest important links between stream hydrodynamics and morphodynamics. Calculations are also carried out for the same meandering stream with an instream structure installed along its outer bank to demonstrate the utility of the model as a powerful tool for developing science-based design guidelines for stream restoration.

Table of Contents

List of Tables

List of Figures

Chapter 1

Introduction

Efforts to stabilize and restore streams and rivers across the nation have grown dramatically in the last fifteen years, with over $1 billion spent every year since 1990 (Bernhardt et al., 2005). The commonly stated goals for river restoration in the United States are to enhance water quality, manage riparian zones, improve instream habitat for fishes, and prevent streambank erosion (Bernhardt et al., 2005). A rather common strategy to stream restoration involves the installation of a wide variety of instream hydraulic structures, which act to modify the local hydrodynamics in a way that facilitates the satisfaction of these stream-restoration goals. The development of effective and long-lasting strategies for installing and operating such structures, however, is far from trivial. This is because the complex interactions among turbulence, sediment transport, biota and hydrological processes in natural streams with complex instream structures are far from being fully understood. Even though stream restoration efforts have been underway for well over fifty years, few stream restoration techniques have been thoroughly evaluated (Roni et al., 2002), and existing design guidelines for instream structures are usually vague and ineffective. Such guidelines rely largely on ad-hoc and subjective criteria (Gray and Sotir, 1996) or on grossly simplified descriptions of the underlying flow

physics (e.g. cross sectionally averaged values of the shear stress) (Li and Eddleman, 2002; Fischenich, 2003) rather than in-depth physical understanding of the highly unsteady and three-dimensional mechanisms via which a given instream structure alters the flow and transport processes in the stream (Johnson et al., 2002b). As a result, the stream restoration practice today is more of a highly empirical art than science. It is presumably due to the lack of a science-based approach to stream-restoration that more than half of stream restoration projects ultimately fail (O'Neil and Fitch, 1992). Therefore, critical prerequisite for developing effective stream restoration strategies and improving existing design methods is to understand the complex flow phenomena occurring around real-life instream structures in a natural stream.

In the following sections previous works on studying flow patterns in a natural meandering stream are reviewed and subsequently stream restoration methods using instream structures are presented. These are followed by discussion of the challenges such flows pose to numerical methods and a comprehensive review of previous efforts to simulate numerically turbulent flows in complex natural streams. Finally, the objectives of the present research are presented.

1.1 Flow patterns in meandering streams

The objective of this section is to provide a thorough description of meander bend hydrodynamics in nature as it emerges from previous field studies, laboratory experiments and numerical simulations. Meandering channels in nature consist of pool-riffle sequences (Keller, 1972; Thompson, 1986), which are the manifestation of rich morphodynamics emerging from the complex interaction of the turbulent flow with the streambed material. Riffles are typically shallow straight segments characterized by large water surface slopes, high velocities, and intense turbulent mixing. Pools, on the other hand, are

characterized by larger flow depth, slower overall velocities and could exhibit significant longitudinal and transverse bathymetry gradients. The morphologic complexity of meandering streams gives rise to highly three-dimensional flows dominated by energetic coherent vortices, secondary flows, shear layers, regions of recirculation and flow stagnation, and pockets of highly non-isotropic turbulent stresses. It is presumably because of such complex flow phenomena and their poorly understood interactions with mobile streambeds that the underlying mechanisms that govern the formation of meanders in nature are still not entirely understood and cannot be fully explained by a single unifying theory (Leopold and Wolman, 1960; Dietrich et al., 1979; Frothingham and Rhoads, 2003). Yet understanding these mechanisms is critical prerequisite for developing physics-based approaches for stabilizing stream banks and restoring waterways.

One of the most important and well-known characteristics of flow through a meandering bend is the curvature-induced transverse secondary motion that develops within the bend as the result of the imbalance of the centrifugal force and the transverse pressure gradient near the bed (Humphrey et al., 1981; Johannesson and Parker, 1989). This imbalance sets up a streamwise coherent vortical structure, widely known in the open channel literature as the inner-bank cell, whose sense of rotation is such that it directs surface flow toward the outer bank and near-bed flow toward inner bank. The inner bank cell has been studied extensively for well over a century due to its importance in redistributing momentum and transporting scalars (e.g. temperature) and sediments within the stream and its major role in determining stream morphodynamics (Thomson, 1876; Kalkwijk and de Vriend, 1980; Dietrich and Smith, 1983; Johannesson and Parker, 1989; Frothingham and Rhoads, 2003). Thomson (1876), for instance, was the first to explain theoretically the occurrence of sediment deposition at the inner bank of the bend by linking this phenomenon to the inner bank cell and its propensity to transport sediment from the outer to the inner banks along the bed. Kalkwijk and

de Vriend (1980) developed a mathematical model describing primary and secondary flow velocities in wide and mildly curved open channel bends while Johannesson and Parker (1989) developed a theoretical model for the calculation of secondary flow in mildly sinuous channels. Dietrich and Smith (1983) studied the influence of the point bar on the flow in meander bends and found that its presence significantly modifies the flow patterns and the balance of the underlying hydrodynamic forces. They found the commonly assumed secondary flow pattern in the meander bend, which is outward flow at the surface and inward flow near the bed, does not occur over the entire cross section and there is an outward flow over the top of the point bar. Frothingham and Rhoads (2003) studied the three-dimensional flow structure and streambed change in an asymmetrical, compound meander loop by field investigation. They found that the helical mean flow motion associated with the inner bank cell decays rapidly as the flow moves toward inflections in curvature and that no mean streamlines complete a full cycle of helical rotation within a lobe.

The counter-clockwise rotating inner bank cell is often accompanied by a smaller transverse secondary motion cell that rotates in the opposite direction and is located near the corner region between the water surface and the outer bank (Bathurst et al., 1979; Thorne et al., 1985). This cell is known as the outer bank cell and even though smaller and generally weaker than its inner bank counter part it is an important feature of meander bend flows as it can affect bank erosion processes by altering the streamwise velocity and boundary shear stress distributions. The outer bank secondary cell has also been the subject of extensive research through field investigations (Hey and Thorne, 1975; Bathurst et al., 1979; Thorne et al., 1985), laboratory experiments (Blanckaert and de Vriend, 2004) and numerical simulations (Balen et al., 2009; Stoesser et al., 2010). Hey and Thorne (1975) was among the first to observe that in natural

rivers there exist two counter-rotating secondary cells inducing water surface flow convergence, which gives rise to a vertical flow directed from the surface toward the bed and causes channel deepening. Subsequently Bathurst et al. (1979) and Thorne et al. (1985) further reinforced the existence of the outer bank secondary cell in field studies. Thompson (1986) investigated flow in a meandering gravel-bed stream and observed a zone of upwelling adjacent to the outer bank of the stream and inward flow along the water surface towards a zone of convergence over the deepest part of the pool. To investigate the physical mechanisms that give rise to the outer bank cell in meander bends, Blanckaert and de Vriend (2004) carried out detailed laboratory experiments in a prismatic open channel bend at resolution sufficiently fine to calculate the various terms in the budget of mean streamwise vorticity and turbulence kinetic energy equation. They found that both the gradients of the cross-stream turbulent stresses and the centrifugal force contribute to the formation of the outer bank cell. Balen et al. (2009) carried out large-eddy simulation (LES) to simulate the flow in a curved flume with rectangular cross section and confirmed that cross-stream turbulent stresses and centrifugal force play an important role in the formation of the outer bank cell. They also observed that the outer bank cell generates a pocket of increased turbulence kinetic energy (TKE) and TKE production. Stoesser et al. (2010) employed both LES and RANS with an isotropic turbulence closure to simulate the flow in a prismatic curved bend. They reported the RANS simulation failed to predict the outer bank cell, which further reinforces the conclusion that turbulence anisotropy is a key contributor to the formation of the outer bank cell in curved open channels. In summary, the aforementioned studies make a strong case that the formation of the outer bank cell is driven by the combined effects of the centrifugal force and the anisotropy of turbulence. In spite of these important studies, however, the physics of the outer bank cell is, relative

to its inner bank counter part, not as well understood. This is especially true in natural meander bend geometries for which neither experiments nor simulations have been reported with resolution sufficiently fine to resolve the underlying physical phenomena and mechanisms with clarity.

Another interesting phenomenon occurring in natural meander bend flows, which has not been studied as widely as the inner and outer bank cells, is the occurrence of flow separation at the inner bank of the bend. Several previous studies have observed occurrence of flow separation at the inner bank of natural or laboratory bends (Bagnold, 1960; Leopold et al., 1960; Leeder and Bridges, 1975; Nanson, 1980; Schmidt, 1986; Rubin et al., 1990). Bagnold (1960) argued that flow separation occurs at the inner bank of the meander bend during the development of the bend creating deposition at the inner bank and its intensity reaches maximum for $r_m/w \simeq 2.0$, where r_m is the radius of curvature of the mid-stream line and w is the width of the channel. Leeder and Bridges (1975) investigated flow separation in meander bends and related its occurrence to the bend tightness (r_m/w) and the Froude number. Rubin et al. (1990) observed recirculation zones and formation of bars in the Colorado River in a Grand Canyon and observed that deposition is focused at the separation point, reattachment point, recirculation eddy center, or along the shear surface that separates the recirculation zone from the faster moving flow in the main channel. Schmidt (1990) studied the formation of flow separation in the vicinity of a debris fan in the Colorado River in the Grand Canyon and found that recirculation zones increase in length with increasing discharge and that sand bars form beneath recirculation zones, especially near the separation and reattachment points. They also observed that the form and location of bars is consistent with the location and behavior of stagnation points in the river. Therefore, all previous field and laboratory studies indicate that flow separation occurring at the inner bank of the bend has a profound impact on meander morphodynamics as it is linked with the

formation of bars at the inner bank of the bend.

1.2 Stream restoration practice

To control sedimentation, protect bank erosion or increase flow diversity in natural streams, engineers commonly install instream structures such as rock vanes, root wads, bendway weirs, etc. (Rosgen, 2001; Harman et al., 2001; Johnson et al., 2002a). Such structures increase the complexity of the hydrodynamic environment within the stream and make the development of design guidelines based on scientific understanding of the underlying flow physics a rather challenging undertaking. In this section we present and discuss the function of some of the most commonly used instream structures.

Rock vanes are single-arm rock structures placed to extend out from a streambank into the flow (Sotiropoulos et al., 2009). Figure 1.1 shows the rock vane installed at the St. Anthony Falls Laboratory (SAFL) Outdoor StreamLab. They gradually slope from the bank into the bed in a way that the tip is submerged but other sections are exposed and they are placed at an angle with regard to the oncoming flow. Rock vanes are typically installed along the outer bank and designed to direct oncoming flow away from the bank in order to create quiescent local flow conditions to mitigate erosive flow patterns by reducing the bed shear stress along the streambank (Maryland Department of the Environment, 2000; Harman et al., 2001). Scour pools formed behind the rock vanes can aid aquatic habitat by creating flow diversity. Rock vanes also deflect the oncoming high speed flow from the bank and dissipate energy. The flow is directed toward the center of the channel and quiescent flow conditions are created near the bank (Johnson et al., 2002a). It is recommended by Johnson et al. (2001) that a series of vanes in the streamwise direction are required to create a secondary flow cell, which creates scour at the middle of the channel and effectively relocates erosive flow patterns induced by channel curvature.

J-hook vanes (Figure 1.2) are modified rock vanes which are composed of a rock vane with additional boulders placed at the tip of the vane in a hooking pattern with gaps

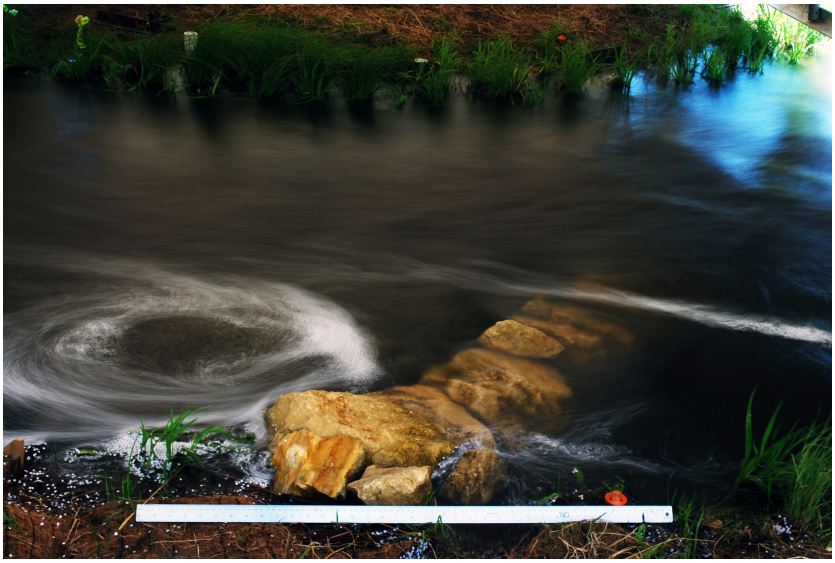

Figure 1.1: A rock vane installed at the SAFL Outdoor StreamLab (the flow direction is from right to left; flow is visualized by tracers, which show formation of a recirculation zone and a shear layer around the rock vane).

between them (Sotiropoulos et al., 2009). According to Rosgen (2001), the vane portion of the structure occupies 1/3 of the bankfull width of the channel near the channel banks, while the hook occupies 1/3 of the width at the center. The attached hook is known to create aquatic habitat, to increase energy dissipation (Harman et al., 2001; Rosgen, 2001) and to provide a longer, deeper and wider scour pool than that created by rock vanes only (Rosgen, 2001). This is an important function of such structures since the flow separation zones at the center of the channel, where upwelling and downwelling currents are found, are believed to provide excellent habitat for trout (Rosgen, 2001).

Cross vanes (Figure 1.3) are another variation of the rock vanes having dual-arm rock structures made by connecting the tips of two rock vanes from opposite banks with rocks arranged perpendicular to the flow (Sotiropoulos et al., 2009). Cross vanes primarily function as grade control structures while still providing a reduction in near-bank shear stress (Rosgen, 2001; Doll et al., 2003). They act to create a high velocity core and two

Figure 1.2: A J-hook vane installed at the SAFL indoor flume (the flow direction is from left to right; image courtesy of Craig Hill).

flow separation zones at the center of the channel and near the streambanks, respectively. Cross vanes also create scour pools in their wake. They are normally installed within a section of little or no turbulence for larger streams or at the head of a riffle for smaller streams (Doll et al., 2003).

Bendway weirs (Figure 1.4) are rock structures that are nearly flat across their length, extend from the bank into the channel center, and fully submerged for bankfull flows (Sotiropoulos et al., 2009). Bendway weirs are known to relocate the erosive flow patterns from the vulnerable outer bank toward the center of the channel (Derrick, 1998) by altering transverse helical flow motions associated with channel meanders and deflecting flow away from the outer bank. Bendway weirs usually are used in larger meandering rivers and tend to perform well in high-flow conditions but have also been observed to function effectively in low-flow conditions (Derrick, 1998; Abad et al., 2008).

All of the above mentioned structures are designed to direct flow away from the banks, dissipate flow energy, protect streambanks from erosion and scour, promote the

Figure 1.3: A cross vane installed at the SAFL indoor flume (the flow direction is from left to right; image courtesy of Craig Hill).

Figure 1.4: Bendway weir installed at the SAFL indoor flume (the flow direction is from left to right; image courtesy of Craig Hill).

development of sustainable aquatic habitat, and increase habitat diversity (Kauffman et al., 1997). They are preferred by many federal, state, and local governmental agencies to assist in stabilizing beds and banks in stream restoration projects (Johnson et al., 2002b). However, evaluation of performance of those structures was based either on the field monitoring (Harman et al., 2001) or simple flume experiments estimating scour depth around structures (Johnson et al., 2002a). In-depth studies of the three-dimensional flow field and turbulence characteristics induced by such structures have yet to be carried out. Furthermore, evaluation of such structures based on field monitoring or simple flume experiment can be challenging since their performance is highly site-specific and may vary significantly from site to site and under different flow conditions. Besides, and as recent work has shown, flows past complex hydraulic structures are highly three-dimensional and dominated by energetic and dynamically rich coherent structures induced by site-specific geometric complexities and associated large-scale flow instabilities (Devenport and Simpson, 1990; Martinuzzi and Tropea, 1993; Ge and Sotiropoulos, 2005; Paik and Sotiropoulos, 2005). The physical mechanism that govern the interaction of instream structures with turbulence, sediments, and the free-surface are have yet to be understood. As a result, the performance of such structures in of a stream restoration projects is difficult to predict a priori and one must rely on long-term posteriori field monitoring to ultimately assess success or failure over time.

A key characteristic of flows past stream restoration structures is the emergence of a wide range of large-scale, energetic vortical structures ranging from large-scale, slowly evolving eddies in regions of recirculation and flow stagnation to energetic shear layers, tornado and whirlpool type vortices, horseshoe vortices, and curvature-induced streamwise vortices. Experimental and computational studies (Devenport and Simpson, 1990; Paik and Sotiropoulos, 2005; Paik et al., 2007; McCoy et al., 2008; Paik et al., 2010) have shown that slowly evolving, large-scale vortical structures can be the primary

mechanism for producing turbulence in flows past wall-mounted hydraulic structures. Devenport and Simpson (1990), for instance, found that the velocity fluctuations in the vicinity of the large-scale turbulent horseshoe vortex (THSV) developing at the upstream junction of a bed-mounted wing-shaped pier exhibit bimodal probability density functions. They also found that these bimodal velocity fluctuations produce a pocket of turbulent stresses in the junction region larger by one order of magnitude than the turbulent stresses produced in the upstream turbulent boundary layer. The details of the instability mechanism that gives rise to the rich dynamics of the THSV were studied by Paik et al. (2007). Paik et al. (2007) also who argued that the growth of hairpin vortices is the result of centrifugal instability of the flow that originates at the outer turn of the THSV between the vortex and the wall. Another example of the complexity of flows past instream structures was reported in the numerical work of Paik and Sotiropoulos (2005) who simulated turbulent flow past a straight rectangular block mounted perpendicularly to the side of a shallow open channel. They showed that such flows are characterized by a wide range of time scales, ranging from high frequency vortex shedding from the edge of the obstacle to the slowly evolving eddies in the recirculating zone downstream of the obstacle. A striking finding of this work was with regard to the complexity of the flow in the recirculating region that develops upstream of the obstacle. Paik and Sotiropoulos (2005) showed that this region is dominated by multiple and highly energetic eddies and is energized by aperiodic vorticity entrainment from the shear layer that delineates the recirculating zone from the fast moving outer flow occurring at the unstable saddle point of attachment at the upstream face of the obstacle. In a more recent study, Paik et al. (2010) studied the flow past a similar wall-mounted block but in a significantly deeper flow. They found that the flow in the upstream recirculating region in this case is dominated by an intricate web of highly three-dimensional vortices with axes perpendicular and parallel to the bed. Vortical structures generated near

the bed were found to rise to the surface aperiodically causing surface-boil like events that manifested themselves as a source-like flow directed upstream from the upstream obstacle wall.

As follows from the above literature review, all insights into the dynamics of coherent structures in flows past instream structures have been derived from numerical simulations and experiments carried out in straight laboratory flumes of simple cross sectional geometry. Therefore, little is known today about the the flow environment instream structures will induce when mounted in natural meander bends of arbitrarily complex bathymetry. Given the enormous geometric complexity of the problem and the difficulties in carrying out high-resolution measurements in natural waterways, numerical simulation provides the only viable tool for elucidating the physics of such flows at the level of detail needed to enable science-based approaches to stream restoration. In the following section we provide an overview of the challenges for numerical methods and review the state-of-the-art in numerical simulations of turbulence in open channels and natural river reaches.

1.3 Challenges for numerical modeling of turbulence in natural waterways

A major challenge in modeling flows in natural streams arises from the geometric complexity of the flow domain. Natural streams and rivers are characterized by arbitrary geometric complexity that spans a wide range of scales: from the scale of a reach of a stream or river meander, to the scale of transverse bathymetric variabilities, down to the scale of boulders, small rocks, and sand grains typically found in river beds. The presence of natural and/or man-made structures, such as riffles and pools, tree trunks, root wads, bridge foundations and stream restoration structures, and dynamically evolving boundaries (water surface and erodible bed) further add to the difficulty of the problem. In order to correctly capture complex flow physics occurring in the real-life streams, it is essential to have a numerical model which is able to handle all underlying geometric complexities. Several numerical methods have been developed in order to simulate flows in highly complex geometries, which will be discussed in Section 1.4.

Modeling difficulties are especially exacerbated when one is interested in resolving directly, rather than modeling with statistical approaches, the dynamics of energetic coherent vortical structures that dominate flows in natural waterways. Due to the enormous geometric complexity of natural waterways and the wide variability of spatial and temporal scales of the various coherent structures, accurate numerical simulations require fine computational meshes, small time steps and turbulence models that are able to resolve dynamically rich coherent structures. For the most part, and as the subsequently presented review of related literature will show, statistically stationary models using the Reynolds-averaged Navier-Stokes (RANS) equations have been the models of choice in previous numerical simulations. Only recently, coherent-structure resolving models, such as unsteady RANS and LES, have started making a mark in

the field. Even so application of such models has for the most part been restricted to simple laboratory flumes since numerical methods that will facilitate their application to natural waterways do not exist today.

Central to the development of a scientific approach to stream restoration is the in-depth understanding of turbulent flow and transport processes in natural streams at restoration-relevant scales: from the reach scales (order of tens of meters or even kilometers) and the scale of a given instream (order of meters), which determine large scale hydrodynamics and morphodynamics, to flow scales that are relevant to instream aquatic biota (order of cm or even mm). Along the same lines, there is a large disparity in the time scales of such flows, which could range from a fraction of a second for energetic vortical structures and shear layers, which are actively involved in scouring of the streambed, to tens of minutes in slowly evolving recirculating regions, where fish like to gather and spawn. All these spatial and temporal scales are important to enable a science-based approach to stream restoration and need to be resolved by the numerical model. In order to resolve such multi-scale flow dynamics, one needs to use spatial and temporal increments which are sufficiently fine to resolve the smallest and fastest coherent structures of interest throughout the entire computational domain, which is as large as the size of the reach of the streams or river of interest. To accomplish this objective, especially at Reynolds numbers of practical interest, the total number of grid nodes required to discretize the computational domain can be in the order of tens or even hundreds of million points. Therefore, critical prerequisite for being able to perform such simulations is the development of fast numerical algorithms which can efficiently solve the Navier-Stokes equations in massively parallel supercomputers is necessary to be able to do such simulations.

A major challenge for carrying out such high-resolution reach-scale, coherent structure resolving simulations of turbulence in natural waterways stems from the large

aspect-ratio of the resulting computational domains due to the large disparity among the flow depth and the streamwise and lateral dimensions of the reach. Large domain and grid cell aspect-ratios induce numerical stiffness and could dramatically deteriorate the convergence rate of iterative solvers for linear systems of equations. Therefore, unsteady flow simulations on fine computational grids in large-aspect ratio domains can be plagued by such numerical stiffness, rendering numerical simulations within reasonable computational times unlikely if not impossible even on powerful, massively parallel computational platforms.

Numerical modeling of flows in natural waterways is further complicated by the presence of the moving boundaries such as free-surface and deformable bed. free-surface, for instance, in low Froude number flows (or subcritical flows) is often approximated as a flat rigid surface using the rigid-lid approximation (Mcguirk and Rodi, 1978). However, the Froude number of flows within natural waterway could vary significantly due to the presence of the irregular bed topography and arbitrarily complex hydraulic instream structures. The rigid-lid approximation is inadequate for modeling supercritical or transcritical free-surface flows with the high water surface slope. Modeling of the morphodynamics interacting with the flowfields in a natural stream presents yet another major challenge. The scales of the bed motion vary from fast moving bed forms to slowly evolving large scale scour and deposition patterns such as the pool, channel thalweg and point bars found in natural meanders. Another difficulty stems from the fact that the sediment moves both in suspension and bedload. Wide range of grain sizes in natural sediments increases the complexity of the problem because it requires multiple sediment transport modeling both for transport of suspended sediment and bedload.

The above mentioned difficulties are daunting and render attempts to simulate turbulence in natural aquatic environments a rather challenging undertaking for even the

most advanced numerical methods available today. In what follows, we present an overview of various numerical approaches for simulating arbitrarily complex geometries and subsequently we discuss previous work on numerical modeling of turbulent flows in open channels and natural waterways.

1.4 CFD methods for treating complex geometry

Several numerical methods have been proposed in the literature to solve three-dimensional incompressible flows in complex computational domains. One widely used approach is to employ boundary-fitted, generalized curvilinear grids. In such methods, a complex domain is transformed into a simple rectangular domain through a generalized coordinate transformation. These methods have been mostly used in conjunction with the finite difference or finite-volume methods in order to solve incompressible Navier-Stokes equations (Chen et al., 1990; Rosenfeld et al., 1991; Zang et al., 1994; Meselhe and Sotiropoulos, 2000; Felten and Lund, 2006) and work well for relativity simple, singly-connected computational domains. Chen et al. (1990) solved Reynolds-averaged Navier-Stokes equations under nonorthogonal body-fitted coordinates using a modified SIMPLER algorithm (Patankar, 1980). They demonstrated the performance of the method by calculations of the flow over a typical ship hull. Rosenfeld et al. (1991) solved lid-driven flow in a polar cavity, flow around a circular cylinder and flow through a curved duct. They obtained reasonable agreement between computations and measurements. Sotiropoulos and Patel (1994) calculated the three-dimensional turbulent flow through a circular-to-rectangular transition duct using Reynolds-stress closure in generalized curvilinear coordinates. The computed streamwise velocity and vorticity fields were in good agreement with the measurements. Yoon and Patel (1996) developed a two-dimensional numerical model based on solution of the RANS equations and the $k-\omega$ turbulence model and generalized coordinates to describe the flow in a fixed dune-bed channel. The model predictions were in good agreement with existing experimental data. Sotiropoulos and Ventikos (1998) solved RANS equations in generalized curvilinear coordinates with an artificial compressibility approach and calculated the flow through a 90° rectangular duct by employing standard isotropic and nonlinear two-equation turbulence closures. They demonstrated that near-wall, non-isotropic,

two-equation models offer a promising alternative to Reynolds-stress transport closures for predicting complex shear flows of engineering interest. Jordan (1999) developed a LES model under generalized curvilinear coordinates and applied the model in order to solve turbulent flow around a cylinder. Hodges and Street (1999) solved turbulent free-surface flows by using the body-fitted boundary orthogonal grids. They employed the arbitrary Lagrangian-Eulerian (ALE) in conjunction with curvilinear body-fitted grids to handle the deformation of the free-surface. Meselhe and Sotiropoulos (2000) solved turbulent free-surface flow in a curved open channel by using the $k - \varepsilon$ RANS model under generalized curvilinear coordinates. They determined the free-surface elevation by allowing the computational mesh to deform during the iterative solution procedure so that the proper kinematic and dynamic conditions are satisfied at convergence. The aforementioned curvilinear grid methods have been successfully used to handle moderate levels of geometric complexity, such as those associated with channels of simple cross section without complex embedded structures However, a major shortcoming of these methods is that they are inherently limited to relatively simple geometries as they are difficult to apply to multi-connected computational domains.

Unstructured grid methods, on the other hand, can handle higher levels of geometric complexity than the structured (or body-fitted) grid counterpart. These methods have been used in conjunction with finite volume (Zhang et al., 2002; Mahesh et al., 2004; McCoy et al., 2008; Kirkil et al., 2008; Koken and Constantinescu, 2009) or spectral/finite element methods (Chu and Karniadakis, 1993; Henderson and Karniadakis, 1995; Karamanos and Karniadakis, 2000; Dong et al., 2006). Mahesh et al. (2004), for instance, developed a LES framework by using finite volume method with three-dimensional unstructured grids. They carried out LES for solving turbulent flow in a coaxial combustor which has highly complex geometry and obtained good agreement between computations and measurements. The same method was later extended by

Constantinescu and co-workers to carry out LES of flows in open-channel geometries with hydraulic structures (McCoy et al., 2008; Kirkil et al., 2008; Koken and Constantinescu, 2009). Chu and Karniadakis (1993), on the other hand, carried out direct numerical simulations (DNS) of laminar and turbulent flow over riblet-mounted surfaces using the spectral element method in order to investigate the drag reduction effect by V-groove riblets, and they revealed complex flow physics around the riblet. Dong et al. (2006) investigated development of shear-layer instabilities in the near wake of a cylinder at different Reynolds numbers by carrying out DNS using the spectral element method. Unstructured grid methods can be very attractive since they can in principle handle any level of geometric complexity. However, the generation of three-dimensional unstructured mesh for arbitrarily complex geometries is not trivial and can be very time consuming. Moreover, unstructured grid methods are typically computationally less efficient than the structured grid methods because they require much larger computer memory for storing grid connectivity information. This is not a trivial to solve when one is interested in solving a problem with tens or hundreds of millions of unknowns. It is presumably because of such difficulties that the open channel simulations reported by McCoy et al. (2008) and Kirkil et al. (2008), who employed the model of Mahesh et al. (2004), have been restricted to relative coarse meshes with about 4×10^6 nodes.

An alternative to unstructured grid and structured curvilinear grid methods is the overset grid approach (Tang et al., 2003; Ge and Sotiropoulos, 2005; Paik and Sotiropoulos, 2005). In this approach, a complex geometric configuration is decomposed into a set of simpler, overlapping subdomains, each designed so that it can be easily discretized with a set of simple, boundary-conforming, curvilinear coordinates. Tang et al. (2003) developed an overset grid framework that solves unsteady, three-dimensional incompressible flows in complex geometries using the finite-volume method with the

dual time-stepping artificial compressibility approach. They proposed a new interpolation scheme other than the trilinear interpolation which minimizes non-physical spurious oscillations in the overlap region and is less sensitive to grid refinement. Ge and Sotiropoulos (2005) employed body-fitted, chimera overset grids in conjunction with a grid-embedding strategy to discretize arbitrarily complex, multi-connected flow domains around an actual bridge foundation embedded in a stretch of the Chattachochee River near Cornelia, Georgia, USA. Paik and Sotiropoulos (2005) employed multiple overset grids to discretize flow domains around a rectangular block mounted to the side of a rectangular open channel and investigated three-dimensional turbulent flow structures near the block by carrying out the detached eddy simulation (DES) approach. The same approach has also been used to simulate flows past wing-shaped and cylindrical piers mounted on a flat bed (Paik et al., 2007; Escauriaza and Sotiropoulos, 2010), cube-shaped roughness elements on a flat bed (Paik et al., 2010), and a rectangular block mounted on the side of a straight open channel with mobile bed but with the bed shape frozen at its final equilibrium shape. Compared to their unstructured grid counterpart, composite structured grid algorithms simplify the implementation of high-resolution discretization schemes and allow for efficient clustering of grid surfaces near solid walls, thus, enhancing accuracy in high Reynolds-number simulations. However, the degree of geometric complexity that the overset grid methods can handle is still limited because they employ body-fitted grids for each overset block. In addition, grid generation is often cumbersome and time consuming especially for arbitrarily complex geometries.

Recently, sharp-interface immersed boundary (SIB) methods have become very popular for simulating flows in arbitrarily complex, multi-connected domains with moving immersed boundaries (Iaccarino and Verzicco, 2003; Gilmanov and Sotiropoulos, 2005; Ge and Sotiropoulos, 2007; Borazjani et al., 2008; Borazjani and Sotiropoulos, 2008,

2010). In SIB methods a complex boundary is typically treated as a sharp interface immersed in a non-boundary-conforming background mesh. The immersed body is discretized by a separate surface mesh which is used to identify the relative location or even track the motion, in the case of moving boundaries, of the immersed body within the fixed Cartesian background mesh. The presence of the solid boundary on the ambient flow is accounted for via suitable boundary conditions reconstruction techniques based on interpolation either along grid lines (Fadlun et al., 2000; Iaccarino and Verzicco, 2003) or the local normal to the immersed boundary (Gilmanov and Sotiropoulos, 2005). An important drawback of SIB techniques with a Cartesian background grid is encountered in internal problems involving flows in curved conduits or manifolds where a large number of grid points can be located outside of the region of interest and unnecessarily burden the computation. To circumvent this problem, Ge and Sotiropoulos (2007) introduced the curvilinear immersed boundary (CURVIB) method, which integrates SIB approaches with generalized curvilinear grids. Unlike standard SIB methods, which use Cartesian background grids, the CURVIB method employs a curvilinear mesh that can either exactly or approximately conform to the immersed boundary shape, thus, greatly minimizing wasted grid nodes. This method, even though promising for modeling arbitrarily complex geometries, has yet to be applied to flows in natural waterways.

1.5 Turbulence modeling of flow in natural streams

Three-dimensional numerical simulation of turbulent flows in natural rivers and streams has been the subject of intense research for well over fifteen years. One of the first three-dimensional models of flow in a natural reach was reported by Sinha et al. (1998) who employed a multi-block approach with generalized curvilinear coordinates to simulate the flow in a 2.5 mile reach of the Columbia River downstream of the Wanapum Dam. They carried out steady Reynolds-averaged simulation (RANS) with the standard $k-\varepsilon$ model with wall-functions and reported good agreement between the simulations and the results of a laboratory-scale model study. Neary et al. (1999) developed a RANS model based on the $k-\omega$ turbulence model (Wilcox, 1993) for solving turbulent flows through lateral intakes with rough walls. The model elucidated the complex three-dimensional flow patterns of lateral-intake flows, including zones of flow division, separation and reversal, vortices, and singular points within the bed-shear stress vector field. Comparisons of the predicted mean velocity field with laboratory measurements showed good agreement. Wilson et al. (2003) employed the $k-\varepsilon$ RANS model to simulate the flow through a pseudo-natural meandering reach that was created in a laboratory environment and also reported good agreement between measured and computed mean velocity fields. Rodriguez et al. (2004) reported RANS simulations of the flow in the 60 m reach of the Embarras River using Flow-3D^{TM} software with the $k-\varepsilon$ RNG model for turbulence closure. The numerical model was able to capture the secondary flow patterns developing in this highly sinuous reach. Lai et al. (2003) solved a laboratory scale meandering open channel flow using the $k-\varepsilon$ model and obtained mean streamwise and transverse velocities that agree well with the measured data. Wormleaton and Ewunetu (2006) solved flow in meandering channels in a laboratory flume using the standard $k-\varepsilon$ models. The results captured secondary cells driven by pressure variation due to

centrifugal forces and predicted the presence of recirculation zones on the outer floodplain, which were also observed in experiments. Zeng et al. (2008) solved the flow field and the sediment transport in the laboratory open channel bends using the Spalart-Allmaras turbulence model (Spalart, 2000) and the SST model (Menter et al., 2003) and compared the computed results with the measured data. Both RANS models gave similar results and qualitatively reproduced the measured flowfield. Zeng et al. (2008) concluded that the discrepancies between the model predictions and the measurements occurring in the region near the outer bank are due to the inability of isotropic RANS models to handle turbulence anisotropy.

Steady RANS models, such as those discussed above, are efficient engineering simulation tools and have been shown to capture with reasonable accuracy the mean flow characteristics in natural rivers. Reach scale flow dynamics in a river can be well resolved by the steady RANS models. However, such models are inherently incapable of resolving the dynamics of large-scale coherent structures and their impact on turbulence production and scalar and particulate transport. Unsteady RANS (URANS) models, which solve the RANS equations in a time accurate manner, can in principle capture large-scale, organized vortex shedding and such models have also been applied to simulate turbulence in natural waterways. Ge and Sotiropoulos (2005), for instance, simulated the flow through a reach of the Chatachochee River near Cornelia, Georgia, with an embedded bridge foundation using an overset grid approach with the standard $k-\varepsilon$ model in URANS mode. The model could capture large-scale vortex shedding from the bridge piers and the simulated mean velocity field was in good agreement with laboratory scale measurements (Ge et al., 2005). In spite of encouraging results, however, the model yielded an essentially steady horseshoe vortex system in the vicinity of the bridge foundation, which is in contrast with experimental observations of Devenport and Simpson (1990) and a direct consequence of the inherent excessive diffusivity of

URANS type models.

The above mentioned works focused primarily on solving the flowfield in open channels. There are also several works which solved both flow and sediment transport in conjunction with the RANS model. Demuren and Rodi (1984), for instance, developed a three-dimensional RANS model of sediment transport for open channels using boundary-fitted, curvilinear coordinates to simulate flow, sediment and contaminant transport in a meandering channel. They compared the computed pollutant concentration with the experimental data. Wu et al. (2000) developed a similar model based on the $k-\varepsilon$ closure for solving flow and sediment transport in a 180° bend. Rüther and Olsen (2005) also developed a RANS model for solving flowfield and bed deformation in a 90° bend. Nagata et al. (2005) used a RANS model with nonlinear $k-\varepsilon$ model under a body-fitted, curvilinear coordinates to resolve flow and sediment transport around a spur dike and a bridge pier. They predict the temporal change in bed topography using a stochastic, bed load formulation, which is based on computing the bed load particle velocity by solving an analytical momentum equation for sediment particles.

While the steady RANS models have been applied to solve the reach scale flows in a river or a stream, LES methods have been mostly applied to solve much smaller scale flows and in relatively simple domains. The computational cost of the LES or hybrid URANS/LES models is much higher than that of the RANS models, however they can accurately simulate the dynamics of coherent vortical structures. Thomas and Williams (1995) carried out LES of flow in a rectangular channel with a floodplain. The LES reproduced the secondary flow at the internal corner and showed the increase in the bed stress on the floodplain. They attributed the increase of the shear stress to the lateral transfer of momentum from the main channel by the extended secondary circulation existing on the floodplain. Hodges and Street (1999) developed a numerical model that solves turbulent free-surface flows. They carried out LES for turbulent open channel flow

with a nonlinear, non-breaking, progressive, surface wave. They employed curvilinear body-fitted grids with the arbitrary Lagrangian-Eulerian (ALE) method to handle the free-surface. Zedler and Street (2001) carried out LES for flow over periodic ripples with body-fitted curvilinear grids to study flow dynamics of the sediment transport. The results yielded detailed bottom shear stress distribution, properly identified coherent structures, and resolved sharp gradients in the sediment concentration. They reported the sediment is carried up into the flow from locations where the shear stress is high – on the upslopes of ripple crests – and is advected downstream by the current and upward by the vertical velocity component. Yue et al. (2005b) studied turbulent open-channel flow over a two-dimensional laboratory-scale dune using LES in conjunction with a free-surface model. The model captured highly complex coherent structures produced behind the dune crest by a strong shear layer riding over the recirculation zone, and the numerical predictions were in good agreement with experimental data. Keylock et al. (2005) applied LES to solve flow over river gravels, and the simulation was able to capture the complexity of the near-bed flow including regions of upwelling. McCoy et al. (2008) studied flow dynamics in a straight open channel containing a multiple-embayment groyne field on one of its sides using the LES. They obtained good agreement of computed mean flow and the root mean square velocity statistics with the measurements. Kirkil et al. (2008) carried out LES of flow around circular cylinder mounted on the mobile bed. Fixed equilibrium bathymetry was employed in the numerical simulation. They investigated coherent structures present in the flow field around a circular cylinder located in a scour hole and found that the structure of the horseshoe vortex inside the scour hole varies considerably in space and time. Stoesser et al. (2010) carried out both steady RANS simulation and LES to solve turbulent flow in a curved open channel and compared the computed mean velocity profile with laboratory measurements. The computed results correctly reproduced the patterns of primary and

secondary flows in the bend. They reported the isotropic RANS model does not capture formation of the outer bank cell, while the LES captures it. Paik and Sotiropoulos (2005) and Paik et al. (2007) have successfully applied detached eddy simulation (DES) (Spalart et al., 1997), a hybrid URANS/LES model, in conjunction with the overset grid method, to simulate the rich dynamics of coherent vortical structures past abutment and bridge-pier like structures mounted in straight rectangular open channels and reported good agreement between the simulations and experiments. The DES of Paik et al. (2007) correctly captured the bimodal probability density functions of the velocity fluctuations in the THSV which was reported by Devenport and Simpson (1990). The results of this computation strengthens the findings of the experiment by Devenport and Simpson (1990) who revealed the flow around the obstacle is dominated by the very complex THSV system created by the roll up of the incoming flow due to the induced adverse pressure gradient.

LES and hybrid URANS/LES models have been successful in resolving dynamically rich coherent vortices in open channels with complex hydraulic structures. However, such models typically require much finer computational grids than RANS and URANS models and thus drastically increase the computational cost. It is presumably due to this limitation that most previous attempts to simulate open channel flows with coherent-structure resolving turbulence models have been restricted to channels of simple topography or focused on the flow in the immediate vicinity of instream structures.

1.6 Needs for further research

Being able to accurately simulate unsteady coherent structures in natural aquatic environments is critical prerequisite not only for understanding scalar and particulate transport processes but also for facilitating a number of important engineering objectives. Examples include, among others, improved design of bridge foundations that are not susceptible to scour, stabilization of streambanks using flow controlling structures, quantification of nutrient residence times to evaluate denitrification potential, and the enhancement of aquatic habitat quality in stream restoration projects. However, as pointed out in Section 1.3, there are major challenges that need to be overcome by the numerical model, which include: 1) high degree of geometric complexity due to presence of man-made structures and irregular topography; 2) the dominant role of dynamically rich coherent structures that require fine computational meshes and suitable turbulence models; 3) the excessive computational costs needed for resolving flow phenomena across the wide range of relevant scales; 4) the large aspect ratio of the computational domain that deteriorates numerical convergence; 5) the presence of the deforming free-surface boundary; and 6) the erodible streambed and the strong coupling between hydrodynamics and morphodynamics. To the best of the author's knowledge, a CFD model that can capture all these complexities has yet to be developed and reported in the literature. In fact, and as the previous literature review has established, high-resolution simulations of turbulence in natural meandering streams with or without instream structures have yet to be reported in the literature.

1.7 Research objectives

The objective of this dissertation is to contribute toward the development of a numerical model that can handle several of the aforementioned modeling challenges at resolution sufficiently high to enable science-based stream-restoration practice. More specifically, the goals of this work are: 1) to develop an accurate and efficient numerical method for carrying out both URANS and LES of flows in natural streams with instream structures at resolution sufficiently fine to resolve the dynamics of reach-scale coherent structures as well as vortex shedding from cm-long roughness elements on the bed; 2) validate this model by comparisons with experimental data for simple laboratory flows but also field-scale experimental measurements in a natural meandering stream; 3) analyze the computed solutions to elucidate physical flow phenomena and their governing mechanisms in meander bends with natural riffle-pool sequences; and 4) demonstrate the potential of the numerical model as a powerful tool for stream restoration design by carrying out high-resolution simulations in a natural stream with a geometrically complex instream structure. The main emphasis of this work is on high-resolution hydrodynamic simulations and as such sediment transport modeling is not part of this study. Consequently, all simulated cases involve a stream of arbitrarily complex albeit fixed bathymetry. Also even though most cases reported herein employ the rigid-lid assumption for modeling the water surface, this work also develops and validates a numerical framework for performing coupled simulations in domains with deforming free-surface. Preliminary results with this coupled model will also be reported for flow in a natural meandering stream.

The remainder of this dissertation is organized as follows.

- Chapter 2 describes the numerical methods for solving Navier-Stokes equations in arbitrarily complex domains and also presents methods for modeling turbulence.

- Chapter 3 reports numerical simulations for validating the developed numerical model.
- Chapter 4 discusses the application of the model for simulating turbulence in a field scale meandering stream with and without instream structures.
- Chapter 5 discusses the flow phenomena and mechanism occurring in a natural meandering stream and presents new findings emerging from the numerical simulations.
- Chapter 6 presents a final discussion and a conclusion.
- Appendix A presents the transformation and discretization of Navier-Stokes equations in the generalized curvilinear coordinate system.
- Appendix B describes the test filtering of large-eddy simulation.
- Appendix C describes the numerical methods for solving free-surface flows in conjunction with the level-set method and reports test cases for the validation of the free-surface model.
- Appendix D describes the third-order WENO discretization method.
- Appendix E describes the GMRES method.

Chapter 2

Governing equations and numerical model

In this chapter we present the equations governing three-dimensional, incompressible turbulent flows dominated by unsteady coherent structures. We also present the models we use for turbulence closure and discuss boundary conditions.

2.1 Governing equations and boundary conditions

2.1.1 Filtered/Reynolds-averaged Navier-Stokes equations

The equations governing the instantaneous, resolved flowfield for three-dimensional, incompressible, turbulent flow are the time (Reynolds) or spatially-averaged (for URANS and LES, respectively) continuity and Navier-Stokes equations. In the curvilinear immersed boundary (CURVIB) method of Ge and Sotiropoulos (2007) employed in this work, the governing equations are first written in Cartesian coordinates $\{x_i\}$ and then transformed fully (both the velocity vector and spatial coordinates are expressed in curvilinear coordinates) in non-orthogonal, generalized, curvilinear coordinates $\{\xi_i\}$.

The filtered/averaged Navier-Stokes equations for incompressible flow read in Cartesian coordinates and in tensor notation (where repeated indices imply summation) as follows ($i, j = 1, 2, 3$):

$$\frac{\partial u_j}{\partial x_j} = 0, \tag{2.1}$$

$$\frac{\partial u_i}{\partial t} + u_j \frac{\partial u_i}{\partial x_j} = -\frac{1}{\rho}\frac{\partial p}{\partial x_i} + \frac{1}{\rho}\frac{\partial}{\partial x_j}\left(\mu \frac{\partial u_i}{\partial x_j}\right) - \frac{1}{\rho}\frac{\partial \tau_{ij}}{\partial x_j} + \frac{1}{\rho}G_i + \frac{1}{\rho}H_i, \tag{2.2}$$

where u_i is the velocity vector, p is the pressure, ρ is the density, μ is the dynamic viscosity, τ_{ij} is the subgrid stress tensor of LES models or Reynolds stress tensor for RANS models, and G_i and H_i are the external forces due to the gravity and the surface tension, respectively.

The fully transformed equations in generalized curvilinear coordinates read in compact tensor notation as follows ($i, j = 1, 2, 3$):

$$J\frac{\partial U_j}{\partial \xi_j} = 0, \tag{2.3}$$

$$\frac{1}{J}\frac{\partial U_i}{\partial t} = \frac{\xi_l^i}{J}\left(-\frac{\partial}{\partial \xi_j}(U_j u_l) + \frac{1}{\rho}\frac{\partial}{\partial \xi_j}(\mu \frac{g^{jk}}{J}\frac{\partial u_l}{\partial \xi_k}) - \frac{1}{\rho}\frac{\partial}{\partial \xi_j}(\frac{\xi_l^j p}{J}) - \frac{1}{\rho}\frac{\partial \tau_{lj}}{\partial \xi_j} + \frac{1}{\rho}G_l + \frac{1}{\rho}H_l\right), \tag{2.4}$$

where J is the Jacobian of the geometric transformation $J = \partial(\xi_1, \xi_2, \xi_3)/\partial(x_1, x_2, x_3)$, $\xi_l^i = \partial \xi_i / \partial x_l$ are the transformation metrics, u_i is the i^{th} Cartesian velocity component, $U_i = (\xi_m^i / J) u_m$ is the contravariant volume flux, and $g^{jk} = \xi_l^j \xi_l^k$ are the components of the contravariant metric tensor. The details of the curvilinear coordinate transformation are presented in Appendix A.

2.1.2 Turbulence closure models

2.1.2.1 URANS models

In URANS models the τ_{ij} tensor in Eq. (2.4) is the Reynolds stress tensor, which is modeled using the Boussinesq hypothesis as follows:

$$\tau_{ij} = -2\mu_t \widetilde{S_{ij}} + \frac{2}{3}\rho k \delta_{ij}, \tag{2.5}$$

where $\widetilde{S_{ij}}$ is the Reynolds averaged strain-rate tensor, μ_t is the dynamic eddy viscosity, k is the turbulence kinetic energy, and δ_{ij} is the unit tensor. To close the URANS equations, the k-ω model (Wilcox, 1988) and the SST model (Menter et al., 2003) are employed in this work.

The governing equations for the k-ω model (Wilcox, 1988) are formulated in generalized curvilinear coordinates as follows:

$$\frac{1}{J}\frac{\partial(\rho k)}{\partial t} + \frac{\partial}{\partial \xi_j}(\rho k U_j) = \tau_{ij}\frac{\xi_j^k}{J}\frac{\partial u_i}{\partial \xi_k} - \frac{1}{J}\beta^* \rho k \omega + \frac{\partial}{\partial \xi_j}\left((\mu + \sigma^* \mu_t)\frac{g^{jk}}{J}\frac{\partial k}{\partial \xi_k}\right), \tag{2.6}$$

$$\frac{1}{J}\frac{\partial(\rho \omega)}{\partial t} + \frac{\partial}{\partial \xi_j}(\rho \omega U_j) = \alpha\frac{\rho\omega}{k}\tau_{ij}\frac{\xi_j^k}{J}\frac{\partial u_i}{\partial \xi_k} - \frac{1}{J}\beta \rho \omega^2 + \frac{\partial}{\partial \xi_j}\left((\mu + \sigma^* \mu_t)\frac{g^{jk}}{J}\frac{\partial \omega}{\partial \xi_k}\right). \tag{2.7}$$

$$\mu_t = \rho k/\omega, \tag{2.8}$$

where the closure coefficients are given as $\alpha = 5/9$, $\beta = 3/40$, $\beta^* = 9/100$, $\sigma = 1/2$, and $\sigma^* = 1/2$.

The governing equations for the SST model (Menter et al., 2003) in generalized curvilinear coordinates read as follows:

$$\frac{1}{J}\frac{\partial(\rho k)}{\partial t}+\frac{\partial}{\partial \xi_j}(\rho k U_j)=\frac{1}{J}\tilde{P}-\frac{1}{J}\beta^*\rho k\omega+\frac{\partial}{\partial \xi_j}\left((\mu+\sigma_k\mu_t)\frac{g^{jk}}{J}\frac{\partial k}{\partial \xi_k}\right), \tag{2.9}$$

$$\begin{aligned}\frac{1}{J}\frac{\partial(\rho\omega)}{\partial t}+\frac{\partial}{\partial \xi_j}(\rho\omega U_j)=&\frac{1}{J}\alpha\rho\widetilde{S}^2-\frac{1}{J}\beta\rho\omega^2+\frac{\partial}{\partial \xi_j}\left((\mu+\sigma_\omega\mu_t)\frac{g^{jk}}{J}\frac{\partial \omega}{\partial \xi_k}\right)\\&+\frac{1}{J}2(1-F_1)\rho\sigma_{\omega 2}\frac{1}{\omega}\left(\frac{\partial \xi_l}{\partial x_j}\frac{\partial k}{\partial \xi_l}\right)\left(\frac{\partial \xi_l}{\partial x_j}\frac{\partial \omega}{\partial \xi_l}\right),\end{aligned} \tag{2.10}$$

$$\mu_t=\frac{a_1\rho k}{max(a_1\omega, SF_2)}, \tag{2.11}$$

where $\widetilde{S}=\sqrt{2\widetilde{S_{ij}}\widetilde{S_{ij}}}$ is the invariant measure of the strain rate and $\tilde{P}$ is a limited production term given by the following equation:

$$\tilde{P}=min\left(\mu_t\frac{\partial u_i}{\partial x_j}\left(\frac{\partial u_i}{\partial x_j}+\frac{\partial u_j}{\partial x_i}\right), 10\beta^*\rho k\omega\right). \tag{2.12}$$

F_1 and F_2 are blending functions defined by

$$F_1=tanh\left\{\left\{min\left[max\left(\frac{\sqrt{k}}{\beta^*\omega d}, \frac{500\mu}{\rho d^2\omega}\right), \frac{4\rho\sigma_{\omega 2}k}{CD_{k\omega}d^2}\right]\right\}^4\right\}, \tag{2.13}$$

$$F_2=tanh\left[\left[max\left(\frac{2\sqrt{k}}{\beta^*\omega d}, \frac{500\mu}{\rho d^2\omega}\right)\right]^2\right], \tag{2.14}$$

with

$$CD_{k\omega}=max\left(2\rho\sigma_{\omega 2}\frac{1}{\omega}\frac{\partial k}{\partial x_j}\frac{\partial \omega}{\partial x_j}, 10^{-10}\right). \tag{2.15}$$

and d is the distance to the nearest wall.

The closure coefficients of the SST model are obtained by blending those of the k-ω model, denoted as ϕ_1, and the standard k-ϵ model, denoted as ϕ_2, via the relation

$\phi = \phi_1 F_1 + \phi_2(1 - F_1)$. The coefficients are given by $a_1 = 0.31$, $\beta^* = 9/100$, $\alpha_1 = 5/9$, $\beta_1 = 3/40$, $\sigma_{k1} = 0.85$, $\sigma_{\omega 1} = 0.5$ $\alpha_2 = 0.44$, $\beta_2 = 0.0828$, $\sigma_{k2} = 1$, $\sigma_{\omega 2} = 0.856$.

2.1.2.2 Large-eddy simulation

The filtered Navier-Stokes equations solved in LES (Eqs. (2.3),(2.4)) are obtained by decomposing the velocity into resolved and unresolved components and integrating the Navier-Stokes equations over a spatial filter (Sagaut, 1988). As a result, sub-grid stress terms appear in the momentum equations (Eq.(2.4)), which are modeled using the Smagorinsky sub-grid scale (SGS) model (Smagorinsky, 1963)

$$\tau_{ij} - \frac{1}{3}\tau_{kk}\delta_{ij} = -2\mu_t \overline{S_{ij}}, \tag{2.16}$$

where the overbar denotes the grid filtering operation, and $\overline{S_{ij}}$ is the filtered strain-rate tensor. The eddy viscosity is calculated as follows:

$$\mu_t = C_s \Delta^2 |\overline{S}|, \tag{2.17}$$

where C_s is the Smagorinsky constant, Δ is the filter size, and $|\overline{S}| = \sqrt{2\overline{S_{ij}}\,\overline{S_{ij}}}$. The box filter (Sagaut, 1988) is employed in the present model, for which its size given as follows:

$$\Delta = J^{-1/3}. \tag{2.18}$$

The dynamic Smagorinsky model (Germano et al., 1991) is employed as a sub-grid model in which the model constant C_s evolves in space and time as function of the flow. The optimal value of C_s is selected to minimize the mean square error between the resolved stress at the grid filter and the test filter (Germano et al., 1991) as follows:

$$C_s = \frac{\langle L_{ij} M_{ij} \rangle}{\langle M_{kl} M_{kl} \rangle}, \tag{2.19}$$

where

$$L_{ij} = \widehat{\overline{u_i}\,\overline{u_j}} - \widehat{\overline{u_i}}\,\widehat{\overline{u_j}}, \tag{2.20}$$

$$M_{ij} = 2\Delta^2 \widehat{\overline{S_{ij}}|\overline{S}|} - 2\widehat{\Delta}^2 \overline{S_{ij}}|\widehat{\overline{S}}|. \tag{2.21}$$

In the above equations, $\widehat{\Delta}$ is the size of the test filter which is twice as large as the grid filter for uniform grids and the hat denotes the test filtering operation, which in three-dimensions involves the 27 grid nodes surrounding a given grid node. $\langle\,\rangle$ denotes averaging in the homogeneous directions. For problems with no homogeneous direction present (e.g. fully three-dimensional flows) this averaging can be replaced by local averaging around a grid node (see Appendix B for details).

It was pointed out by Armenio and Piomelli (2000) that Eq. (2.19) is not invariant with respect to a rotation of the frame of the reference in generalized curvilinear coordinates. To remedy this, the following invariant formulation is employed in this work:

$$C_s = \frac{\langle L_{il} M_{im} G_{lm} \rangle}{\langle M_{kp} M_{kq} G_{pq} \rangle}, \tag{2.22}$$

where G_{ij} is the covariant metric tensor defined as $G_{ij} = (\partial x_l/\partial \xi_i)(\partial x_l/\partial \xi_j)$.

In the present numerical implementation of the above SGS model, the Smagorinsky constant and the eddy viscosity are computed at the center of the cell using Eq. (2.22) and Eq. (2.17), respectively, at the beginning of each time step. Subsequently the eddy viscosity is interpolated from the cell center to the cell face and it is used to calculate the SGS terms in Eq. (2.16).

2.1.3 Velocity boundary conditions

2.1.4 Wall boundary conditions

In low Reynolds number flow simulations and assuming that the computational mesh is sufficiently fine to resolve the velocity gradients near the wall, the no-slip boundary condition is specified near the wall as follows ($i = 1, 2, 3$):

$$u_i = 0. \tag{2.23}$$

In high Reynolds number flow simulations, however, applying the no-slip boundary condition at the wall is often impractical as it results in excessively fine meshes and long computational times. To address this difficulty the wall model proposed by Cabot and Moin (2000) and Wang and Moin (2002) is employed in this work. These models handle the near wall region with the RANS approach assuming that the flow near the wall is governed by the boundary layer equations. The boundary layer equations are typically simplified by dropping the non-linear terms and the resulting equations are used to derive a boundary condition for the velocity vector at the first grid node off the wall. In this work, this wall modeling approach is employed both for LES and URANS models. The model solves the Reynolds-averaged boundary layer equation in the following form:

$$\frac{1}{\rho}\frac{\partial}{\partial l}\left((\mu+\mu_t)\frac{\partial u_{si}}{\partial l}\right) = \frac{1}{\rho}\frac{\partial p}{\partial s} + \frac{\partial u_{si}}{\partial t} + \frac{(\partial u_l u_{si})}{\partial s}, \tag{2.24}$$

where l and s indicate the directions normal and tangential to the wall, respectively, and i denotes the directions of two velocity components which are tangent to the wall. By neglecting the right hand side of the Eq. (2.24), one obtains the equilibrium stress balance model (Wang and Moin, 2002)

$$\frac{1}{\rho}\frac{\partial}{\partial l}\left((\mu+\mu_t)\frac{\partial u_{si}}{\partial l}\right) = 0. \tag{2.25}$$

The eddy viscosity is modeled by the mixing length model with the near-wall damping as follows:

$$\mu_t = \mu\kappa l^+(1 - e^{-l^+/19})^2, \tag{2.26}$$

where $l^+ = \rho u_\tau l/\mu$, and u_τ is the wall shear velocity. The above equation is integrated from the wall to the second off-wall node to obtain the velocity at the first off-wall node. The implementation of this model, which can be used in conjunction with either a URANS model or LES, in the context of the CURVIB method is discussed in Section 2.3.2.

2.1.5 Free-surface boundary conditions

Most simulations reported in this dissertation employ the rigid-lid approximation (Mcguirk and Rodi, 1978) for handling the free-surface boundary, whose shape is prescribed as input to the numerical model from experimental measurements. This conditions is valid for low Froude numbers and treats the surface as a shear-free (or a free-slip) rigid interface by applying the following condition at the surface:

$$\frac{\partial u_i}{\partial s_j} = 0 \quad (i, j = 1, 2), \tag{2.27}$$

$$u_i l_i = 0 \quad (i = 1, 2, 3), \tag{2.28}$$

where s_j and l_i denote a direction tangent and normal to the free-surface, respectively.

When the measured water surface elevations are not available, the free-surface elevation needs to be predicted numerically as part of the solution of the flow equations.. A fully nonlinear, three-dimensional free-surface model based upon the level-set approach is developed in the present work for modeling free-surface flows in open channels with

arbitrarily complex geometric configurations. The reader is referred to Appendix C for details of the model.

2.1.6 k and ω boundary conditions

The low Reynolds number wall boundary conditions for k and ω are given as follows (Wilcox, 1993):

$$k = 0, \tag{2.29}$$

$$\omega = \frac{6\mu}{\rho\beta d^2}, \tag{2.30}$$

where d is the distance of the first off-wall grid from the nearest wall. The above boundary conditions are valid when the first off wall grid point is located inside the viscous sublayer.

The high Reynolds number wall boundary conditions for k and ω are, which need to be applied when the near-wall grid is not fine enough to resolve the laminar sublayer, read as follows (Wilcox, 1993):

$$k = \frac{u_\tau^2}{\sqrt{\beta^*}}, \tag{2.31}$$

$$\omega = \frac{u_\tau}{\sqrt{\beta^*}\kappa d}, \tag{2.32}$$

where $\kappa = 0.4$ is the von Kármán constant, and u_τ is the wall shear velocity calculated by solving Eqs. (2.47) and (2.48). The above boundary conditions are adopted when the first off wall grid point is located inside the logarithmic layer.

2.2 Numerical solution of Navier-Stokes and URANS equations

2.2.1 The fractional step method

To solve the resolved flow equations, Eq. (2.3) and Eq. (2.4), we employ the implicit fractional step method proposed by Ge and Sotiropoulos (2007). During the first step, the momentum equations Eq. (2.4) are discretized in a fully implicit manner using second-order backward differencing in time:

$$\frac{1}{J}\frac{3\mathbf{U}^* - 4\mathbf{U}^n + \mathbf{U}^{n-1}}{2\Delta t} = RHS(\mathbf{U}^*, \mathbf{u}^*), \tag{2.33}$$

where n denotes the time level, and RHS is the right hand side of Eq. (2.4). Both advection and diffusion terms in the right hand side of Eq. (2.33) are discretized using, three-point central, second-order accurate finite-differencing. Both of two variables, $\mathbf{U}^*$ and $\mathbf{u}^*$, appear in the right hand side of the above equation, because the Navier-Stokes equations are discretized using the hybrid staggered/non-staggered grid approach (Gilmanov and Sotiropoulos, 2005) which use both the contravariant volume flux and the Cartesian velocity vectors for the discretization (see Appendix A for details).

The intermediate volume flux U^* obtained by solving Eq. (2.33) is not divergence-free and needs to be corrected to satisfy the continuity equation. This is accomplished by formulating and solving the following Poisson equation for the pressure increment (or pressure correction) $\Pi = p^{n+1} - p^n$:

$$-J\frac{\partial}{\partial \xi_i}\left(\frac{1}{\rho}\frac{\xi_l^i}{J}\frac{\partial}{\partial \xi_j}(\frac{\xi_l^j \Pi}{J})\right) = \frac{3}{2\Delta t} J \frac{\partial U_j^*}{\partial \xi_j}. \tag{2.34}$$

Following the solution of the above equation (see below), the pressure and contravariant volume fluxes are obtained as follows:

$$p^{n+1} = p^n + \Pi, \tag{2.35}$$

$$U_i^{n+1} = U_i^* - J\frac{2\Delta t}{3}\frac{1}{\rho}\frac{\xi_l^i}{J}\frac{\partial}{\partial \xi_j}(\frac{\xi_l^j \Pi}{J}). \tag{2.36}$$

The above fractional step algorithm is implemented discretely in a hybrid staggered/non-staggered grid, which was originally proposed by Gilmanov and Sotiropoulos (2005) for Cartesian grids and subsequently extended to curvilinear coordinates by Ge and Sotiropoulos (2007). The formulation is such that it satisfies the discrete divergence of the velocity field to machine zero in generalized curvilinear grids. For details of the discretization the reader is referred to Appendix A.

2.2.1.1 Solution of the discrete momentum equation

The discretized momentum equation given by Eq. (2.33) is a nonlinear ordinary differential equation for $\mathbf{U}^*$ that can be written as follows:

$$F(\mathbf{U}) = 0, \tag{2.37}$$

where F is a general functional involving both the time derivative and the right hand side of the discrete momentum Eq. (2.33) and the superscript * from Eq. (2.33) is omitted for brevity. To linearize the functional $F(\mathbf{U})$ we expand it in a Taylor series about $\mathbf{U} = \mathbf{U}^k$ (where $\mathbf{U}^k$ is the approximation to the final solution $\mathbf{U}^*$ during the k^{th} iteration):

$$F(\mathbf{U}^k + \delta\mathbf{U}^k) = F(\mathbf{U}^k) + F'(\mathbf{U}^k)\delta\mathbf{U}^k + O(\delta\mathbf{U}^2), \tag{2.38}$$

where $\delta\mathbf{U}$ denotes the increment of $\mathbf{U}$ at each iteration and $F'(\mathbf{U})$ is defined as $F'(\mathbf{U}) = \partial F(\mathbf{U})/\partial\mathbf{U}$.

Neglecting the higher-order terms and setting the right hand side to zero yields the Newton's method

$$A(\mathbf{U}^k)\delta\mathbf{U}^k = -F(\mathbf{U}^k), \tag{2.39}$$

$$\mathbf{U}^{k+1} = \mathbf{U}^k + \alpha_k \delta\mathbf{U}^k, \tag{2.40}$$

where A is the Jacobian matrix of F given by $A(\mathbf{U}^k) = F'(\mathbf{U}^k)$, and α_k is the parameter that controls the convergence. During each iteration k (denoted as outer iteration) the now linear system given by Eq. (2.39) is solved by using the GMRES method (Saad and Schultz, 1986) (see Appendix E). The procedure that solves the linear system is called the inner iteration. When the GMRES method is used as a linear solver for the inner iteration, the Jacobian matrix does not need to be stored since it only requires matrix-vector products which can be approximated by a simple finite difference method, as follows (Brown and Saad, 1990):

$$A\mathbf{x} = \frac{F(\mathbf{U} + \sigma\mathbf{x}) - F(\mathbf{U})}{\sigma}, \tag{2.41}$$

where σ is a small scalar perturbation computed by (Brown and Saad, 1990)

$$\sigma = e_r U_{min} sign(\mathbf{U}^T\mathbf{x})||\mathbf{x}||_1/||\mathbf{x}||_2^2, \tag{2.42}$$

where $e_r = 10^{-8}$ is the the square root of the relative error in the function evaluations, $U_{min} = 10^{-6}$ is a tunable parameter, and $||\mathbf{x}||_p$ denotes the L_p norm of the vector $\mathbf{x}$ defined as $||\mathbf{x}||_p = (|x_1|^p + |x_2|^p + ... + |x_n|^p)^{\frac{1}{p}}$, and n is the length of the vector $\mathbf{x}$. Since Jacobian-free methods do not require assembling and storing the Jacobian matrix, it is appropriate for problems with large number of unknowns.

At each time step, the outer and inner iterations are repeated until the residuals satisfy the following convergence criterion:

$$\|\mathbf{r}^k\|_2 = \|A(\mathbf{U}^k)\delta\mathbf{U}^k + F(\mathbf{U}^k)\|_2 \leq \eta_k \|F(\mathbf{U}^k)\|_2, \tag{2.43}$$

where $\eta_k \in (0, 1)$ is a forcing term that controls the convergence of the solution. Instead of using a constant value of the forcing term, we employed the techniques proposed by Eisenstat and Walker (1996), which was shown to improve the convergence of the iterative scheme, for computing η_k at each iteration:

$$\eta_k = \frac{\left| ||F(\mathbf{U}^k)||_2 - ||F(\mathbf{U}^{k-1}) + F'(\mathbf{U}^{k-1})\delta\mathbf{U}^{k-1}||_2 \right|}{||F(\mathbf{U}^{k-1})||_2}. \tag{2.44}$$

It is important to emphasize, however, that the above Newton's method converges only when the initial guess is sufficiently close to the exact solution. To make Newton's method globally convergent, one often needs a globalization method that brings the initial iterate into the radius of convergence of Newton's method (Knoll and Keyes, 2004). The line search method (Dennis and Schnabel, 1983) is employed in this work for the globalization of the Newton-Krylov method. The line search is the method that finds values for α_k in Eq. (2.40) which satisfy $F(\mathbf{U}^k + \alpha_k\delta\mathbf{U}^k) < F(\mathbf{U}^k)$. The iterations of solving nonlinear equations may fail by simply setting $\alpha_k = 1$ (Dennis and Schnabel, 1983).

The procedure described above solves the momentum equation in a fully implicit manner which greatly improves the stability of the numerical scheme and removes the CFL (Courant-Friedrichs-Lewy) time step restriction.

2.2.1.2 The algebraic multigrid method for the Poisson equation

As already discussed in the introduction, a major challenge for carrying out reach-scale, high-resolution simulations of turbulence in natural waterways stems from the large

aspect-ratio of the resulting computational domains due to the large disparity in flow depth the streamwise and lateral dimensions of the reach. Large domain and grid cell aspect-ratios induce numerical stiffness and could dramatically deteriorate the convergence rate of powerful iterative algorithms such as the previously described GMRES method (Saad and Schultz, 1986). This is an especially critical issue for the solution of the Poisson equation that needs to be satisfied to machine zero during every time step in order to satisfy the incompressibility condition for the velocity field. To improve the convergence of the Poisson equation in large aspect-ratio grids and domains, we employ the algebraic multigrid (AMG) as the preconditioner for the GMRES method (Saad and Schultz, 1986). The multigrid (MG) method has been one of the most successful methods for accelerating the convergence of elliptic equation solvers, and particularly geometric multigrid (GMG) methods have been popular for the simulation of incompressible flows with structured grids (Rosenfeld et al., 1991; Ge and Sotiropoulos, 2007). In the GMG, the convergence is accelerated by correcting the solution of the fine grid by solving an error residual equation on the coarser grid. Often more than two grid levels are employed, and the coarse grid usually is twice as coarse as the grid spacing of the next finer level grid. More details about the implementation of GMG can be found in Briggs et al. (2000). The drawback of the GMG is that the convergence rate degenerates as the grid becomes more stretched and cell aspect ratios increase. The method with semi-coarsening has shown promise in simulations involving stretched, large aspect-ratio grids (Naik and Rosendale, 1993; Larsson et al., 2005; Ge and Sotiropoulos, 2007) but convergence could still be sluggish in generalized curvilinear grids and large aspect-ration domains. In fact initial attempts to employ GMG in this work were not successful as it was found that the computational resources required to converge the Poisson equation were so large that high-resolution simulations of turbulence in real-life streams were impractical.

The AMG does not utilize the geometric information to build coarse grids, instead the adjacency graph of the matrix to be inverted is used. For example, we say that the point i strongly depends on j and vice versa if (Ruge and Stüben, 1987)

$$-a_{ij} \geq \gamma \max_{k \neq i}(-a_{ik}), \tag{2.45}$$

where a_{ij} is the component of a matrix at the ith row and the jth column and $\gamma \in (0, 1)$ is a strength threshold. The above criterion was employed in the Ruge-Stüben coarsening algorithm (Ruge and Stüben, 1987) for building the coarse grid matrix. The underlying idea behind using the threshold γ in Eq. (2.45) is very similar to that of the semi-coarsening method of the GMG, which generates coarse grids by neglecting the geometrically stretched directions, but is more general since it is not dependent on the the geometric shape of the grid. For this reason, the AMG is more appropriate method for solving problems with complicated geometry and is employed in this work. In the present solver we implement AMG by employing the BoomerAMG package (Henson and Yang, 2002) with the parallel modified independent set (PMIS) coarsening scheme (Sterck et al., 2006).

To demonstrate the drastic efficiency improvements that can be obtained with AMG, we employ the fractional step method described above to simulate impulsively started laminar flow through a very long square duct whose cross section is intentionally discretized with highly stretched and distorted grids as shown in Figure 2.1. This unusual grid structure is employed in order to set up a challenging numerical experiment combining a large-aspect ratio domain (streamwise length to width ratio equal to 10^3) with highly stretched and skewed grids. The Reynolds number based on the width of the duct and the mean velocity is 100 and the Poisson equation is solved with four different algorithms: AMG; GMG with 3-level semi-coarsening; GMG with 6-level semi-coarsening; and no multigrid. Four processors are used for the computation.

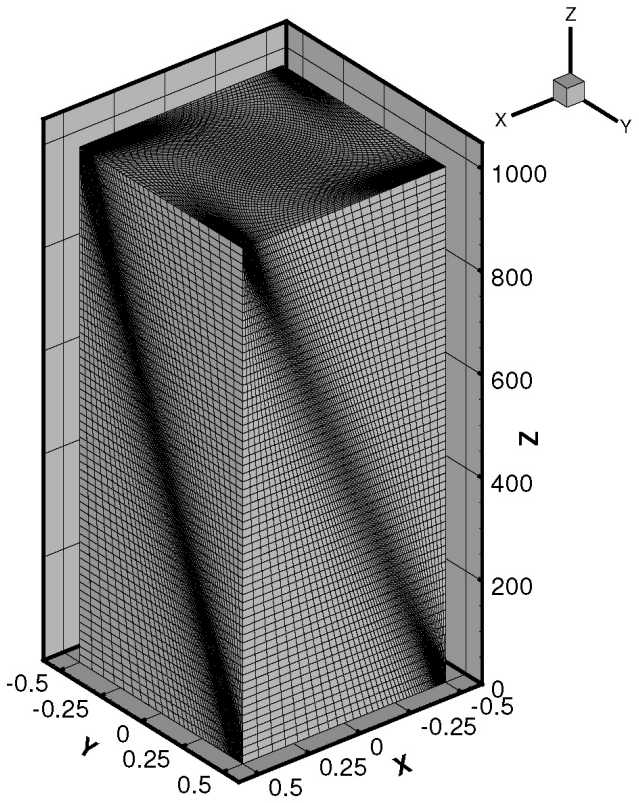

(a) Three-dimensional view.

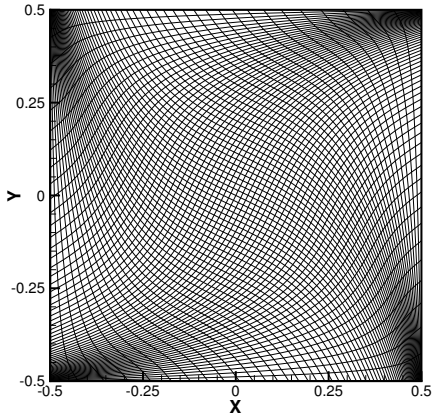

(b) Cross sectional view at z=0.

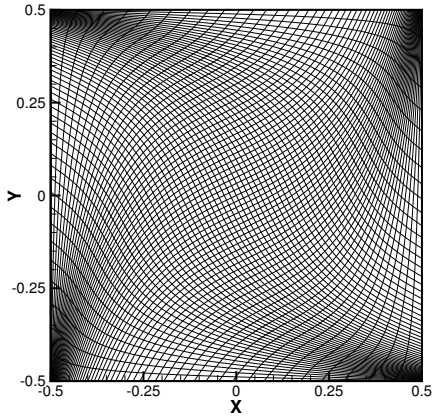

(c) Cross sectional view at z=1000.

Figure 2.1: Grid used for testing the efficiency of the AMG solver.

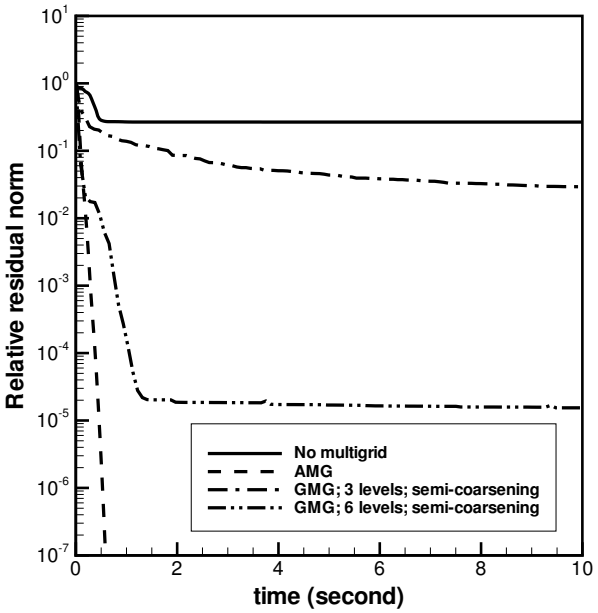

Figure 2.2: Convergence of the Poisson equation.

The convergence history is shown in Figure 2.2. It is evident that the no-multigrid option fails to converge while the GMG algorithm does improve the convergence rate somewhat especially when the number of grid coarsening levels is increased. Even for the 6-level GMG algorithm, however, the Poisson equation does not reach machine zero. Only with AMG the iterative algorithm converges monotonically to machine zero in just a fraction of a second of computational time. These results clearly show that large aspect ratios, grid stretching in multiple directions, and grid non-orthogonality cannot be easily treated by the standard semi-coarsening method of the GMG and establish the superior efficiency of the AMG over the GMG. The efficiency gains documented in Figure 2.2 become even more significant in the context of applying AMG to solve the Poisson equation in a LES when several thousands of time steps need to be realized computationally to obtain statistically converged flowfields.

2.2.2 Solution of $k-\omega$ equations

Third-order WENO (Jiang and Shu, 1996) (see Appendix D) and second-order central differencing schemes are used for the spatial discretization of advection and diffusion terms in k and ω equations, respectively, and the second-order backward differencing scheme is used for the time integration. The k and ω equations of k-ω and SST models are solved at every time step after the velocity fields are obtained by the subsequently described fractional step method. The values of eddy viscosity are calculated at the center of the cell using Eq. (2.11), and they are interpolated to the face of the cell. The fully implicit Jacobian-free Newton's method is employed for solving Eq. (2.6) and Eq. (2.7) in order to enhance numerical stability.

2.3 Treatment of complex geometry

2.3.1 The CURVIB method

The CURVIB method (Ge and Sotiropoulos, 2007) was originally proposed for cardiovascular flow applications in which a moving immersed boundary, e.g. a mechanical heart valve, is embedded in a background domain that can be efficiently discretized with a boundary-fitted curvilinear mesh (e.g. a curved blood vessel). Rather than using a boundary conforming mesh to describe the immersed moving boundary, the CURVIB methods treats the boundary as a sharp interface and boundary conditions are re-constructed at curvilinear grid nodes in the immediate vicinity of the boundary using interpolation along the local normal to the boundary direction (Gilmanov and Sotiropoulos, 2005; Ge and Sotiropoulos, 2007). So far the method has been applied to carry out direct numerical simulations of cardiovascular flows involving fluid structure interaction (Borazjani and Sotiropoulos, 2008) and swimming of fish and planktonic organisms (Borazjani and Sotiropoulos, 2010; Borazjani et al., 2010). The CURVIB framework, however, is ideally suited for simulating flows in natural meandering streams with arbitrarily complex bed topography and instream structures. A schematic illustrating the application of the CURVIB method for a meandering stream is shown in Figure 2.3. The immersed boundaries (bathymetry and instream structures) are discretized with a triangulated surface mesh and embedded in a curvilinear domain that follows the meandering outline of the stream but has a regular (prismatic) cross section that contains fully the actual stream everywhere. In this section we describe the details of the method by emphasizing the new algorithmic developments implemented in this work to extend it to turbulent flow simulations.

In the CURVIB method, the boundaries of solid bodies are treated as sharp interfaces immersed in a background Cartesian or curvilinear grids. As shown in Figure 2.4, the

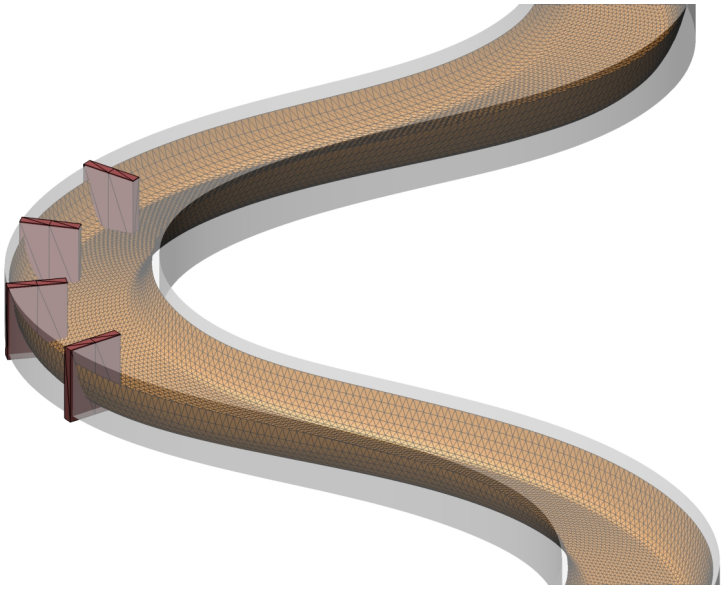

Figure 2.3: Schematic description of applying the CURVIB method for the natural stream.

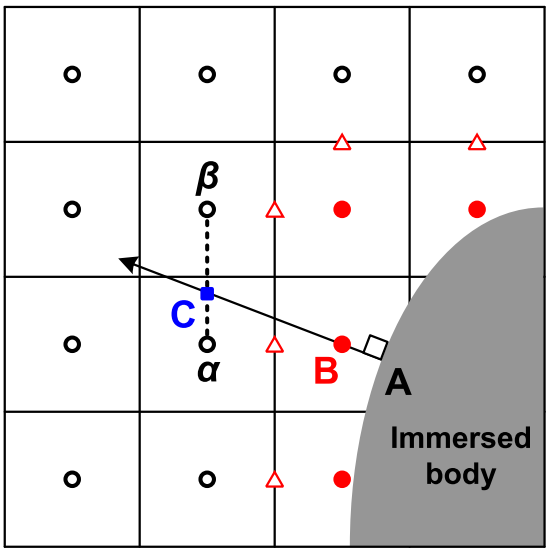

Figure 2.4: Schematic description of the wall normal interpolation at the IB node. (circles filled with red color: IB nodes, circles without fill: internal nodes, square filled with blue color: interception node, triangles: cell faces where the volume flux is stored).

grid nodes are classified relative to their location with respect to the immersed body: solid nodes, IB nodes, fluid nodes. A ray-triangle intersection method (Möller and Trumbore, 1997; Borazjani et al., 2008) has been used to classify the type of the nodes. In this method, starting from the point under consideration, a random half-infinite ray is casted and the number of intersections between the half ray and a closed surface of an immersed body are counted. If the number of intersections is odd then the point is located inside the body, otherwise it is located outside. The solid nodes are blanked out of the computation, and equations are solved only at fluid nodes. The boundary conditions at IB nodes are reconstructed as described below.

The standard CURVIB method (Ge and Sotiropoulos, 2007) employs wall normal interpolation for calculating the velocity components at near-wall grid nodes–referred to as Immersed Boundary or IB grid nodes–under the hybrid staggered/non-staggered grid layout proposed by Gilmanov and Sotiropoulos (2005). Figure 2.4 illustrates the wall normal interpolation for a velocity component or a turbulence quantity. At a given node (B in Figure 2.4) immediately adjacent to the immersed boundary, a straight line is drawn normal to the nearest wall (A in Figure 2.4) until it intersects with the grid line (or plane in three-dimensional space) which connects two (three in three-dimensional space) neighboring internal nodes. The point C in Figure 2.4 is called the interception point. The values of flow variables at the point C are obtained by linear interpolation from computed values at internal grid nodes α and β. Gilmanov and Sotiropoulos (2005) used the above approach to compute the velocity at the IB nodes in a manner such that the no-slip boundary condition is exactly satisfied at the wall. They used linear and quadratic interpolation which for turbulent flows would work well only if the grid spacing in the vicinity of the immersed boundary is sufficiently fine to resolve the laminar sublayer region and directly impose the no-slip condition on the solid immersed boundary. When the mesh is not sufficiently fine (as is often the case for

high Reynolds number turbulent flows), however, the wall model described in Section 2.1.3 above is used to reconstruct the boundary conditions. In what follows we describe the implementation of boundary conditions in the CURVIB method for both velocity components and turbulence quantities.

2.3.2 Velocity boundary conditions

As discussed above, the no-slip boundary condition is employed when the near wall grid spacing is fine enough to resolve the viscous sublayer. Assuming the i^{th} component of the velocity vector at the solid wall (point A) is u_i^A, which is zero when the wall is not moving, and its distribution along the points A, B and C is linear, the Cartesian velocity components at the IB node is given as follows:

$$u_i^B = \left(\frac{\overline{AB}}{\overline{AC}}\right)(u_i^C - u_i^A) + u_i^A, \tag{2.46}$$

where i=1, 2, and 3, and $\overline{AB}$ and $\overline{AC}$ denote the distance between the points A and B and the points A and C, respectively.

When the near wall grid spacing is not fine enough to resolve the viscous sublayer, the velocity boundary condition is obtained by the wall modeling approach. Integration of Eq. (2.25) from the surface of the wall at $l = 0$ to the the second off-wall node at $l = \delta_c$ (C in Figure 2.4) yields the following nonlinear equation

$$\tau_w = \mu \frac{\partial u_{si}}{\partial l}\Big|_{l=0} = \frac{1}{\int_0^{\delta_c} \frac{1}{\mu+\mu_t} dl}\left(u_{si}(\delta_c) - u_s(0)\right), \tag{2.47}$$

with

$$\tau_w = \rho u_\tau^2, \tag{2.48}$$

where δ_c is the distance from the wall to the node C, and τ_w is the wall shear stress

component in the tangential direction to the wall. Eq. (2.26) is used to compute the eddy viscosity (μ_t) in Eq. (2.47).

The tangential direction s_i is determined from the velocity vector at the second off-wall node. The unit vector tangential to the wall is given by

$$s_i = \frac{u_i^C - (u_j^C l_j) l_i}{\left| u_i^C - (u_j^C l_j) l_i \right|}, \tag{2.49}$$

where n_i is the unit vector normal to the wall. The tangential velocity component at the wall is given by

$$u_s(0) = u_j^A s_j, \tag{2.50}$$

which is zero when the wall is stationary.

Eq. (2.47) is non-linear in terms of u_τ (which also appears in the right hand side in the model for mu_t given by Eq. (2.47)) and is solved iteratively for u_τ using Newton's method. Usually 4 or 5 iterations are sufficient to get the converged solution. Once u_τ is computed, the tangential velocity component at the first off wall node (B in Figure 2.4) is obtained as follows:

$$u_s(\delta_b) = \frac{\int_0^{\delta_b} \frac{1}{\mu+\mu_t} dl}{\int_0^{\delta_c} \frac{1}{\mu+\mu_t} dl} \left(u_s(\delta_c) - u_s(0) \right) + u_s(0) \tag{2.51}$$

where δ_b is the distance from the wall to the node B. The normal velocity component at the IB nodes is obtained by the wall normal linear interpolation method. The above procedure is employed both for RANS and LES models. Although in this work the wall modeling method will be applied to solve problems involving only stationary immersed bodies, it is designed to be readily applicable to flow problems involving moving immersed bodies such as those encountered in fluid-structure interaction problems.

2.3.3 The k and ω boundary conditions

To impose the low Reynolds number boundary condition given by Eq. (2.29) at the wall (A in Figure 2.4), the linear interpolation along the line normal to the wall is employed. Assuming $k = 0$ at the node A one obtains the value of k at the IB node (B in Figure 2.4)

$$k^B = \left(\frac{\overline{AB}}{\overline{AC}}\right) k^C. \tag{2.52}$$

The boundary condition for ω, Eq. (2.30), is directly imposed at the IB node. The wall distance at the first off-wall grid (d) is given by $\overline{AB}$ in Figure 2.4.

The high Reynolds number boundary conditions given by by Eq. (2.31) and Eq. (2.32) are also directly imposed at the IB node after wall shear velocity has been obtain from the previously described iterative procedure for obtaining the velocity boundary conditions.

2.3.4 Correction of velocity boundary conditions for global mass conservation

The previously described reconstruction techniques are used to specify velocity boundary conditions for the intermediate velocity field U^* in order to solve the momentum equation Eq. (2.4). The so resulting velocity field U^* does not satisfy the integral global mass conservation condition since this condition is not imposed either in the reconstruction of boundary conditions or in the solution of the momentum equation. As such, the pressure Poisson equation in Eq. (2.34) is ill posed, the so-called compatibility condition for Poisson equations is violated, and any attempt to solve it numerically will not converge. To remedy this situation, we propose a correction of the velocity boundary conditions at the IB nodes based on an area weighted volume flux approach. Figure 2.5 illustrates in a schematic how this correction is implemented. The light gray areas

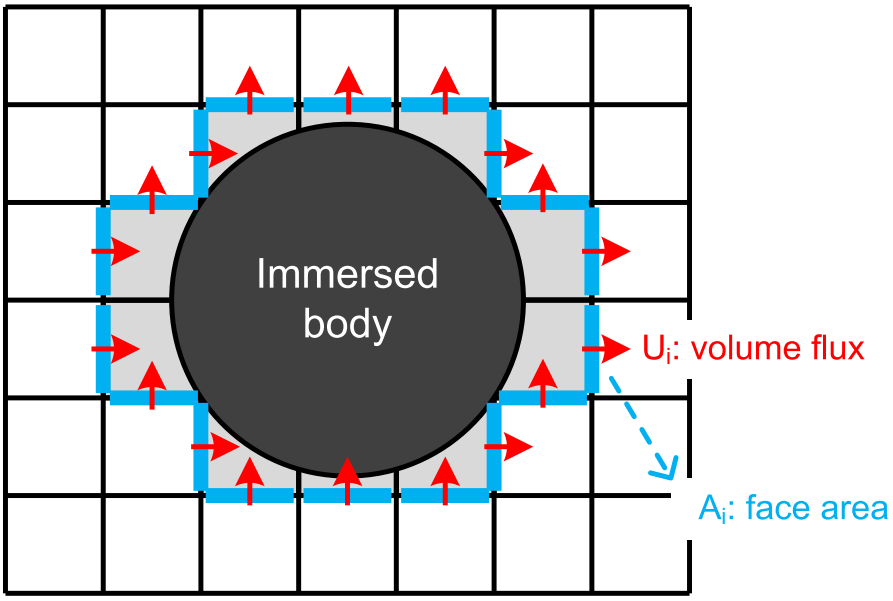

Figure 2.5: Schematic description of the flux correction at the IB nodes.

denote the IB nodes, and the arrows denote the contravariant volume flux adjacent to both an IB node and a fluid node. To satisfy the global mass conservation the sum of all volume fluxes over a closed surface that surrounds a solid boundary, as shown in Figure 2.5, must be zero. To satisfy this condition, the sum of the volume fluxes weighted by the ratio of the local face area (blue areas in Figure 2.5) to the total area is subtracted from the individual volume fluxes. Mathematically, this correction is formulated as follows:

$$\widetilde{U^*}_i = U_i^* - A_i \left(\frac{\sum_k U_k^*}{\sum_k A_k} \right), \tag{2.53}$$

where i denotes the cell face whose volume flux is being corrected, A_i is the area of the cell face adjacent to an IB node and a fluid node (blue areas in Figure 2.5), U is the contravariant volume flux before correction, the index k spans all cell faces (all

blue areas in Figure 2.5) adjacent to both an IB node and a fluid node, and $\widetilde{U^*}$ is the corrected boundary flux used to calculate the right hand side of Eq. (2.34)

Chapter 3

Validation of the numerical model

In this chapter, results aimed at validating the numerical method are presented. To demonstrate the accuracy of the various facets of the method simulations for three model problems solved using direct numerical simulation (DNS), RANS, and LES, respectively, are first presented.

3.1 DNS of fully developed turbulent flow in a channel

DNS of turbulent flow in a plane channel presents an excellent case for testing the spatial and temporal resolution of the method in a simple computational domain that can be handled in a straightforward manner using a body-fitted Cartesian grid.

DNS was carried out for turbulent channel flow at $Re_\tau = 180$. Re_τ is Reynolds number based on the wall shear velocity and the channel half height. The size of the computational domain is 6.4, 3.2, and 2 channel half heights in the streamwise (z), spanwise (x), and vertical (y) directions, respectively, and a grid with $193 \times 129 \times 161$ is used to discretize the computational domain along these directions. The grid increments in the spanwise and streamwise directions are 4.5 and 6 wall units, respectively. One

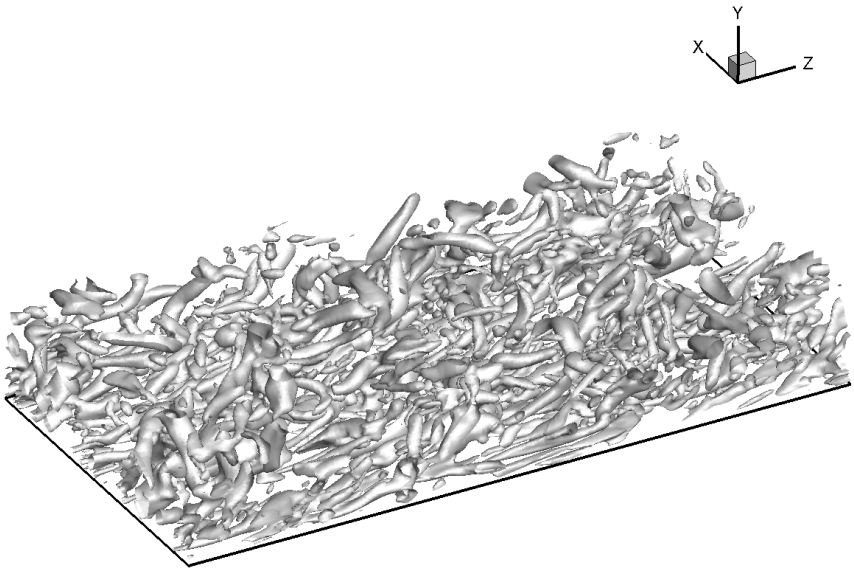

Figure 3.1: Vortical structure ($\lambda_2 = -100$) in fully developed turbulent channel flow at $Re_\tau = 180$.

wall unit equals to the non-dimensional wall distance defined by u_τ/ν, where u_τ is the wall shear velocity and ν is the kinematic viscosity. The minimum and maximum grid spacing in the vertical direction is 0.8 and 4.3 wall units, respectively. Periodic boundary conditions are employed in the streamwise and spanwise directions and the flow is driven by the constant pressure gradient imposed in the streamwise direction. The time step was chosen as $\Delta t = 4 \times 10^{-4}$. A parabolic streamwise velocity profile with superimposed random fluctuations is prescribed as the initial condition. The simulation was first run until the total kinetic energy of the computational domain reached steady-state. Following this, the simulation was continued and the solution was averaged for t = 20, which corresponds to about 48 flow through times.

The computed vortical structures above the bottom wall visualized using the λ_2

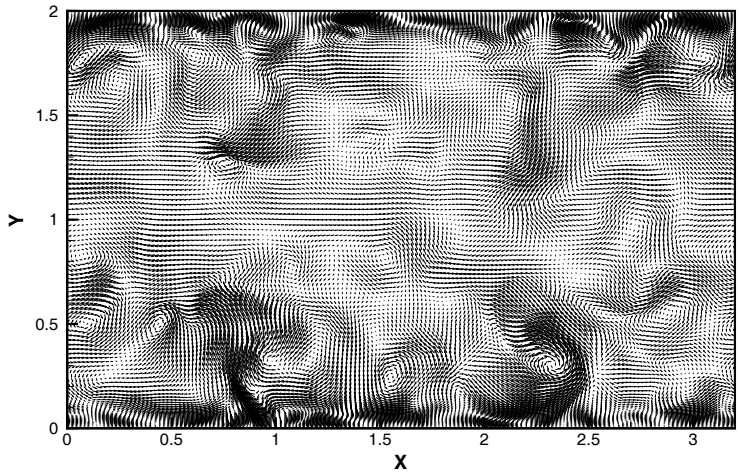

Figure 3.2: Instantaneous velocity vectors at a plane normal to the streamwise direction.

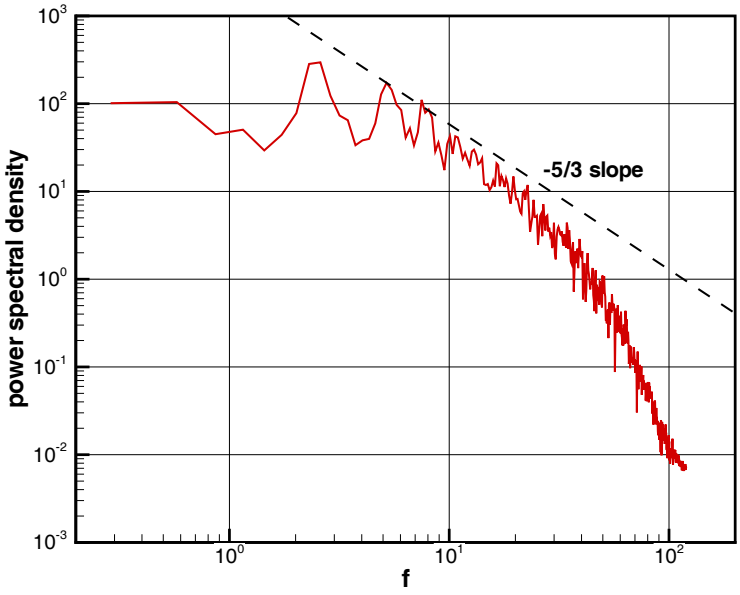

Figure 3.3: Power spectral density of the streamwise velocity fluctuations at the point $y^+ = 121$ away from the wall.

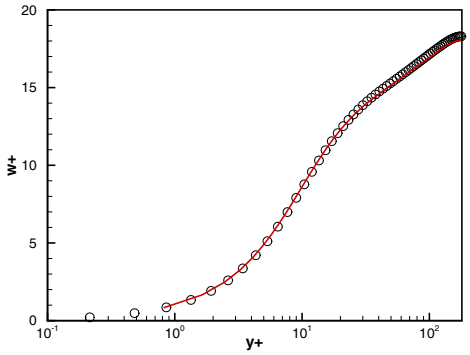

(a) mean streamwise velocity.

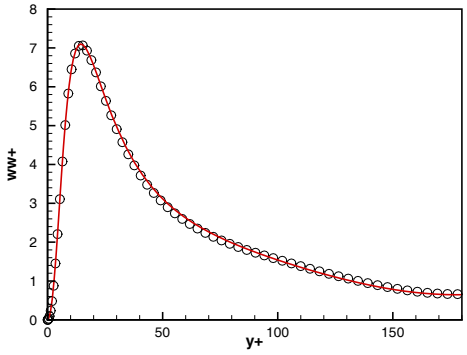

(b) streamwise velocity variance.

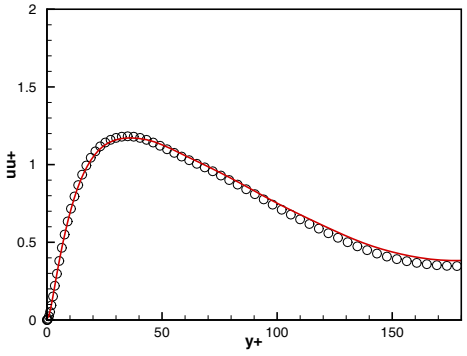

(c) spanwise velocity variance.

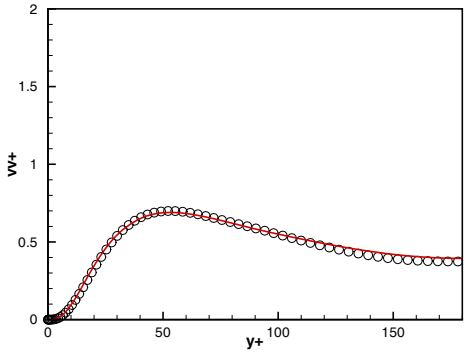

(d) vertical velocity variance.

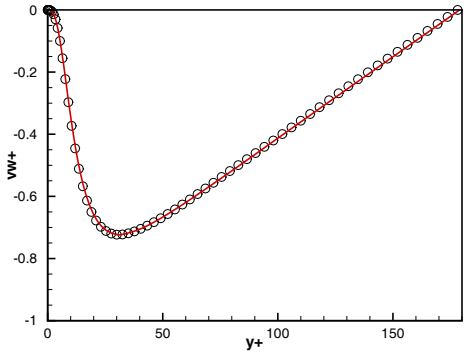

(e) Reynolds shear stress.

Figure 3.4: Computed flow statistics for fully developed channel flow at $Re_\tau = 180$. The solid line and the symbol denote the present computation and the computation by Moser et al. (1999), respectively.

criterion (Jeong and Hussain, 1995) are shown in Figure 3.1 and reveal the highly three-dimensional and complicated structure of the instantaneous flow. Figure 3.2 shows the instantaneous velocity vectors at a plane normal to the streamwise direction. Strong secondary motions induced by the low velocity streaks in the viscous sublayer are observed. Figure 3.3 shows the computed power spectral density of the streamwise velocity fluctuations at the point $y^+ = 121$ away from the wall. The size of the inertial subrange ($-5/3$ slope region) is small because of the low Reynolds number of the simulated flow, and it is seen that the present DNS resolves both the inertial subrange and dissipation range well. The computed mean flow and turbulence statistics are compared with those of the spectral DNS by Moser et al. (1999) (Figure 3.4). Even though the accuracy of the spatial discretization method of the present model is second-order, the agreement between the results of our computation and the spectrally accurate results of Moser et al. (1999) is excellent.

3.2 RANS simulation of fully developed turbulent pipe flow

We simulate fully developed turbulent flow in a straight circular pipe using a RANS models for turbulence closure. The objective of this test case is to demonstrate the accuracy of the boundary condition reconstruction approach in the CURVIB method described in Section 2.3.1 in the context of a RANS simulation. For that, we carry out simulations using both a curvilinear, near-wall resolving, boundary-fitted grid and the CURVIB approach with a wall model to apply boundary conditions on the pipe wall and compare the results of the two simulations. For both simulations, we employ the SST RANS model given by Eqs. (2.9) and (2.10). The Reynolds number of the flow based on the bulk velocity and the diameter of the pipe is $Re = 4 \times 10^4$. The Navier-Stokes and turbulence closure equations are solved in a time accurate manner until the solution becomes steady state with periodic boundary condition specified in the streamwise direction.

The wall resolving RANS computation is carried out using the boundary-fitted, curvilinear grid shown in Figure 3.5(a) to discretize the pipe cross section. 201×201 grid points are employed and the first grid node off the wall is located at $y^+ = 1$. The no-slip boundary condition for the velocity and the low Reynolds number boundary conditions for k and ω are prescribed at the wall of the pipe.

The second simulation is carried out by immersing the wall of the pipe, discretized with a triangular mesh, in a uniform Cartesian grid with 71×71 grid points as shown in Figure 3.5(b). The pipe is treated as an immersed boundary and boundary conditions are specified using the CURVIB method. The near-wall grid spacing for this case is much coarser than the wall-resolving case, with the first grid node off the wall located at $y^+ = 40$. Therefore, velocity and turbulence quantities boundary conditions are

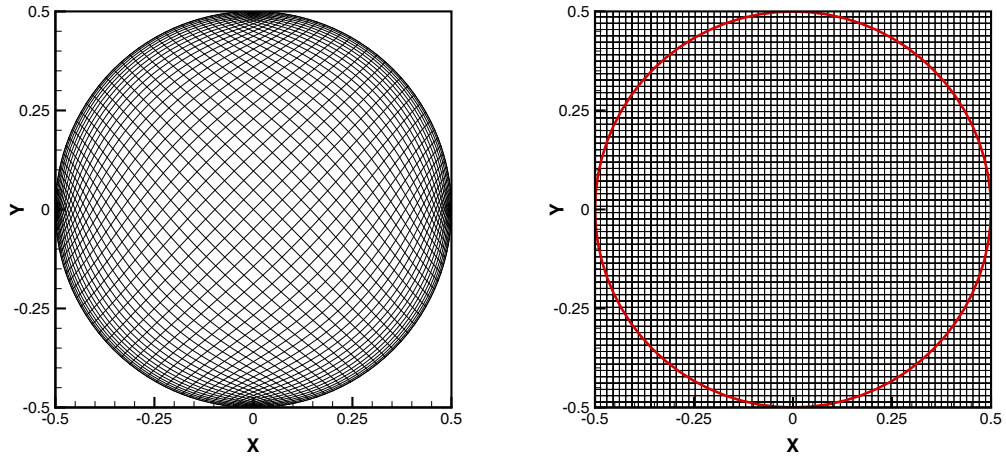

(a) 201×201 grid (every four grid lines are shown). (b) 71×71 grid (the solid red line denotes the immersed boundary).

Figure 3.5: Grids for the turbulent pipe flow computation

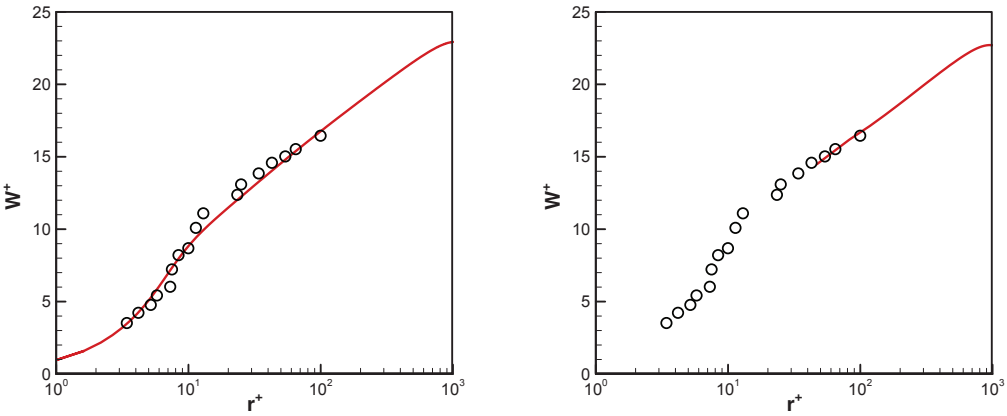

(a) 201×201 grid (boundary-fitted wall resolving grid). (b) 71×71 grid (CURVIB with wall modeling).

Figure 3.6: Comparison of the non-dimensional mean streamwise velocity for the (a) body-fitted wall resolving grid and (b) coarse Cartesian grid with CURVIB wall model (solid line: computation, symbol: measurement by Laufer (1954)).

reconstructed using the wall model described in Section 2.3.2.

The computed non-dimensional streamwise mean velocity profiles for the two cases are shown in Figures 3.6(a) and 3.6(b) and compared with the experimental results (Laufer, 1954). In the figure, $r^+ = u_\tau r/\nu$ implies the distance from the wall in wall units, $W^+ = W/u_\tau$ is the the mean streamwise velocity normalized by the mean shear velocity, r is the distance from the center of the circle, and W is the mean streamwise velocity. For both cases excellent agreement is observed between calculations and measurements. As one would expect, the wall-resolving simulation captures the logarithmic, buffer and laminar sublayer regions of the velocity profile while the CURVIB wall-model simulation can only capture the outer part of the logarithmic region. The agreement between the computation and measurements is very good and demonstrates the correct implementation of the CURVIB wall-model in RANS model.

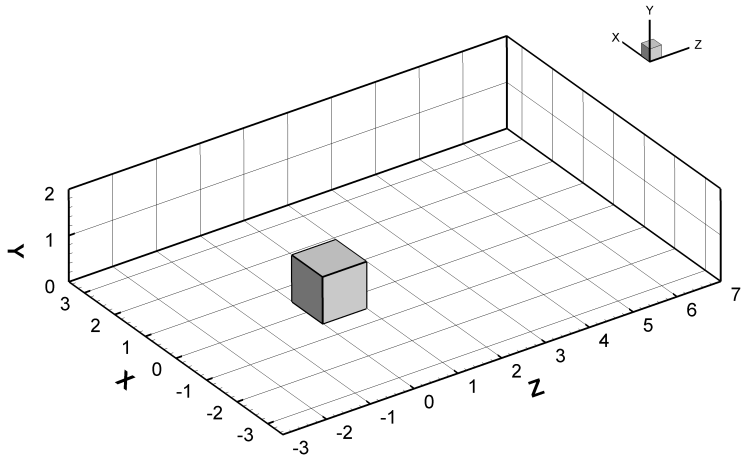

Figure 3.7: Computational domain of turbulent flow around the cubical obstacle.

3.3 LES of channel flow with a wall-mounted cubical obstacle

We carry out LES of turbulent channel flow around a wall-mounted cube in order to demonstrate the accuracy of the LES model implemented in the CURVIB method. The computational domain is shown in Figure 3.7. The Reynolds number based on the height of the cube and the bulk velocity is 4×10^4. The streamwise direction is along the z axis, and the center of the bottom of the cube is located at (0, 0, 0.5). The computational domain extends 7, 2, and 10 cube heights along the spanwise, vertical, and streamwise directions, respectively. The computational grid consists of $121 \times 97 \times 241$ grid points, and the minimum grid spacings near the channel and cube walls are approximately 0.005 and 0.02, respectively. The presence of the cube is handled using the CURVIB method and the wall model described in Section 2.1.3 is used since the near wall grid spacing does not fully resolve the viscous sublayer. Periodic boundary condition is given in the spanwise (x) direction while the instantaneous inflow velocity field is fed from a separate LES of homogeneous turbulent channel flow.

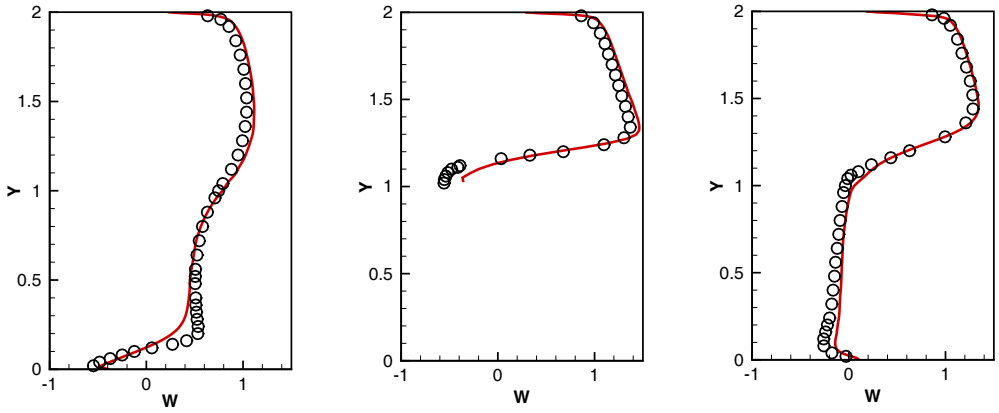

(a) z=-0.25. (b) z=0.5. (c) z=1.08.

Figure 3.8: Comparison of the mean streamwise velocity (solid line: computation, symbol: measurement by Martinuzzi and Tropea (1993)).

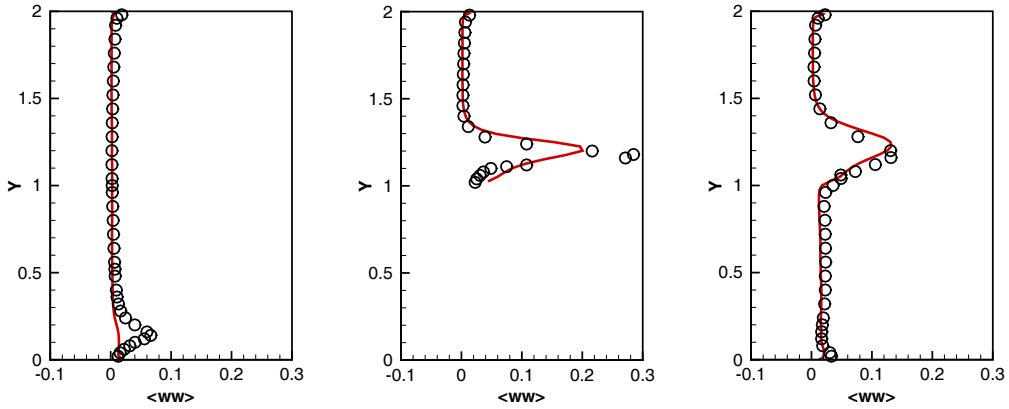

(a) z=-0.25. (b) z=0.5. (c) z=1.08.

Figure 3.9: Comparison of the streamwise velocity variance (solid line: computation, symbol: measurement by Martinuzzi and Tropea (1993)).

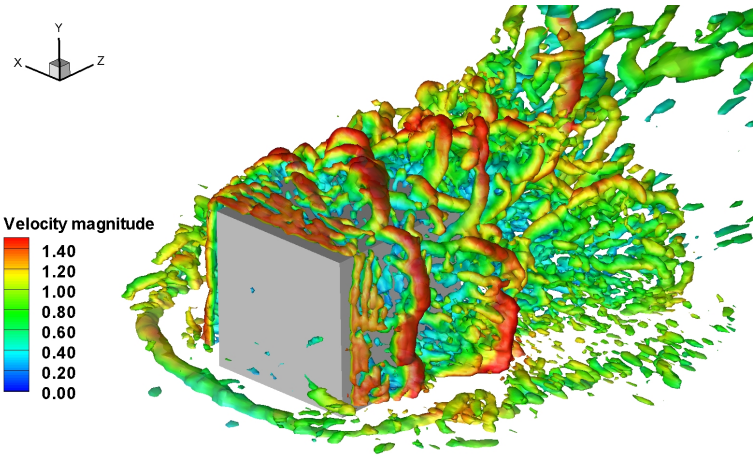

Figure 3.10: Vortical structure (isosurfaces of $\lambda_2 = -15$) around the cube colored by the velocity magnitude.

The computed mean streamwise velocity and streamwise velocity variance are compared with the experimental results (Martinuzzi and Tropea, 1993) at various locations in Figure 3.8 and Figure 3.9, respectively. The solid lines and the symbols in the figures denote the LES computation and the experimental measurement (Martinuzzi and Tropea, 1993), respectively. W and w imply the mean and fluctuating streamwise velocity, respectively, and $< >$ denotes temporal (Reynolds) averaging. The simulations capture the presence of the horseshoe vortex in front of the cube and the presence of recirculating bubbles along the top edge and downstream of the cube as also observed in the measurements. The under-prediction of the velocity variance at z=-0.25 and z=0.5 can be attributed to the coarse grid resolution near the wall. However, the overall agreement between the computed and measured data is good despite the use of the wall model and a rather coarse computational grid. The vortical structures which are identified using the λ_2 criterion (Jeong and Hussain, 1995) around the cube are shown in Figure 3.10. The dynamic horseshoe vortex system that formed in front of the cube as well as the complex web of arch and hairpin vortices shed from the cube are evident in this figure.

Chapter 4

Modeling of turbulent flows in a meandering stream

In this chapter we present the application of the developed LES and URANS models for solving turbulent flows in a field scale natural-like meandering stream. Mean flow characteristics and turbulence statistics are investigated and the computed results are compared with the experimental data.

4.1 SAFL Outdoor StreamLab

To demonstrate the ability of the method to carry out high resolution simulations of flow in a natural stream with arbitrarily complex bathymetry, the numerical model is applied to carry out LES and URANS simulations of turbulent flow in the meandering stream currently installed in the St. Anthony Falls Laboratory (SAFL) Outdoor StreamLab (OSL), University of Minnesota, Minneapolis, MN, USA. This research facility (Figure 4.1) is a 40 m by 20 m basin which has been configured into a sand-bed meandering stream channel that was approximately 50 m long, 2 m wide, and 0.1 m deep at base

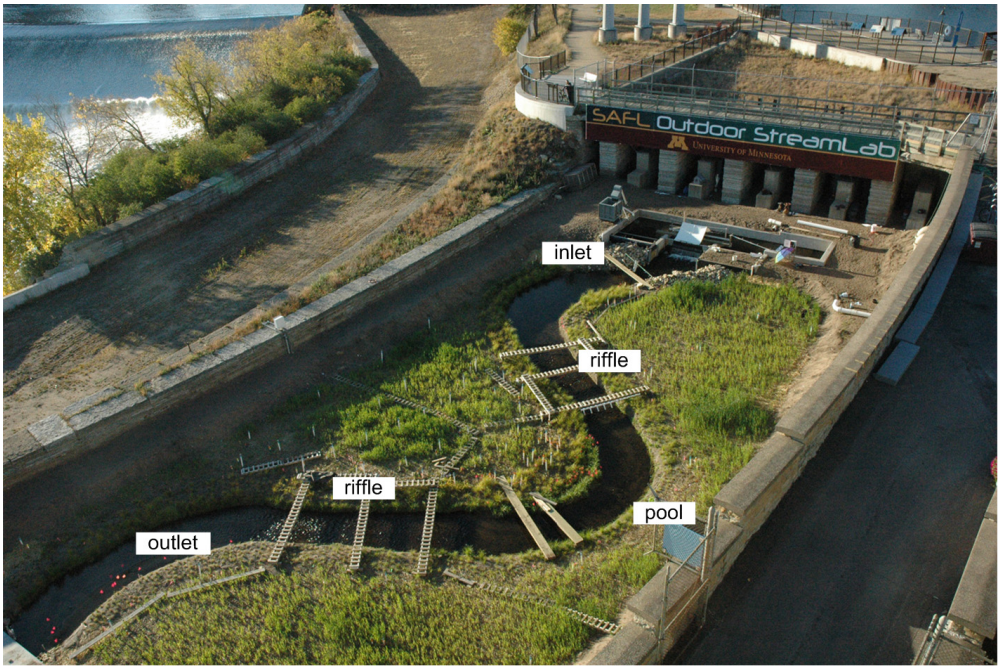

Figure 4.1: Outdoor StreamLab (image courtesy of Anne Lightbody).

flow. Native riparian seedings were planted along the streambank during the first year of operation (2008) along with biodegradable coconut-fiber bank stabilization matting. By 2009, the vegetation had established stable root systems that, along with the remains of the initial coconut fiber matting, stabilized the bank position, The floodplain was seeded with a mixture of native prairie grass seed. Entrance conditions for the OSL allow accurate control and measurement of water and sediment discharge rates, and the facility is outfitted with a sedimentation basin at its downstream end where sediment is collected and stockpiled for recirculation. Simulations and measurements reported herein were performed for a flow rate of 4.45×10^{-2} m^3/s, which yields Reynolds and Froude numbers, based on on average values of depth and velocity, approximately equal to 2.3×10^4 and 0.23, respectively. The flow parameters for the OSL is shown in Table 4.1. Reynolds and Froude numbers are based on the bulk velocity and depth at the inlet.

Three-dimensional mean velocity and turbulence statistics measurements in the OSL were obtained using acoustic Doppler Velocimetry (ADV; Nortek Vectrino and Sontek MicroADV) at 50-Hz for 5 minutes at each location. The ADV probes were mounted to a channel-spanning portable traverse enabling lateral and vertical positioning. At each cross section, the position of this traverse was recorded using a total station (Sokkia X30RK), enabling registration of each sampling location within a common coordinate system. ADV measurements were obtained at twelve channel cross sections located throughout the length of the stream: one directly upstream of the first riffle section, one across the midpoint of each riffle section, eight evenly spaced throughout the middle meander bend, and one spanning the apex of the downstream meander bend. At each cross section, vertical profiles were sampled every 0.25 m laterally at 0.05 m vertical spacing between sampling positions.

Bed and water surface topography in the OSL were collected on a 1-cm horizontal grid at sub millimeter vertical accuracy using instruments mounted to a separate channel-spanning portable carriage, the position of which was registered using the total station. A laser distance sensor (Keyence LK-G series) was used for collecting subaerial bank topography, while a pulser and ultrasonic submersible transducer system (JSR Ultrasonics) documented subaqueous topography. Mean water surface elevation measurements were sampled at 50-Hz over a centimeter-scale spaced grid using an ultrasonic distance sensor (Massa).

The OSL was first run with the given discharge for several days until the bed in the pool region does not change significantly over time, and after that the water and

Case	Flow rate	Reynolds number	Froude number
Base flow	4.4×10^{-2} m$^3/s$	2.4×10^4	0.3
Bankfull flow	2.85×10^{-1} m$^3/s$	10^5	0.4

Table 4.1: Flow parameters for base and bankfull flows.

bed surfaces and velocity data over the whole channel were collected for several weeks. Because of the limited window size of the bed topography scanner the whole stream was divided into many regions where the bed elevation was measured during different times. At each region, bed and water surfaces measured for a finite time were temporally averaged in order to obtain input data for the computation. The bed topography obtained at each region was assembled together to form a single bed topography shown in Figures 4.2 and 4.11. During the time of measurement a long-term morphological change at some regions of the pool was observed, and this was not accounted in the time-averaged bed forms. It is noted that the long-term variability of the bed elevation in some regions was not negligible, and thus non-smooth bed topography inevitably existed at the interface between those regions as it is seen in Figures 4.2 and 4.11. Particularly, there exists noticeable discontinuity of the bed topography near the interface between the first riffle zone and the following pool zone. The measurement error may affect accuracy of local flowfield, but it will be subsequently shown that the overall pattern of mean velocities and large scale motions are not significantly influenced by those errors.

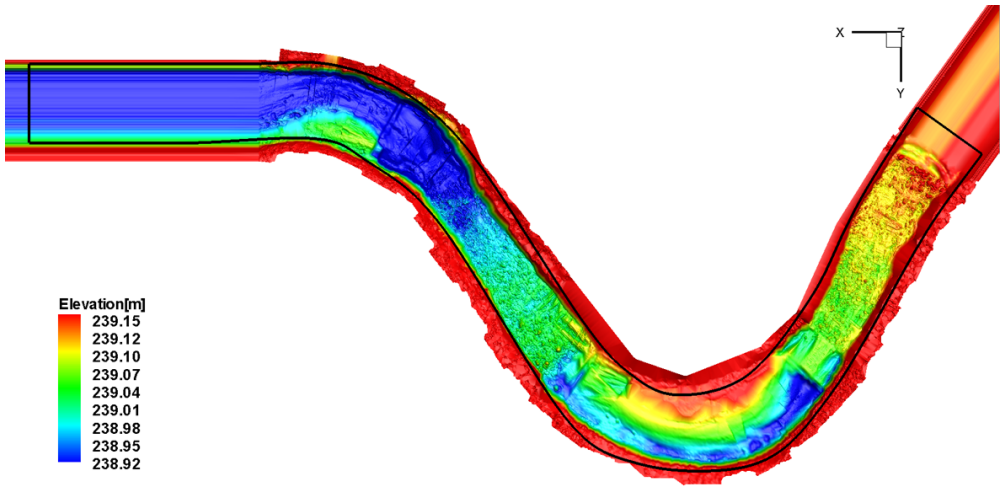

(a) Base flow.

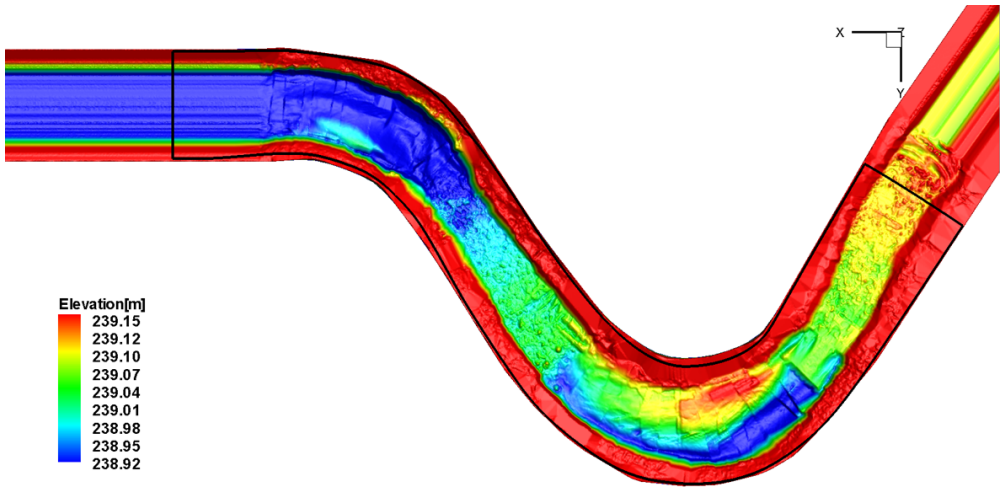

(b) Bankfull flow.

Figure 4.2: The immersed body and the boundary of the background mesh for the base and bankfull flows of the OSL (the solid lines denote the boundary of the background mesh; the flow direction is from right to left).

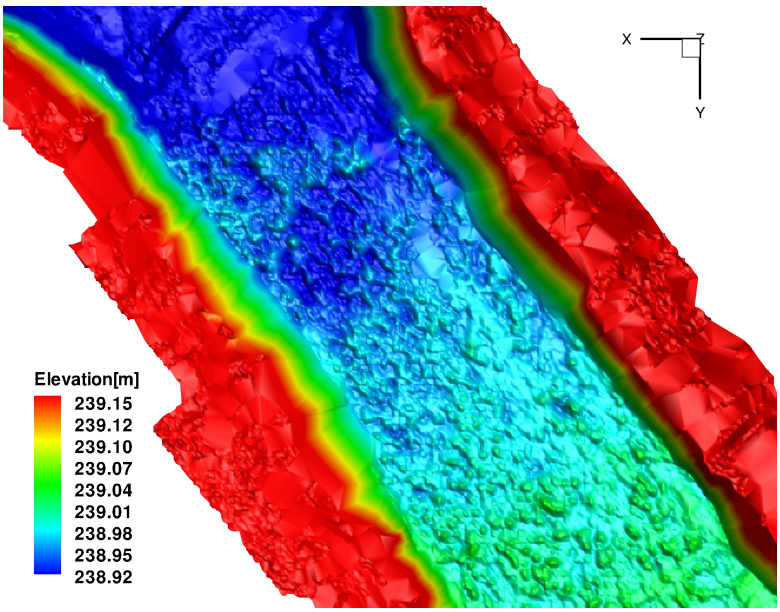

Figure 4.3: The immersed body showing the bed roughness at the second riffle of the OSL (the flow direction is from bottom right to top left).

4.2 Computational setup

The high-resolution scanned bathymetry is shown in Figure 4.2. The flow direction is from right to left and key features of the stream bathymetry include the two riffle zones, which occupy the straight parts between successive curved sections, and one pool zone in between. The measured bathymetry in one of the riffles is shown in Figure 4.3 to illustrate the level of resolution of the various bed features. It is evident from this figure that the measurements resolve individual, centimeter-scale roughness elements on the bed. The measured bathymetry is discretized with an unstructured triangular mesh and embedded in an approximate meandering channel of rectangular cross section as required by the CURVIB method. The outline of the background curvilinear domain used in the simulations of the base and bankfull cases is marked with the two black lines in Figure 4.2.

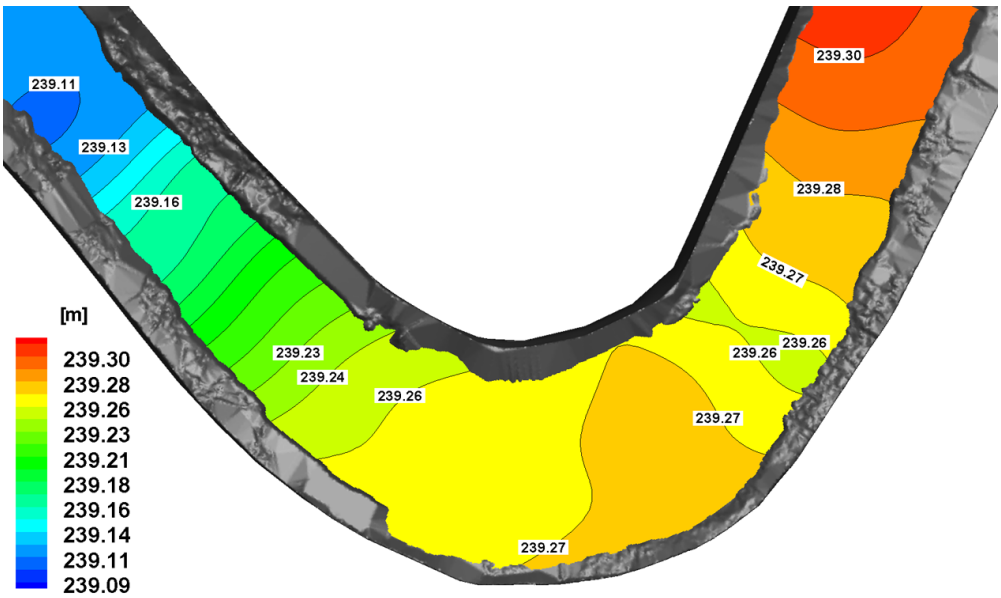

Figure 4.4: Measured water surface elevation of bankfull flow used to define the rigid lid upper boundary in the computational model (the contour levels denote the water surface elevations; the flow direction is from right to left).

The free-surface is treated as a sloping rigid lid on which slip boundary conditions are imposed (see Eqs. (2.27) and (2.28)). This assumption is justified by the relatively low Froude number of the experimental flow (Mcguirk and Rodi, 1978). The shape of the free-surface boundary is prescribed from measurements of the mean water surface elevation. Figure 4.4 shows the free-surface elevation of the bankfull flow.

The background curvilinear mesh discretizing the approximate meandering channel consists of 67 million and 49 million grid nodes for base flow and bankfull flow cases, respectively. The computational grids of the base flow and bank flow cases consist of $3650 \times 301 \times 61$ and $2001 \times 241 \times 101$ nodes in the streamwise, lateral, and vertical directions, respectively. The grid spacing in the three directions for base and bankfull flow simulations is about 1 cm, 1 cm and 1 mm in streamwise, transverse and vertical

directions, respectively. As shown in Figure 4.2, the length of the computational domain for the bankfull flow simulation is shorter than that of the base flow simulation. There are two reasons for using the shorter computational domain in the bankfull flow simulation. First, the influence of the upstream inflow condition on the downstream flowfield was found to be not significant (see Section 5.1.1), and therefore, the length of the computational domain upstream of the first riffle could be shortened. Secondly, regions of interest for the bankfull flow simulation was the regions near the pool and long straight domain at the downstream of the second riffle was unnecessary. For each case, the same grid is employed both for LES and URANS simulations. The wall modeling approach described in Section 2.1.3 is used to compute the velocity boundary conditions at the IB nodes since the present simulation does not resolve the viscous sublayer. It is important to emphasize that the present wall model does not incorporate any roughness effects. This is because in the present geometry roughness elements are almost exclusively found in the two riffles where the computational grid is sufficiently fine to directly resolve most of the key geometric features of the bed. As such, the complex bed bathymetry is treated as smooth wall and the presence of roughness is incorporated by resolving directly flow structures around individual, small scale obstacles, e.g. small rocks, on the stream bed.

For the LES, inflow boundary conditions are prescribed at the inlet of the flow domain by feeding instantaneous velocity fields obtained from a separate LES of fully developed flow in a straight open channel with the same cross section as that of the inlet OSL cross section and at the same Reynolds number. For the URANS simulations, which are carried out using both the $k - \omega$ and SST models, steady, time-averaged velocity profiles that match the measured flow rate is prescribed. Neither of these inflow conditions are likely to accurately represent the flow at the same location in the OSL for which the entrance flow is supplied through a head box (see Figure 4.1) and is

highly turbulent and three-dimensional. The impact of inflow boundary conditions on the predictive capabilities of the model will be discussed in great detail in Section 5.1.1 below. The time steps for the numerical simulations are chosen as 0.001 s and 0.002 s for base and bankfull flows, respectively.

The simulations are carried out using 160 MPI (message passing interface) processors. The LES and RANS simulations were first run until the total kinetic energy in the computational domain reached steady-state and subsequently the flowfields were averaged for approximately t=60 s and 5 s, respectively. The URANS equations are solved in a time-accurate (or unsteady) manner, however, the instantaneous flowfield computed by the URANS model showed little difference with the flowfields averaged for 5 s, and it implies the URANS simulations reached steady-state and no significant unsteadiness is observed.

4.3 LES and URANS modeling of base flow

Snapshots of the calculated instantaneous flow fields at the water surface and near the bed in the riffle region obtained by the LES are shown in Figure 4.5. It is evident from the figure that the LES resolves very complex flow features at the water surface that are the result of the complex and highly heterogeneous bed bathymetry in the riffle region, including intense shear layers and regions of recirculation. The snapshot of the flow at the plane near the bed clearly demonstrates the ability of the method to simulate flow patterns around discrete roughness elements, such as high velocity streaks and vortex shedding around small-scale bed roughness.

Contours of mean velocity magnitude at the water surface computed by the LES and URANS models are shown in Figure 4.6. The velocity magnitudes in the riffle zones predicted by the LES and the SST models are very similar to each other, while the $k-\omega$ model predicts overall higher velocity magnitudes. Some important differences among the three models are also observed in the pool region between the two riffles. The LES predicts the existence of a thin shear layer emanating from the inner bank and ultimately diffusing along the outer bank just upstream of the second riffle. This shear layer is presumably formed due to the sudden expansion of the cross sectional area between the riffle and pool regions and the strong curvature of the bend. This feature of the flow is not captured by either URANS model.

The turbulence kinetic energy (TKE) contours at the surface computed by the LES and the two URANS models are shown in Figure 4.7. The LES and the SST models yield qualitatively similar results and overall similar levels of TKE. A strikingly different prediction is obtained, however, by the $k-\omega$ model with the overall TKE levels in the two riffle regions being nearly one order of magnitude higher than those obtained by the LES and the SST model. Considering that the maximum measured TKE in the riffle zones was in the range of 0.01-0.02 m^2/s^2, the k-ω model significantly over-predicts the

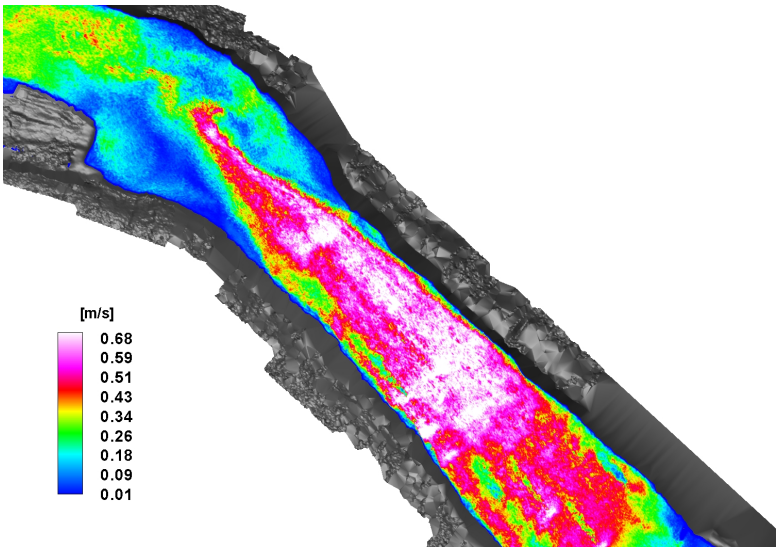

(a) At the water surface.

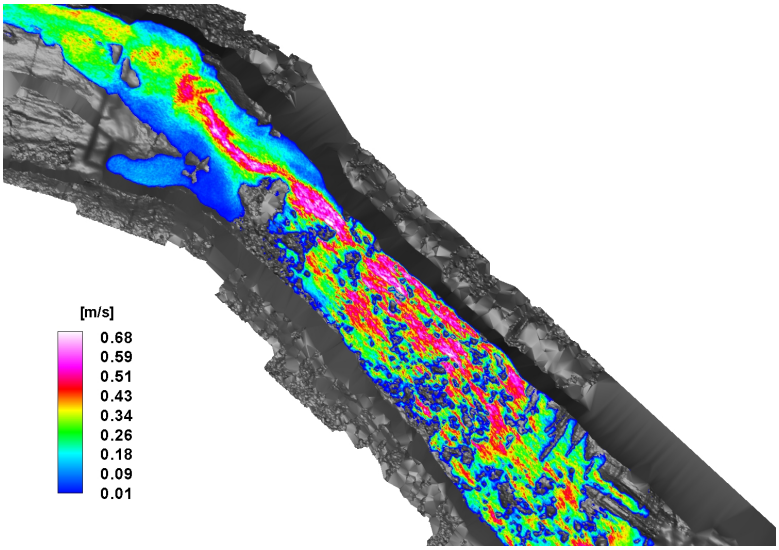

(b) Near the bed.

Figure 4.5: Instantaneous velocity magnitude for the base flow computed by the LES model (the flow direction is from right to left).

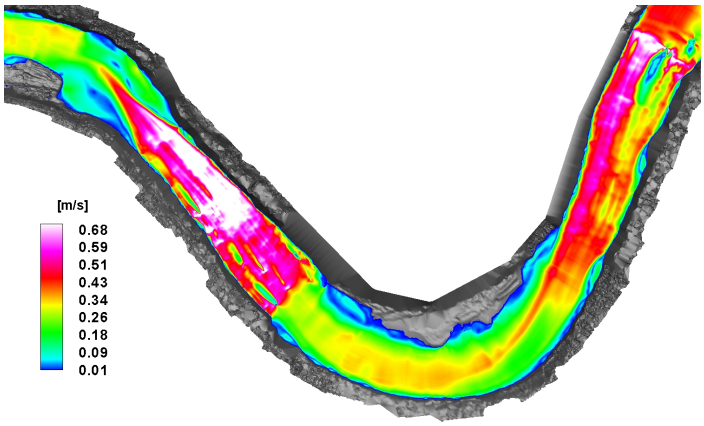

(a) LES model.

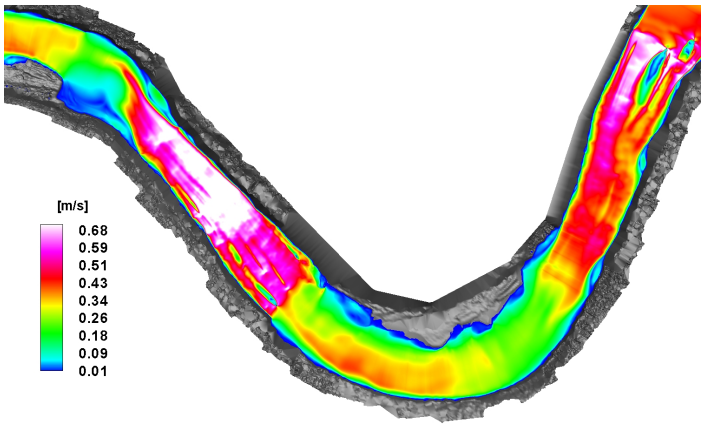

(b) SST RANS model.

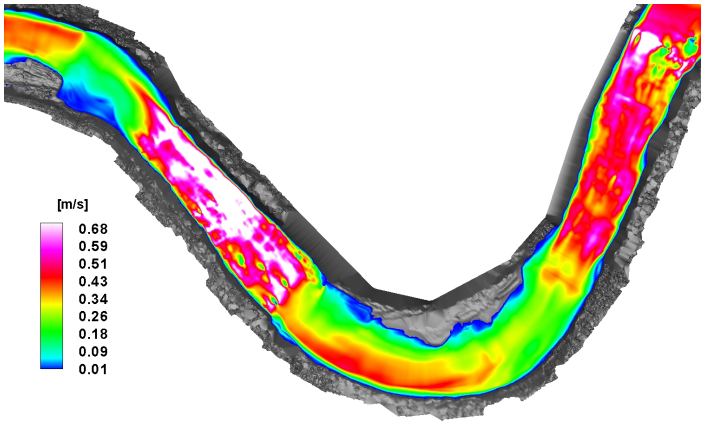

(c) $k-\omega$ RANS model.

Figure 4.6: Computed mean velocity magnitude contours at the water surface for the base flow (the flow direction is from right to left).

magnitude of the TKE while the values predicted by the LES and the SST model are qualitatively correct. Durbin (1996) pointed out that two equation models predict an anomalously large growth of TKE in stagnation point flow. Since the spatial resolution of the present simulations in the riffle zones is high enough to resolve discrete roughness elements, there are many stagnation regions in the flow (e.g. around each roughness element) where the non-physical TKE is produced. Since the SST model employs a limiter for the production term (Eq. (2.12)), its predictions do not suffer from this anomaly.

Figure 4.8 shows the computed mean flow streamlines at selected two-dimensional cross sections near the bend. The LES result shows the formation of a large secondary flow cell rotating in the counter-clockwise direction such that the near bed flow moves from the outer to the inner back cell. This cell is the well-known inner bank cell ((Thomson, 1876)) which is induced by the curvature of the bend and the associated imbalance between the transverse pressure gradient and the centrifugal force near the bed. The inner bank cell is seen in Figure 4.8(a) to dominate the flow throughout the bend. Initially it is located close to the bed but subsequently is seen to rise somewhat and approach the surface toward the end of the bend. Smaller secondary flow cells are also observed near the inner bank, which appear to grow and interact with the primary inner bank cell. Another striking feature of the secondary flow that follows from Figure 4.8(a) is the growth of s small secondary flow cell located near the junction of the outer bank and the free-surface and rotating in the clockwise direction. This cell appears to develop at approximately the apex of the bend and decays before the end of curvature is reached. This is the so-called outer bank secondary flow cell, which has also been observed in laboratory experiments with curved open channels (Blanckaert and de Vriend, 2004) and also documented in field studies (Hey and Thorne, 1975; Bathurst et al., 1979; Thorne et al., 1985). The physics of the inner and outer bank cells and

the underlying mechanisms that drive them will be discussed in detail in Chapter 5. The secondary flow predicted by the two RANS models exhibits the inner bank cell but overall the computed patterns are simpler and more diffused than those obtained with LES (See Figure 4.8). A striking finding is that neither RANS model captures the outer bank cell. As we will discuss below, this is to be expected since turbulence anisotropy plays a major role in the formation of the outer bank cell (Blanckaert and de Vriend, 2004; Balen et al., 2009; Stoesser et al., 2010) and as such isotropic RANS models are inherently incapable of resolving it.

Figure 4.9 shows few selected locations within the pool region where measured velocity and TKE profiles are compared with the computed results in Figure 4.10. All models capture the mean streamwise (Figures 4.10(a)-4.10(e)) and transverse (Figures 4.10(f)-4.10(j)) velocity velocity profiles with reasonable accuracy. This level of agreement is overall consistent with the reasonable agreement between the mean velocity contours at the water surface predicted by all three models in the region between the two riffles as shown in Figure 4.6. The counterclockwise secondary flow (the positive transverse velocity is toward the outer bank) is observed both in the computed and measured transverse velocity profiles suggesting that all three models capture correctly the magnitude of the secondary motion at least in the region where measurements were carried out. The agreement between the computed and measured TKE profiles (Figures 4.10(k)-4.10(o)) is not as good as that for the mean velocities but the results of the LES and SST RANS models are in better overall agreement with the measurements than the k-ω model, which over-predicts significantly the TKE magnitude near the bed.

Overall the agreement between the computed results by LES and SST RANS models with the measurements is reasonable. This finding is especially encouraging when one takes into account the inherent uncertainties in carrying out measurements in a field scale stream like the OSL and the fact that all simulations were carried out without

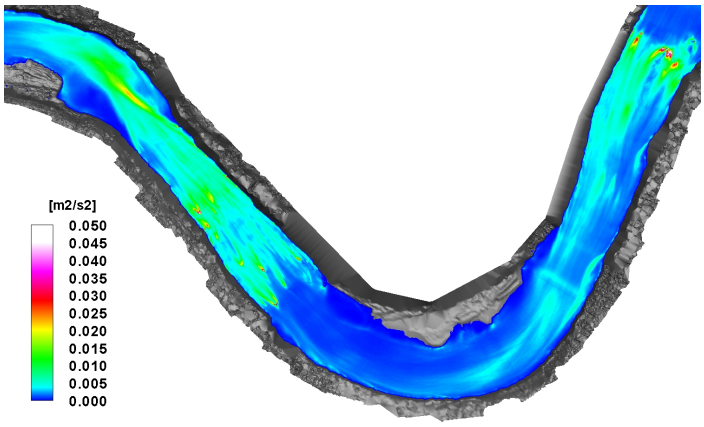

(a) LES model.

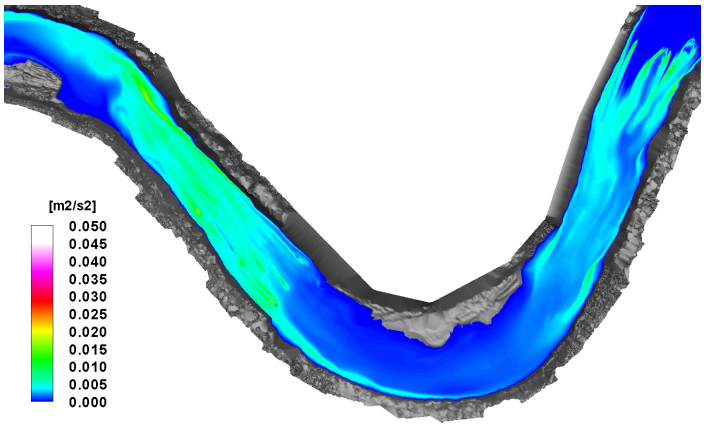

(b) SST RANS model.

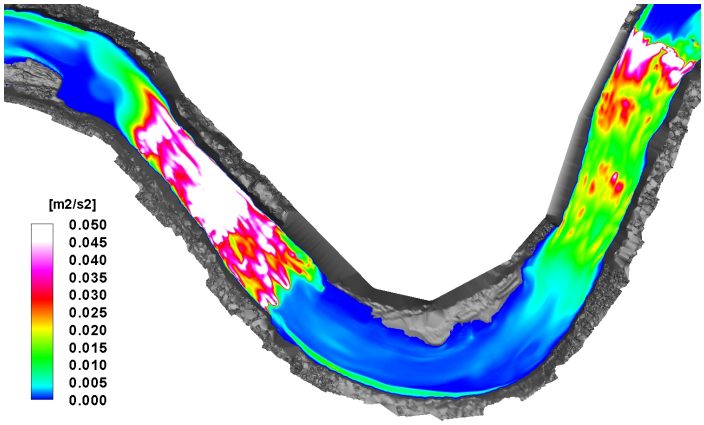

(c) $k-\omega$ RANS model.

Figure 4.7: Computed turbulence kinetic energy contours at the water surface for the base flow (the flow direction is from right to left).

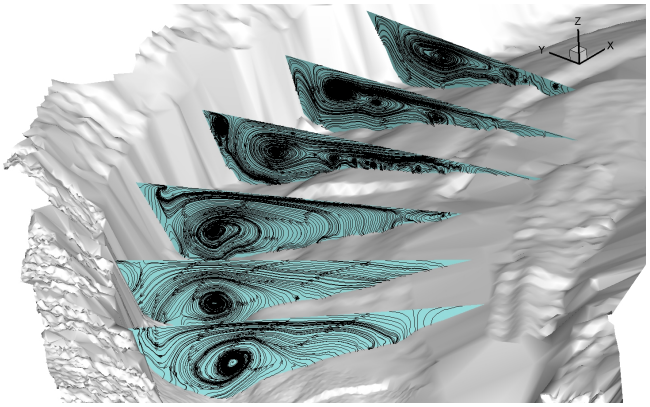

(a) LES model.

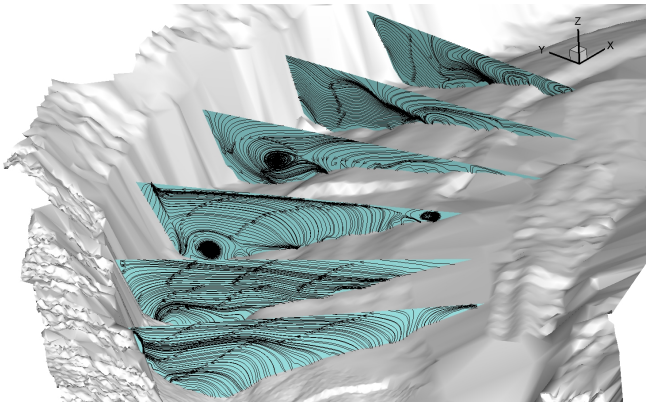

(b) SST RANS model.

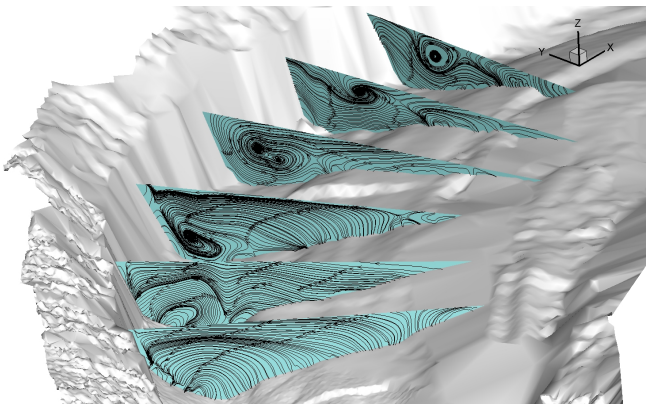

(c) $k-\omega$ RANS model.

Figure 4.8: Computed mean two-dimensional streamlines for the base flow at cross sections near the bend (the flow direction from bottom to top).

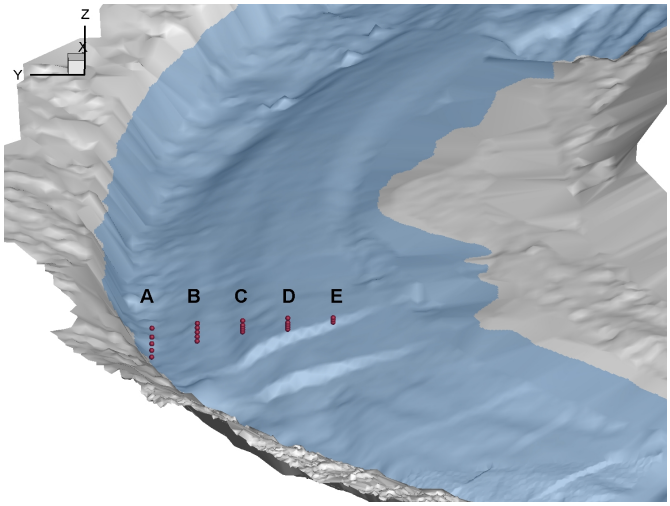

Figure 4.9: Velocity measurement locations near the bend for the base flow (gray and blue surfaces denote bed and water surfaces, respectively; the red symbols denote the locations of the ADV measurement points; the flow direction is from bottom to top).

any calibration against the measured data. It is also important to point out, however, that the results presented in this section underscore the difficulties in validating computational models in natural streams. Based on the comparisons with the limited mean velocity measurements and turbulence statistics measurements, both the LES and SST RANS models yield reasonable results. Yet a more global examination of the flow patterns obtained with the two models (velocity contours at the surface, secondary flow patterns, etc.) reveal significant differences that could lead to a different conclusion regarding their respective predictive capabilities.

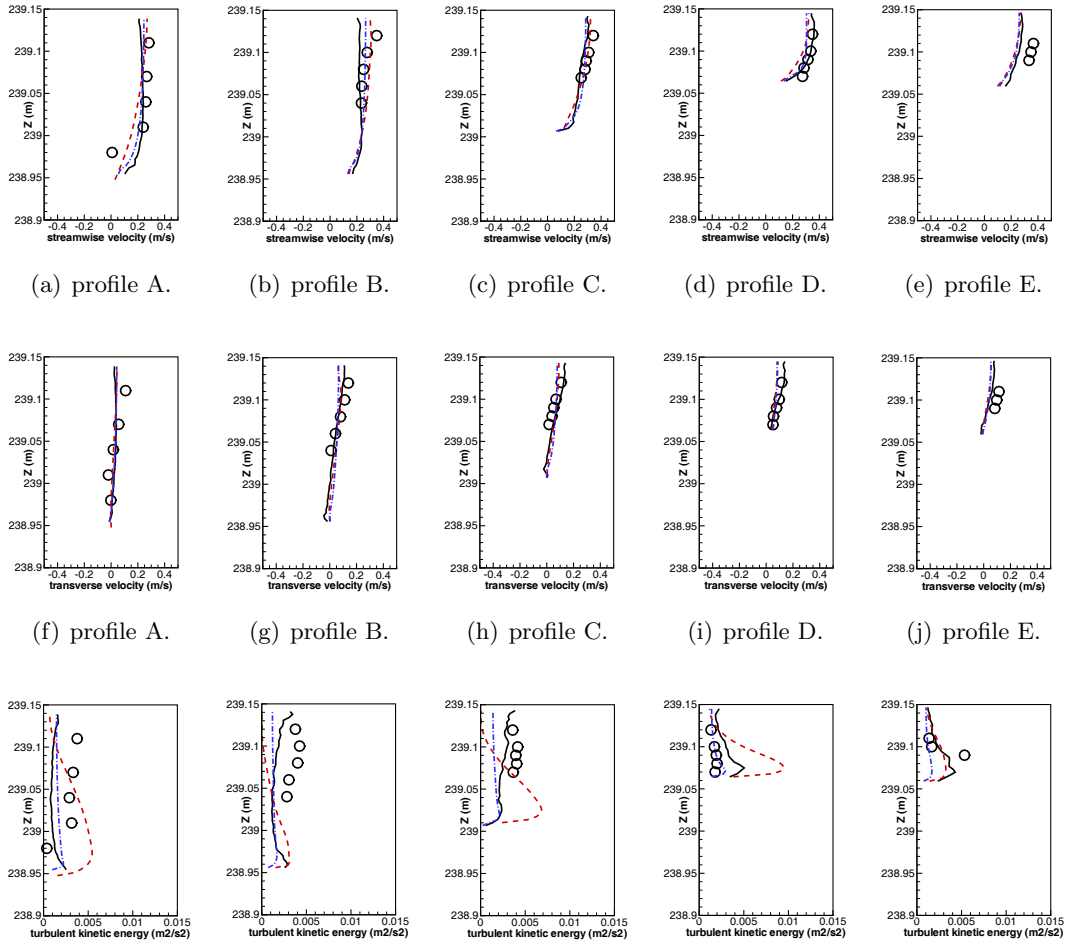

(a) profile A. (b) profile B. (c) profile C. (d) profile D. (e) profile E.

(f) profile A. (g) profile B. (h) profile C. (i) profile D. (j) profile E.

(k) profile A. (l) profile B. (m) profile C. (n) profile D. (o) profile E.

Figure 4.10: Comparison of the mean streamwise velocity (the first row), the mean transverse velocity (the second row), and the turbulence kinetic energy (the third row) with the measurement for the base flow. (black solid line: LES, red dashed line: $k-\omega$, blue dash dotted line: SST, symbol: measurement)

4.4 LES and URANS modeling of bankfull flow

Because the base flow simulation presented in the previous section showed that the SST model predicts mean velocity and TKE better than the $k - \omega$ model, only the SST model is employed for the URANS simulation of the bankfull flow.

Figure 4.11 shows the locations where velocity measurements were obtained. Two cross sections (A and D) were placed near the downstream end of the first and second riffles, respectively, while the other two measurement cross section (B and C) were located within the meander bend. In each cross section, measurements were carried out at four profiles with 4-6 vertical measurement points. As shown in Figure 4.11, the profile locations are numbered from the inner bank to the outer bank.

Figures 4.12, 4.13, 4.14 and 4.15 compare the computed, with LES and SST RANS models, mean velocity and TKE profiles with the measurements at cross sections A, B, C and D, respectively. The first and second letters of the captions in those figures denote locations of the cross section and the profile, respectively. It is seen that both LES and RANS models produce results which are in good overall agreement with the measurements. Notice in particular that the computed transverse velocity component is predicted reasonably well, both in terms of its sign and magnitude, which points to the conclusion that both LES and RANS models captures the magnitude of the secondary motion within the bend with good accuracy. It is also worth noting the that overall level of agreement between the simulations and the experiments improves somewhat from cross section B and beyond. Recall that the inflow conditions prescribed at the start of the computational domain were obtained from a measured velocity and a separate LES of flow in a straight channel with cross section that of the inlet cross section for the URANS simulations and LES, respectively. Such inflow conditions are unlikely to accurately represent the state of the actual flow at the inlet, which enters the OSL stream from the head-box flow control structure as shown in Figure 4.1. The

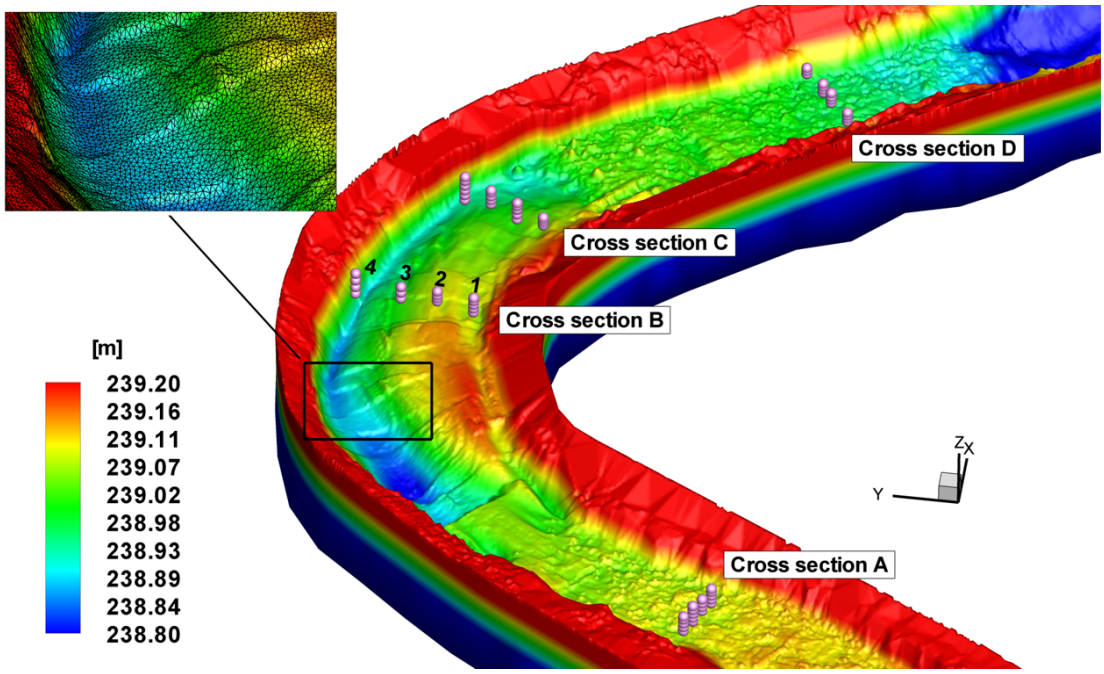

Figure 4.11: The SAFL Outdoor StreamLab bathymetry obtained from high resolution measurements for the bankfull flow. The streambed is discretized using $236,370$ triangular elements and treated as an immersed boundary. The contour levels denote bed elevations. The symbols and numbers mark velocity measurement locations. The flow direction is from bottom to top.

overall good agreement between measurements and experiments, especially downstream of the first riffle, points to the conclusion that the riffle acts to homogenize the flow, causing it to accelerate and increasing significantly turbulent mixing (see below), thus, minimizing upstream memory effects. This is an important finding of this work since prescribing inflow conditions in numerical simulations of natural streams is not only challenging for the OSL but for any field case as well. This issue will be discussed in more detail in Chapter 5.

The overall level of agreement between experiments and simulations emerging from Figures 4.12, 4.13, 4.14 and 4.15 is particularly encouraging when one considers the uncertainties inherent in our numerical model and the fact that no attempt was made to calibrate the model in any way. These uncertainties include: 1) the dynamic bed morphologic condition and the fact that it was not possible to scan the entire bed simultaneously as discussed above; 2) the aforementioned uncertainties in the inflow boundary conditions, which are likely to impact the accuracy of the flow in the vicinity for the first riffle; 3) the possible influence of the sand roughness in the pool zone, which was not taken into account; and 4) the effect of vegetation planted on the streambank on the flow.

Although the RANS simulation was run in unsteady mode, no unsteadiness was observed and the solution obtained from the URANS simulation finally converged to the steady-state. To quantify the range of scales of motion resolved by the LES we plot in Figure 4.16 the one-dimensional power spectral density of the computed streamwise velocity fluctuations at two representative locations in the second riffle zone and the pool, respectively. At both locations there exist three distinct regions in the spectrum: the production range (-1 slope), the inertial subrange ($-5/3$ slope), and the dissipation range with the steep slope at high frequencies. The production range represents the production of TKE by low frequency coherent structures while the inertial subrange

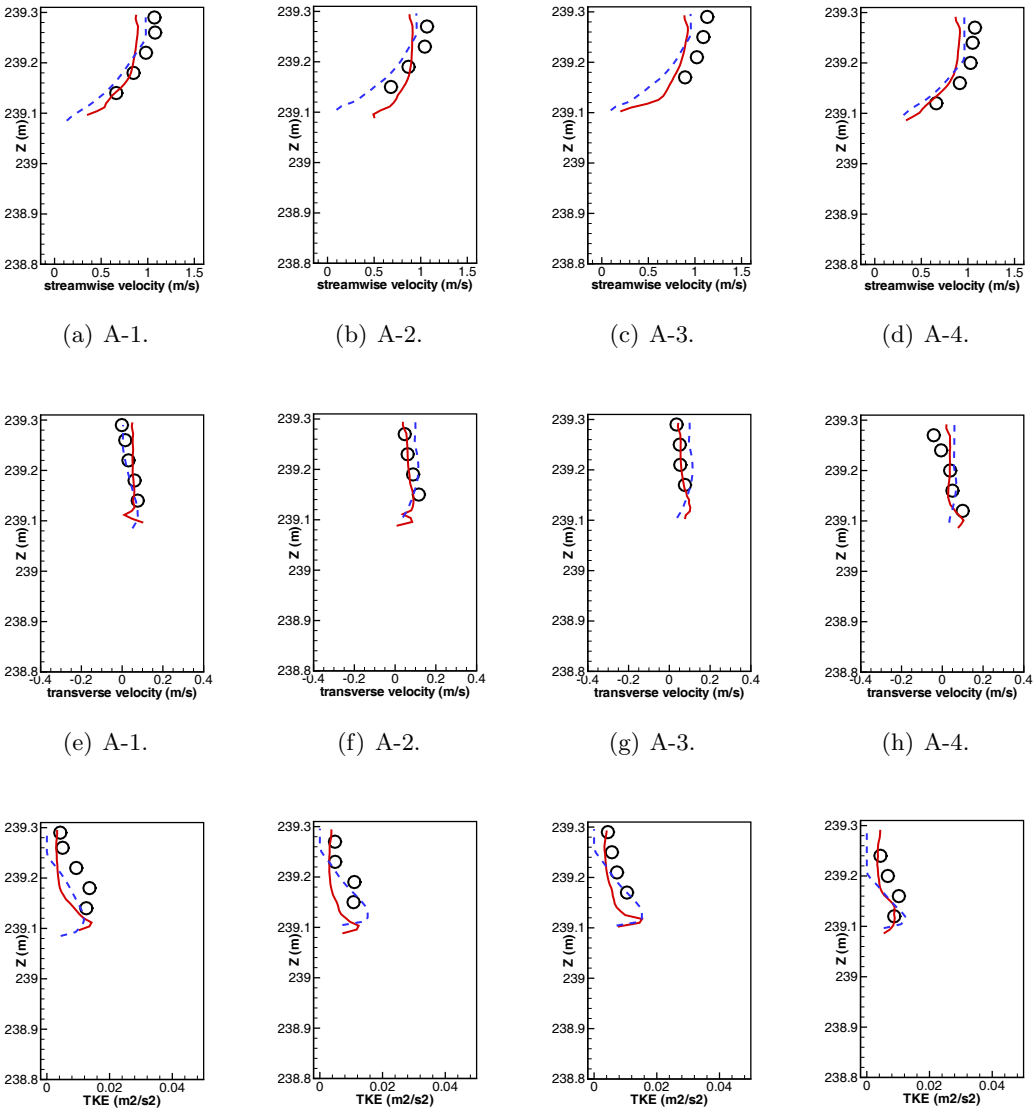

(a) A-1. (b) A-2. (c) A-3. (d) A-4.

(e) A-1. (f) A-2. (g) A-3. (h) A-4.

(i) A-1. (j) A-2. (k) A-3. (l) A-4.

Figure 4.12: Comparisons of mean streamwise velocity, mean transverse velocity, and TKE with the measurements at the cross section A for the bankfull flow (solid line: LES, dashed line: SST RANS model, symbol: measurements). The locations of the cross section and each profile within a cross section are defined in Figure 4.11.

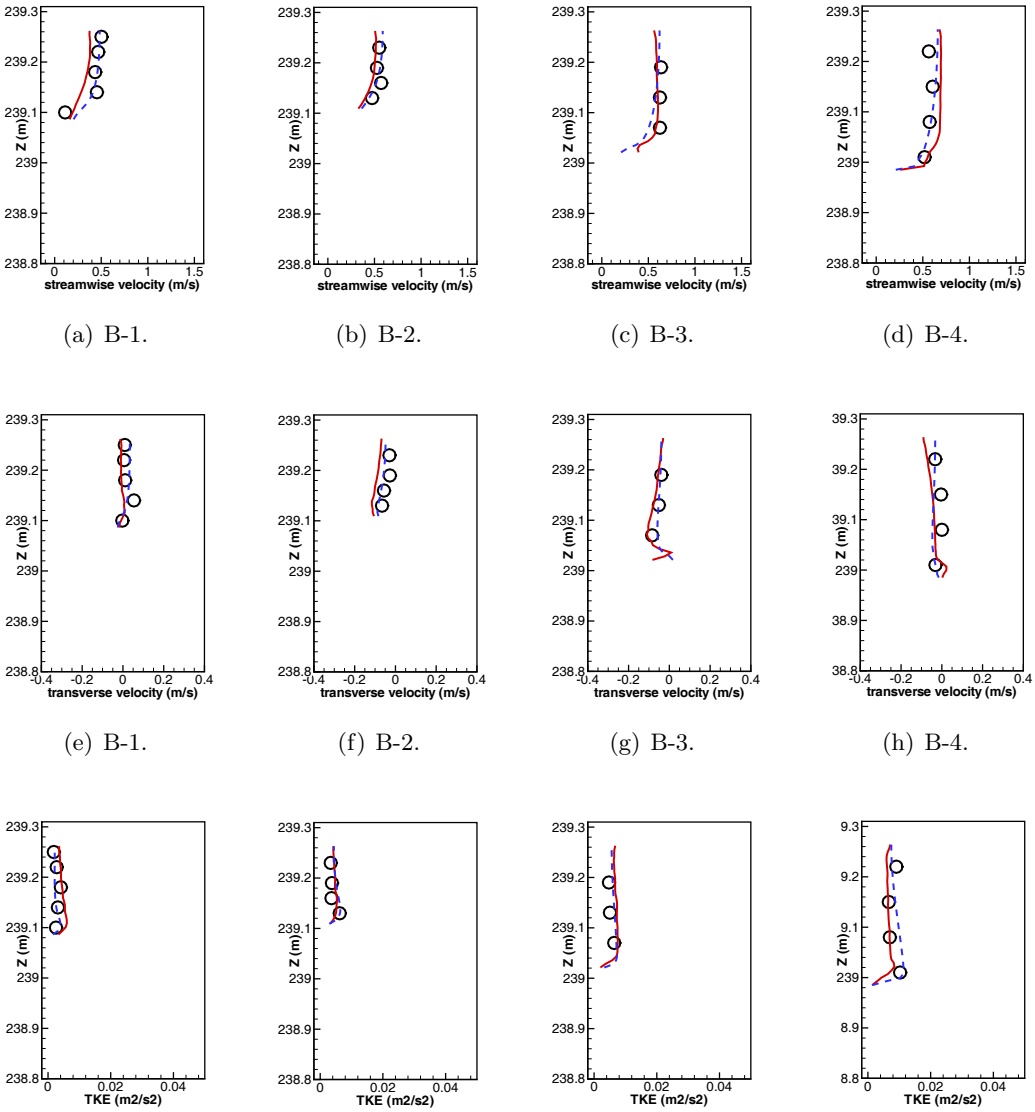

(a) B-1. (b) B-2. (c) B-3. (d) B-4.

(e) B-1. (f) B-2. (g) B-3. (h) B-4.

(i) B-1. (j) B-2. (k) B-3. (l) B-4.

Figure 4.13: Comparisons of mean streamwise velocity, mean transverse velocity, and TKE with the measurements at the cross section B for the bankfull flow (solid line: LES, dashed line: SST RANS model, symbol: measurements). The locations of the cross section and each profile within a cross section are defined in Figure 4.11.

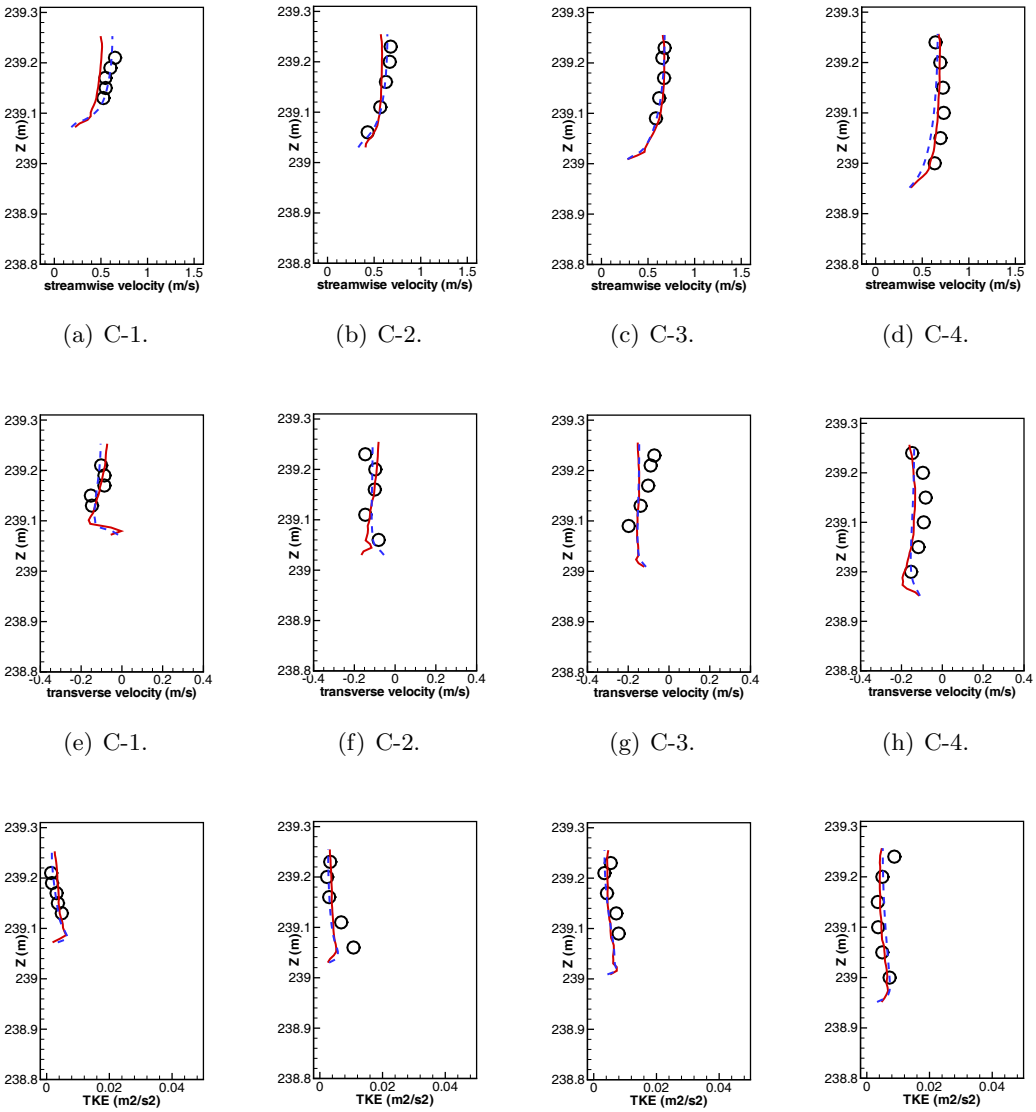

(a) C-1. (b) C-2. (c) C-3. (d) C-4.

(e) C-1. (f) C-2. (g) C-3. (h) C-4.

(i) C-1. (j) C-2. (k) C-3. (l) C-4.

Figure 4.14: Comparisons of mean streamwise velocity, mean transverse velocity, and TKE with the measurements at the cross section C for the bankfull flow (solid line: LES, dashed line: SST RANS model, symbol: measurements). The locations of the cross sections and each profile within a cross section are defined in Figure 4.11.

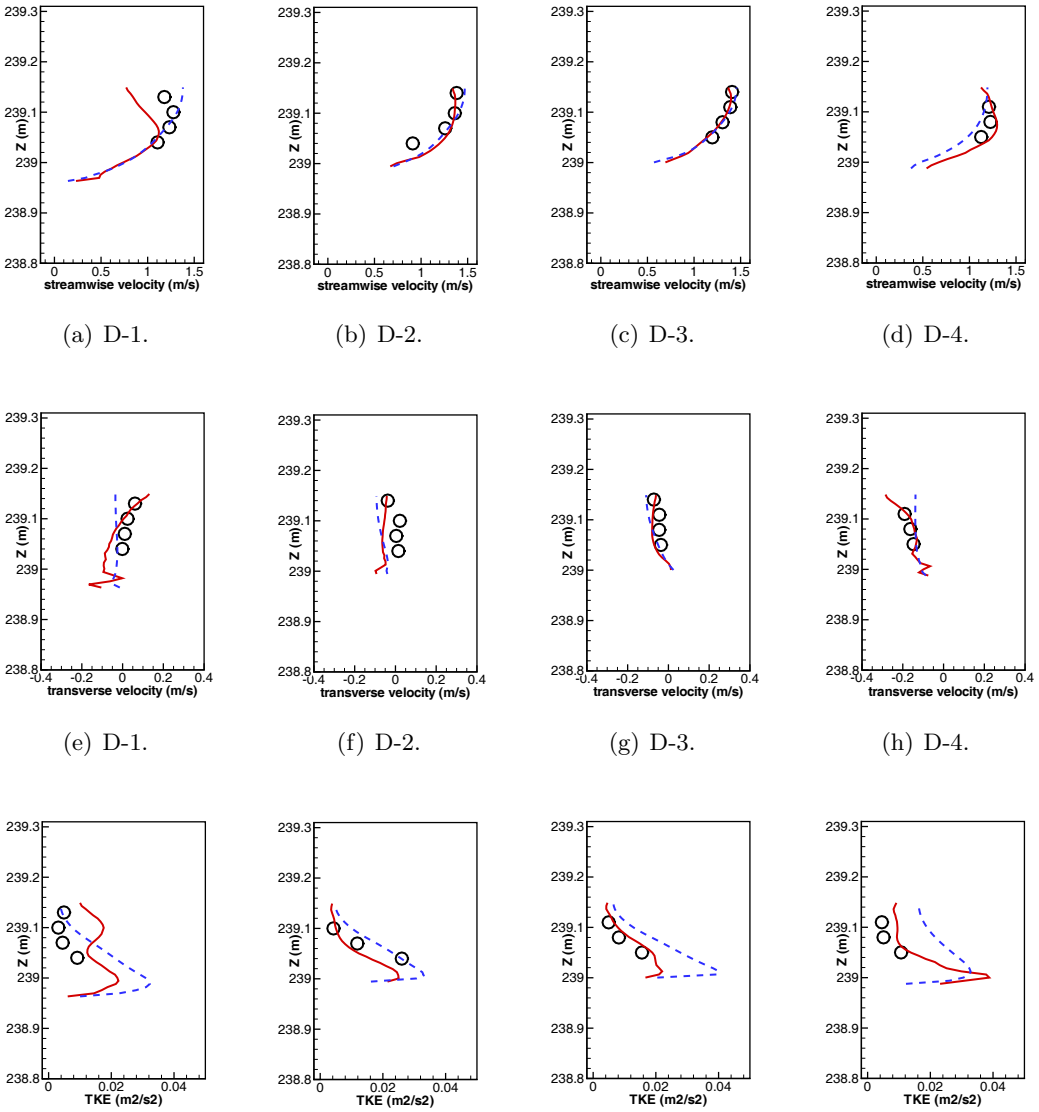

(a) D-1. (b) D-2. (c) D-3. (d) D-4.

(e) D-1. (f) D-2. (g) D-3. (h) D-4.

(i) D-1. (j) D-2. (k) D-3. (l) D-4.

Figure 4.15: Comparisons of mean streamwise velocity, mean transverse velocity, and TKE with the measurements at the cross section D for the bankfull flow (solid line: LES, dashed line: SST RANS model, symbol: measurements). The locations of the cross section and each profile within a cross section are defined in Figure 4.11.

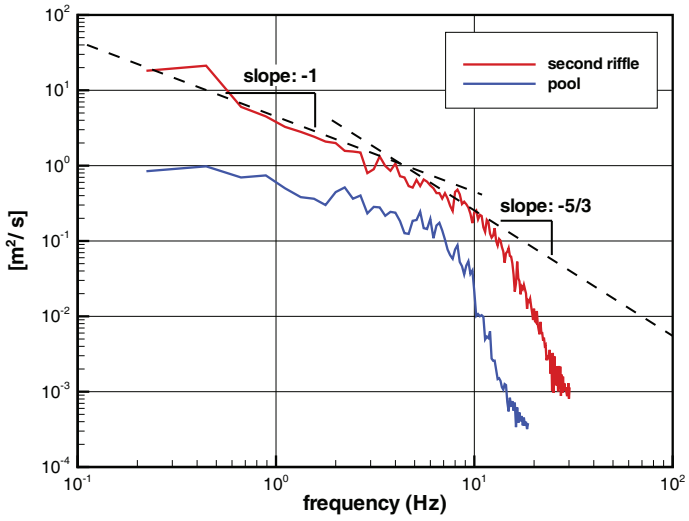

Figure 4.16: Power spectral density of the computed streamwise velocity fluctuations at locations in the second riffle and the pool for the bankfull flow.

marks the cascade of the energy from the larger to smaller eddies. Finally, the dissipation range indicates the dissipation of energy occurring at the sub-grid level due to molecular and SGS viscosities. The cut-off frequency of the spectrum in the riffle and the pool is located approximately at 30 Hz and 20 Hz, respectively. Therefore, our LES resolves accurately temporal scales larger than approximately 0.03 s and 0.05 s in the riffle and pool regions, respectively.

Figures 4.17 and 4.18 show the contours of the mean streamwise velocity and the TKE at the water surface, respectively, computed by using the LES and URANS models. The mean velocity contours computed by the LES model (see Figure 4.17(a)) show the jet-like mean flow structure at the interface between the first riffle and the pool. Two thin free shear layers with high levels of TKE are observed along the boundary of the jet flow (see Figure 4.18(a)). Figure 4.17(a) also shows the presence of the large region with negative streamwise velocities near the inner bank of the bend, which marks the presence

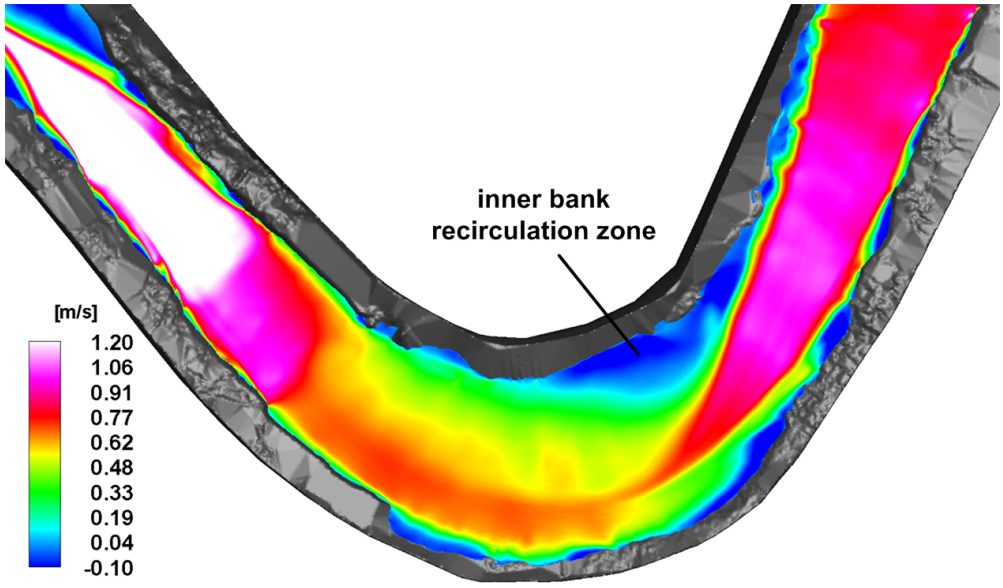

(a) LES model.

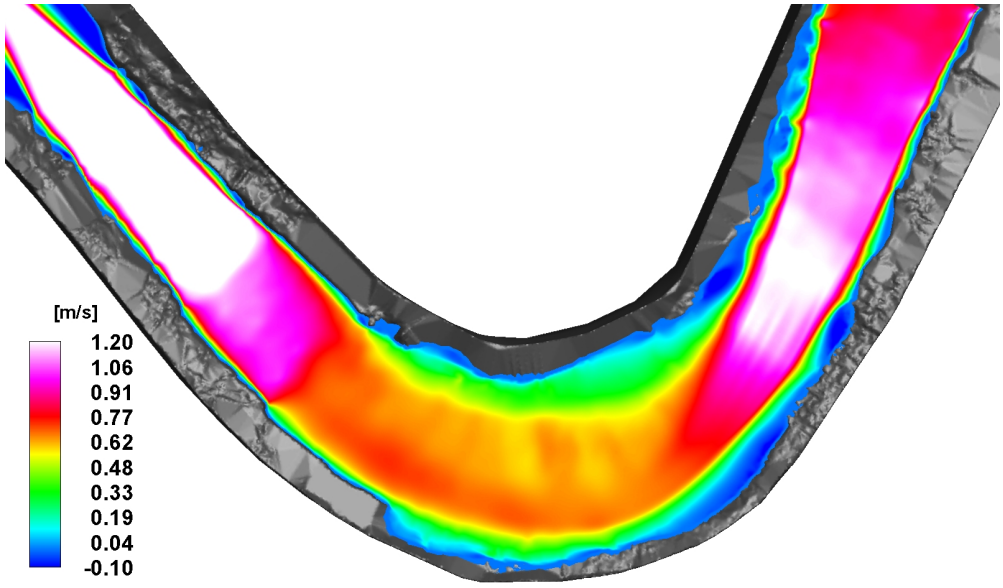

(b) SST RANS model.

Figure 4.17: Computed mean streamwise velocity contours at the water surface for the bankfull flow (the flow direction is from right to left).

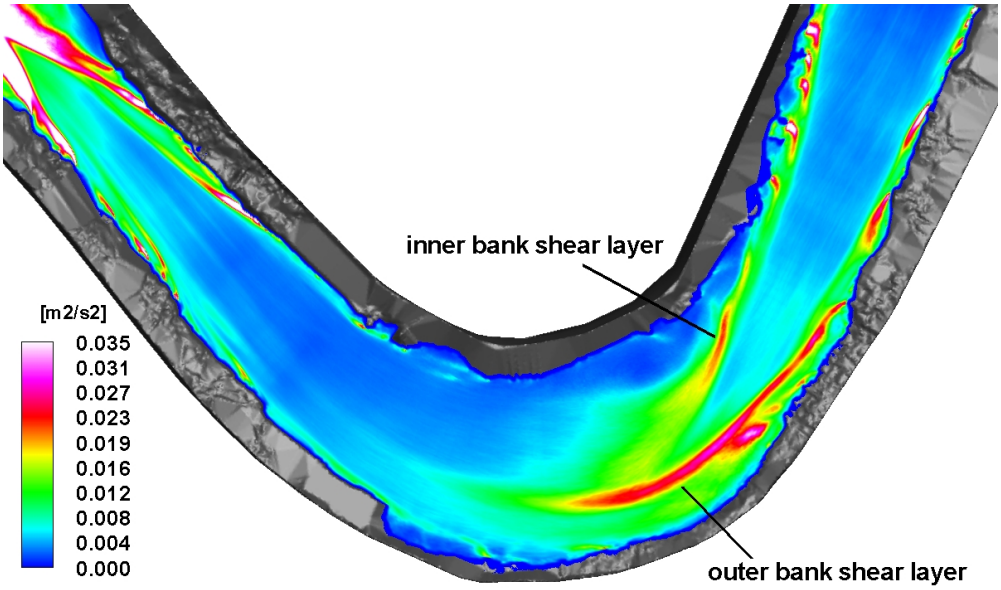

(a) LES model.

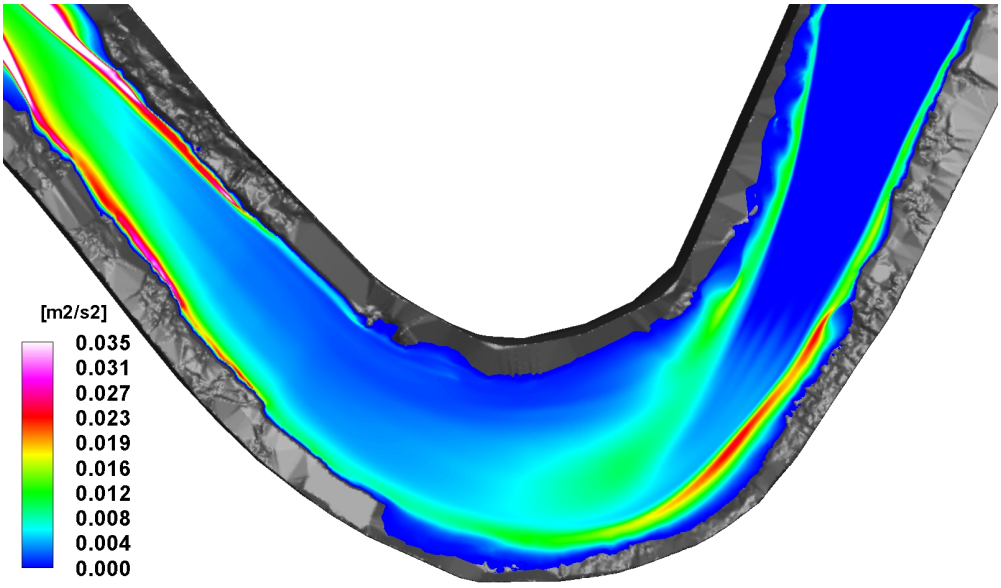

(b) SST RANS model.

Figure 4.18: Computed turbulence kinetic energy contours at the water surface for the bankfull flow (the flow direction is from right to left).

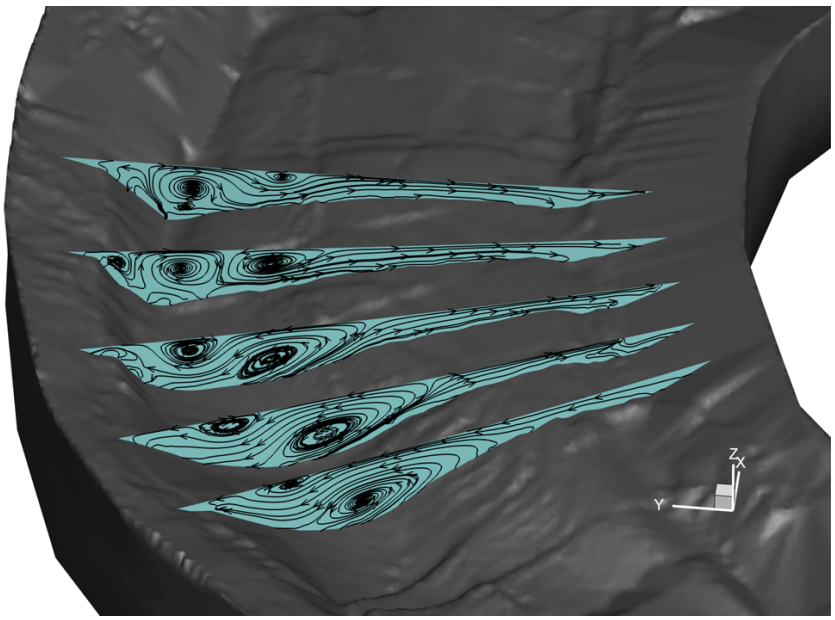

(a) LES model.

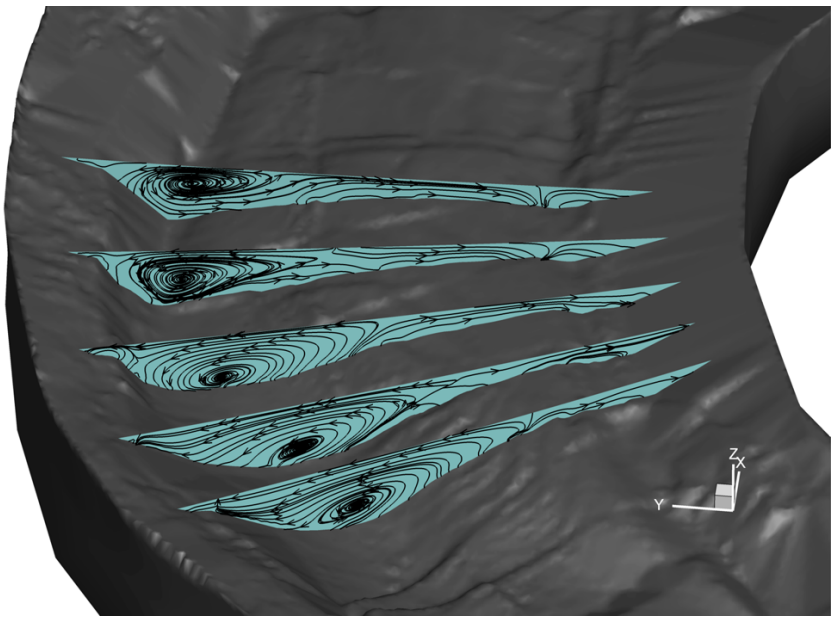

(b) SST RANS model.

Figure 4.19: Computed mean two-dimensional streamlines for the bankfull flow at cross sections near the bend (the flow direction is from bottom to top).

of a large zone of recirculating flow-referred to hereafter as the inner-bank recirculation zone. The RANS results, on the other hand, reveal a rather different structure of the mean flow at the free-surface. Only a very small recirculation region is observed in Figure 4.17(b), along the inner bank, the jet-like structure of the streamwise velocity contours downstream of the riffle is not present (Figure 4.17(b)), the inner bank shear layer in the TKE contours is very weak in the RANS solution, and the outer bank shear layer, while present, it is weaker than in the LES and is located very close to the outer bank (compare Figures 4.18(a) and 4.18(b)). Figure 4.19 shows the two-dimensional streamlines at the cross sections near the bend. As for the base flow case discussed above, the patterns of calculated secondary flow by the LES and RANS models are quite different. While the LES model predicts both the inner and outer bank secondary flow cells, the RANS model predicts only the inner bank cell and yields an overall simpler structure for the secondary flow.

As we also concluded for the base flow case, it follows from Figures 4.12, 4.13, 4.14 and 4.15 that while the RANS model results are in good quantitative agreement with the measured profiles, the global flowfield obtained by the RANS model fails to capture key features of the flow that are obtained by the LES. These include the inner bank reciruclation zone, the jet-like structure of the velocity field in the pool, and the formation of the outer bank cell. It will be shown in Chapter 5 that the flow separation and the outer bank secondary cell are associated with high level of turbulence anisotropy, which cannot be handled by RANS models with isotropic turbulence closure.

Chapter 5

Physics of flow in a meandering stream

In this chapter, flow phenomena and mechanisms in a natural meandering stream with a pool-riffle sequence as they emerge from the present LES and past experimental and computational work are discussed in detail. The bankfull case flowfields are first analyzed and followed by a discussion of the physics of the base flow case and a comparison of the two cases.

5.1 Bankfull flow

In this section we discuss the simulated flow physics by presenting both two-dimensional and three-dimensional visualizations of the calculated flowfields. the instantaneous and time-averaged flowfields of bankfull flow at two two-dimensional planes: 1) the water surface; 2) and a plane located 18 cm below the water surface, i.e. at approximately 75 percent of inlet depth. Figures 5.1, 5.2 and 5.3 show contours of the instantaneous

streamwise velocity component, mean streamwise velocity component and TKE, respectively, at these two planes. we begin the discussion by considering the flow patterns in the riffle followed by flow phenomena in the pool region.

5.1.1 Flow patterns in the riffle

From the instantaneous and mean streamwise velocity contours shown in Figures 5.1 and 5.2, it is evident that the streamwise velocities in the riffle are much higher than those in the pool at all times. This finding is of course consistent with and a direct consequence of the morphology of the riffle-pool sequence in the stream. Namely, due to the much shallower flow depth in the riffle the cross sectional area available to the flow is significantly smaller than in the pool and the streamwise velocity increases to satisfy continuity.

To better illustrate the structure of the near-bed flow in the riffle, we zoom in Figure 5.4 in the second riffle region plotting instantaneous velocity magnitude and TKE contours at the near-bed plane. This figure clearly illustrates the ability of the present method to resolve the dynamics of vortex shedding from discrete roughness elements on the bed. As seen in Figure 5.4(a), for instance, small rocks or varying size and other bed features protrude above the visualization plane and unsteady wake structures are shed from each one of these complex bed features. These wakes interact with each other and the streambed giving rise to a highly-dynamic and very rich flow environment near the bed that is dominated by a multitude of energetic coherent vortices with sizes comparable to the respective size of the bed feature that generated each vortical structure.

The intensity of the flow unsteadiness in this region is evident in Figure 5.4(b), which highlights the ability of the near-bed energetic coherent structures to produce high levels of TKE. It is worth noting that pockets of high TKE occur both upstream and

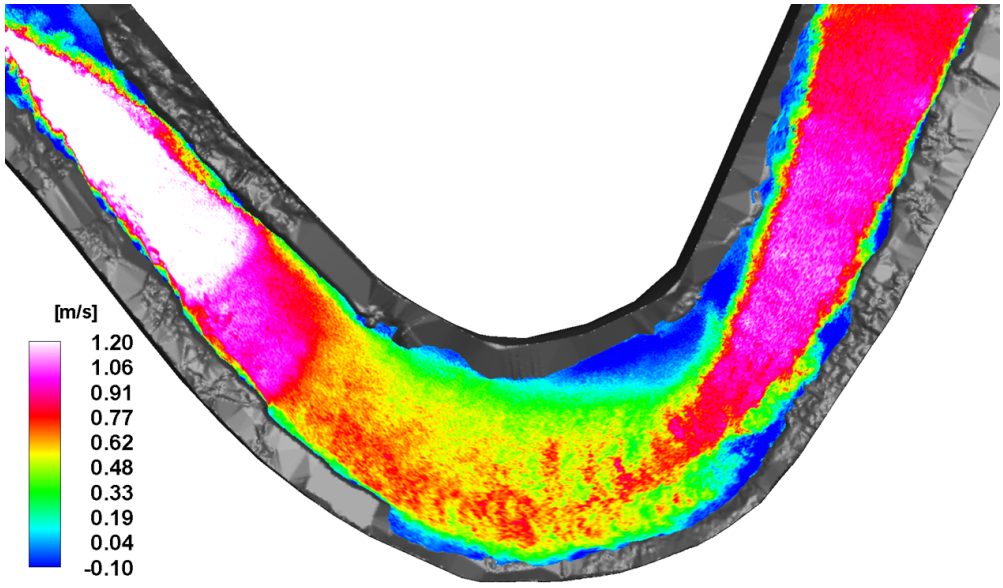

(a) At the water surface.

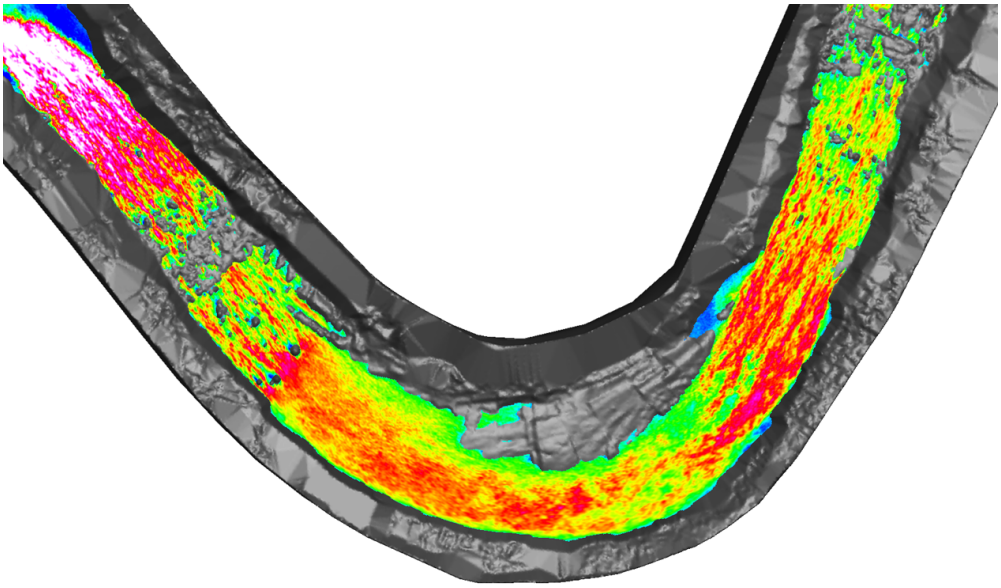

(b) At the plane 18 cm below the water surface.

Figure 5.1: Instantaneous streamwise velocity contours at the water surface (top) and at the plane 18 cm below the water surface (bottom) computed by LES (the flow direction is from right to left).

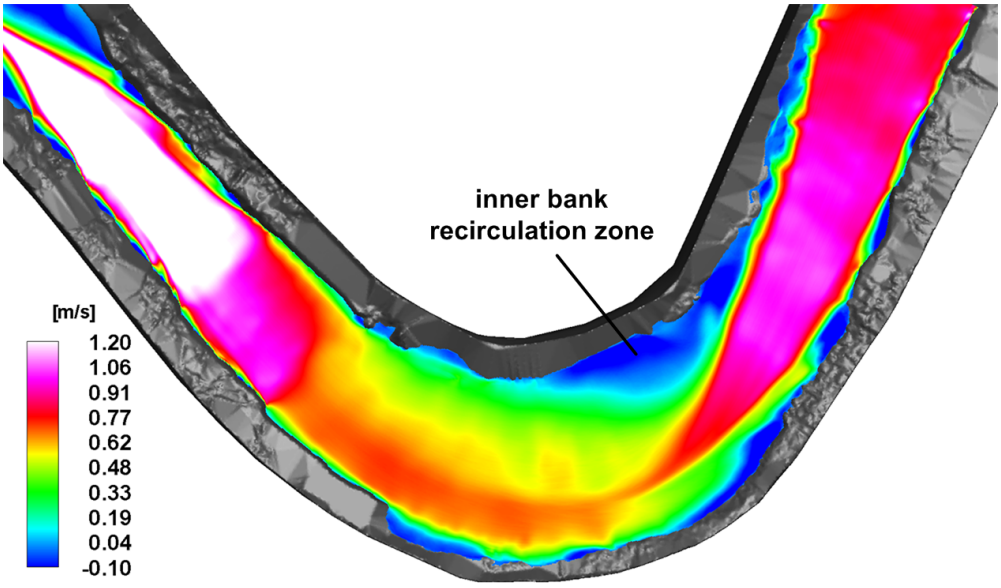

(a) At the water surface.

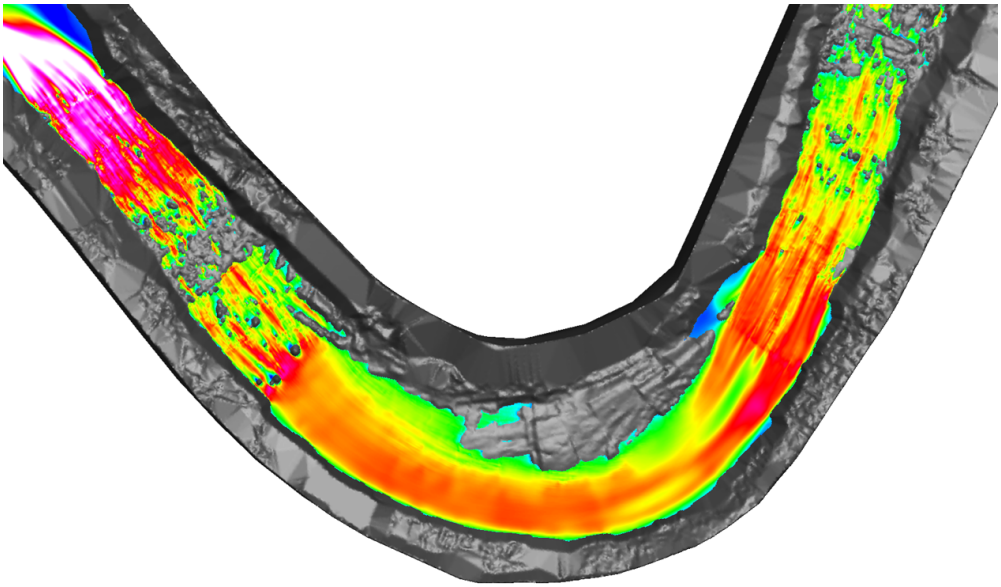

(b) At the plane 18 cm below the water surface.

Figure 5.2: Mean streamwise velocity contours at the water surface (top) and at the plane 18 cm below the water surface (bottom) computed by LES (the flow direction is from right to left).

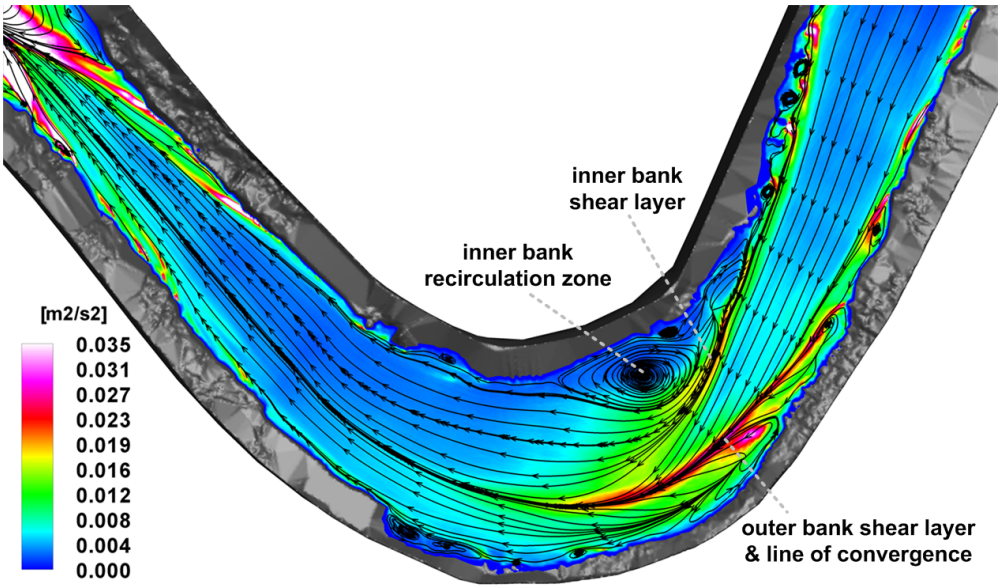

(a) TKE and streamlines at the water surface.

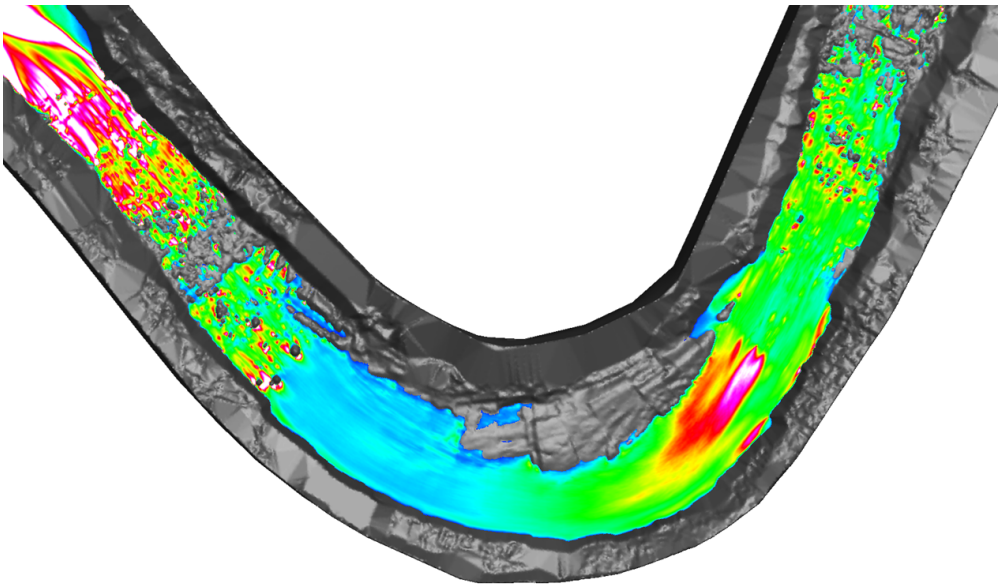

(b) TKE at the plane 18 cm below the water surface.

Figure 5.3: TKE contours at the water surface (top) and at the plane 18 cm below the water surface (bottom) computed by LES (the flow direction is from right to left). Mean streamlines at the water-surface are also shown in the top figure.

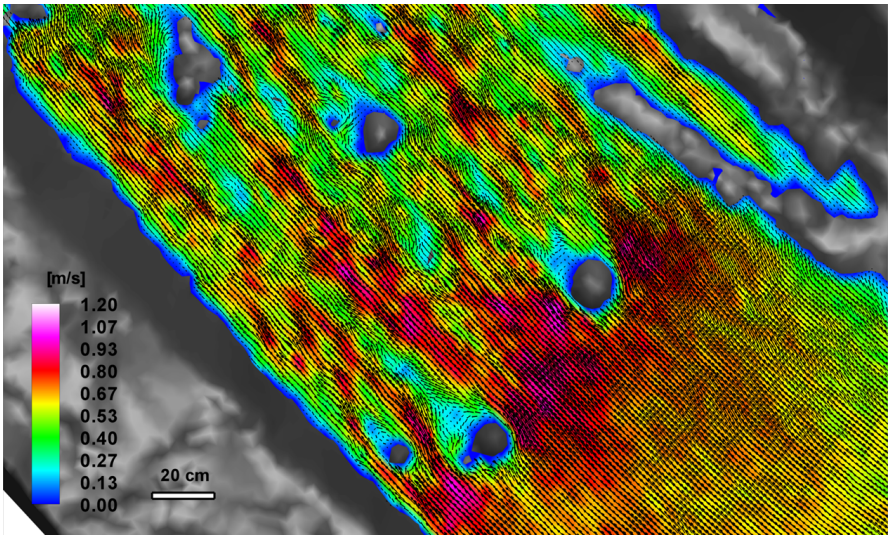

(a) Instantaneous velocity magnitude.

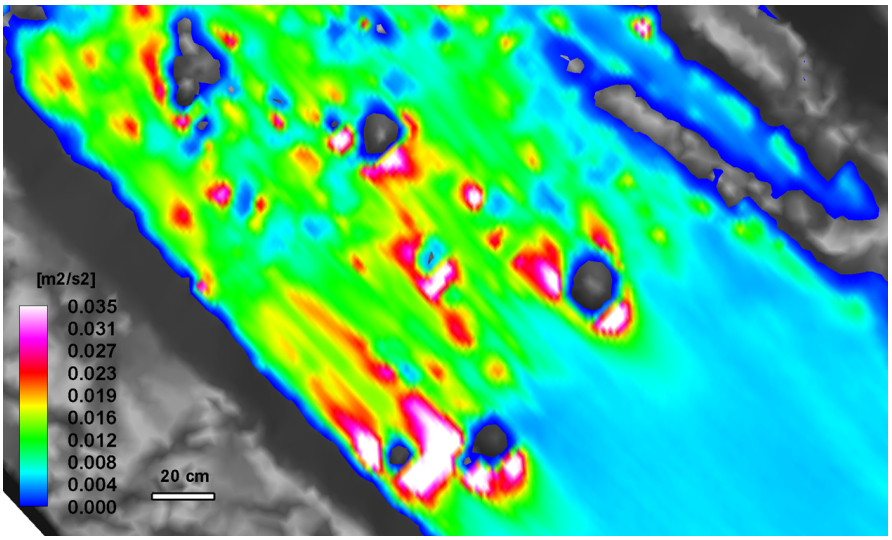

(b) TKE.

Figure 5.4: Computed instantaneous two-dimensional velocity vectors and velocity magnitude contours (top) and TKE (bottom) at the plane 18 cm below the water surface of the second riffle region (the flow direction is from bottom right to top left).

downstream of individual roughness elements, which should be attributed to the complex web of vortical structures induced by the various bed features. For instance, high levels of TKE upstream of roughness elements are likely to be the result of energetic turbulent horseshoe vortices (THSV), which have already been shown capable of producing large levels of turbulence in flows past wall mounted obstacles via low-frequency unsteady fluctuations (Devenport and Simpson, 1990; Paik et al., 2007, 2010). The legs of the THSV are stretched around the various roughness elements interacting with vortical structures in the wake, such arch vortices, tornado and whirlpool vortices, etc. – see the recent work of Paik et al. (2009) who carried out high resolution simulations of the flow past cube-shaped roughness elements. The resulting instantaneous flow environment is very complex, highly dynamic and is characterized by intense turbulent mixing. Another important feature of the near-bed riffle flow that is evident in Figure 5.4(b), is the intense interaction among the wakes shed from each roughness element. As observed in the figure, such interactions raise the TKE levels significantly in between the various bed features causing high overall levels of turbulent mixing throughout the riffle region.

An important consequence of increased turbulent mixing and high Reynolds stresses near the bed is that fine sediments can not be deposited inside the riffle. Only coarser rocks, which can withstand high shear stress, can thus remain in the riffle, thus, pointing to the hydrodynamic reasons for the so-called bed armoring process (Vanoni, 1975). This point will be discussed further in a subsequent section of this chapter where we discuss the wall shear stress patterns at the streambed.

As already mentioned in Section 4.2, the inlet conditions for this simulation were extracted from a separate LES of fully developed turbulent flow in a straight reach with the same cross section as the inlet cross section of the computational domain. Such inflow conditions do not reproduce the first- and second-order statistics of the measured velocity at the inlet correctly and could thus influence the accuracy of the simulated

flowfields in the meander bend. As we showed in Section 4.4, however, the computed mean velocities in the riffles and the pool agree well with the measured data, which already led us to speculate that the flowfield downstream of the riffle is not much affected by upstream errors due to incorrect inlet boundary conditions. The results we have presented in this section clearly show that the complex and very dynamic instantaneous flow environment induced by roughness elements in the riffle renders the flow well mixed and developed within a short distance, thus, diminishing memories of upstream flow conditions. The reason that riffle roughness in this case appears to be very effective in diminishing the impact of the incorrect inflow conditions should be attributed to the shallowness of the flow, which yields typical values of the roughness-height-to-channel-depth ratio to be as high as 50 percent of the flow depth in the riffle. Consequently, the effects of bed roughness are felt throughout the water column causing intense turbulent motions that destroy upstream originating coherent structures and produce an essentially brand new flowfield that is nearly independent of upstream conditions. Obviously, for deeper flows, such as those that can occur during a flood, riffles may not be as effective as in the present case in homogenizing the flow. Therefore, numerical simulation of such cases may well require more careful specification of upstream boundary conditions especially if the flow details within the first meander bend are of interest.

5.1.2 Flow patterns in the pool

We next investigate the simulated flow patterns in the pool. Figures 5.1(a) and 5.2(a) show that as the high-momentum flow from the first riffle enters the pool it narrows forming a strong jet-like flow structure at the water surface. This jet is seen to approach the outer bank of the bend, reaching the apex where the thin high velocity core breaks down and starts diffusing laterally to cover a larger area of the outer bank before it encounters the second riffle. As further seen in Figure 5.2(b), the high velocity jet

appears to become wider below the water surface and is positioned above the thalweg of the bend. The emergence of such high-velocity core near the bed along the outer bank and the thalweg is expected to accelerate streambank and streambed erosion as is known to occur in meander bend flows (Frothingham and Rhoads, 2003).

Another important feature of the surface flow that is evident from Figures 5.1(a) and 5.2(a) is that the narrowing of the high velocity core from the riffle and the formation of the jet-like flow appears, at least at first glance, to be linked to the lateral constriction of the surface flow due to the pockets of negative streamwise velocity that form along both the inner and outer banks of the pool. These are regions of slow recirculating flow with the inner bank recirculation zone being the largest and most prominent feature – this important feature of the flow will be discussed in more detail in a subsequent section of this chapter (see Figures 5.3(a) and 5.10 and related discussion below). Juxtaposing the instantaneous and mean streamwise velocity contour plots in Figures 5.1(a) and 5.2(a) clearly show that the high velocity jet entering the pool, the region of increased streamwise velocity along the outer bank and the pockets of recirculating flow along the inner and outer banks are all rather stable, large-scale features of the flow that are present at all times.

The intensity and spatial extent of flow unsteadiness due to the aforementioned complex flow features in the pool is quantified in Figures 5.3(a) and 5.3(b), which depict contours of TKE at and below the water surface. Figure 5.3(a) also includes mean streamlines at the water surface to facilitate subsequent discussion concerning the links between mean flow patterns and TKE production. There are two distinct thin layers of increased TKE at the water surface that emanate from the inner and outer banks of the bend and mark the outer edges of the previously discussed high velocity jet (see Figure 5.3(a)). We shall refer to these two pockets of increased TKE as the inner and outer bank shear layers, respectively. The inner bank shear layer is seen to

exactly delineate the slow moving flow in the inner bank recirculation zone from the fast traveling outer flow. The reason for the formation of such a shear layer and the associated pocket of increased TKE is easily understood since it is well known that flow separation creates a free shear layer along the boundary of the recirculation zone leaving a clear footprint of high levels of TKE (Le et al., 1997). While the levels of TKE within the inner bank shear layer decay rather quickly at the downstream end of the inner bank recirculation zone, however, the pocket of increased TKE marking the outer bank shear layer intensifies and stretches to reach up to the apex of the bend. This is a rather striking and perplexing feature of the flow, which, unlike the inner bank shear layer, cannot be readily explained by the presence of the small pockets of reversed flow along the outer bank of the bend. In fact, and as clearly revealed by the mean surface streamlines superimposed in Figure 5.3(a), the outer bank shear is seen to coincide exactly with a line of convergence in the mean streamlines along which water surface flow from the outer bank is seen to collide with flow originating near the inner bank. Such line of convergence is the clear mark of three-dimensional separation (Tobak and Peake, 1982) at the water surface in the sense that it must be accompanied by a downward flow from the surface toward the bed. Clearly, therefore, the mechanism that gives rise to the outer bank shear layer is fundamentally different than that generating its inner bank counterpart. As we will subsequently show in Section 5.1.3, this mechanism is linked to the three-dimensional redistribution of streamwise momentum within the pool induced by the complex secondary flow patterns that develop within the bend.

Finally, comparing the TKE contours at and below the water surface in Figures 5.3(a) and 5.3(b), respectively, underscores the three-dimensionality of the flow within the pool. As seen in Figure 5.3(b), for instance, the inner and outer bank shear layers that are present at the water surface are not evident at the 18 cm below the surface plane. Instead a pocket of high TKE is seen to originate at the interface between the shallow

riffle and the deep scour pool. This pocket marks the laterally oriented recirculating eddy created by the sudden, step-like change of bed elevation that generates a shear layer above the deep scour pool.

5.1.3 Secondary flow patterns

To visualize helical secondary flow within the stream we employ the helicity (or helicity density) proposed by Moffatt (1969), which is a scalar quantity defined as follows:

$$H = \overrightarrow{u} \cdot \overrightarrow{\omega}, \tag{5.1}$$

where $\overrightarrow{u}$ and $\overrightarrow{\omega}$ $(= \nabla \times \overrightarrow{u})$ are the velocity and vorticity vectors, respectively. By definition, the helicity H becomes large in regions where the velocity and vorticity vectors are aligned and as such this quantity can be used to identify streamwise vortices in the flow without depending on local cross section and coordinate system definitions. Moreover, if the streamwise velocity is positive the sign of H readily indicates the sense of rotation of the vortical structure. Positive and negative values of helicity imply clockwise and counterclockwise streamwise helical motions, respectively, when in the channel looking downstream.

In Figures 5.5(a) and 5.5(b) we plot side by side contours of the mean helicity and streamwise velocity, respectively, at several cross sections within the stream. These figures reveal a range of complex three-dimensional flow phenomena at various regions within the stream. First, in the straight and shallow riffle zone the helicity contours suggest the presence of multiple streamwise vortical structures along the bed, which distort the isovels both along the bed and near the banks. The presence of streamwise streaks of helical secondary motion in this region is the result of the anisotropy of the Reynolds stresses induced by the combined effects of the channel walls, the water surface and the heterogeneous roughness distribution along the streambed (Naot, 1984;

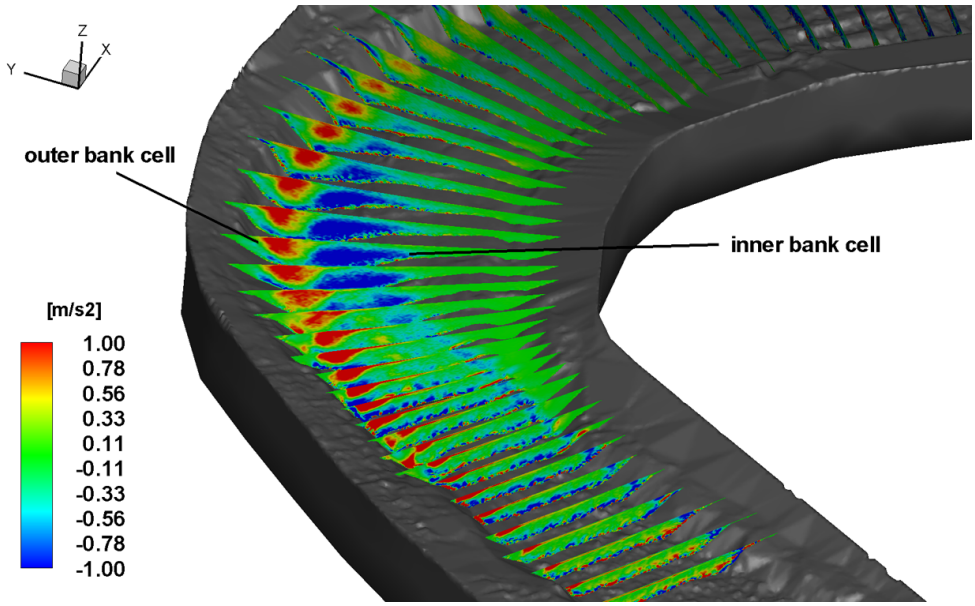

(a) Mean helicity contours

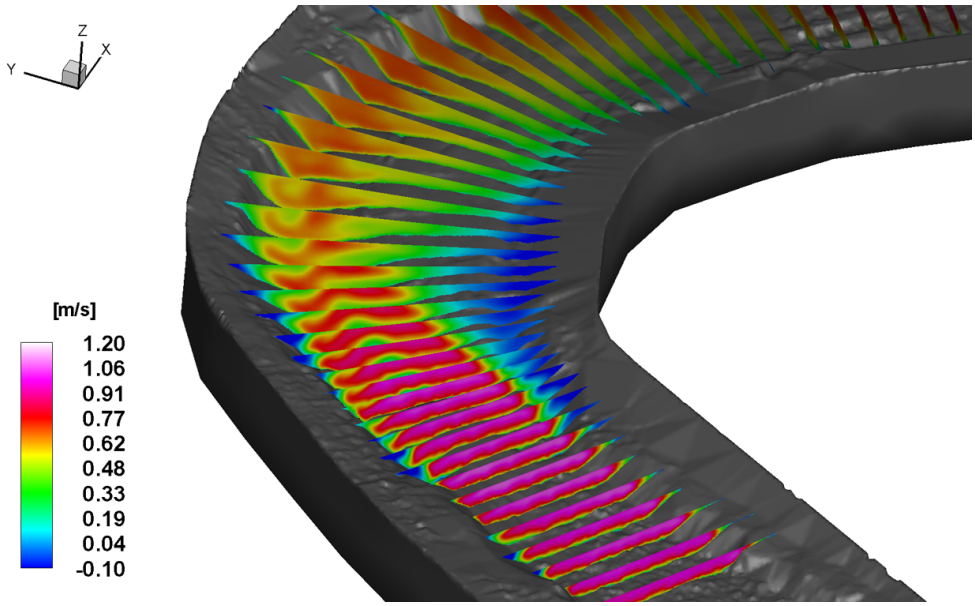

(b) Mean streamwise velocity contours.

Figure 5.5: Three-dimensional visualization of the simulated mean flow patterns by contour plots of mean helicity density (top) and streamwise velocity (bottom) in a series of cross sections through the stream (the flow direction is from bottom to top).

Tominaga et al., 1989).

Downstream of the riffle, the helicity contours reveal that the secondary flow structure transitions from multiple streamwise streaks to a more organized two-cell structure marked by the regions of negative and positive helicity along the inner and outer banks, respectively (see Figure 5.5(a)). These are the well known from previous studies on inner and outer bank cells (Hey and Thorne, 1975; Bathurst et al., 1979; Thorne et al., 1985; Blanckaert and de Vriend, 2004; Balen et al., 2009) – denoted hereafter as IBC and OBC, respectively. The IBC rotates in the counter-clockwise direction (negative helicity), such that near bed flow moves toward the inner bank, and is located closer to the channel bed toward the inner bank. This cell originates via the classical secondary flow mechanism in meander bends and is driven by the imbalance between centrifugal force and transverse pressure gradient (Humphrey et al., 1981; Johannesson and Parker, 1989). Both the intensity and size of the IBC are seen to increase rapidly as the flow encounters the point bar, presumably due to the local increase in streamwise curvature induced by the presence of the point bar, and appear to be maximized at the apex of the bend. Downstream of the apex, however, the IBC starts decaying and essentially disappears well upstream of the second riffle. The OBC, on the other hand, is attached to the water surface and, as seen in Figure 5.5(a), its origin can be traced to a small pocket of positive helicity that appears near the corner junction between the surface and the outer bank somewhere within the downstream end of the first riffle. This cell persists well beyond the apex of the bend even after the IBC has decayed fully. Ultimately, however, both cells are seen to decay well upstream of the second riffle. This finding is consistent with the field observation of Frothingham and Rhoads (2003) who observed that helical motions disintegrate as the flow moves out of the bend, thus, implying that each pool-riffle sequence involves its own physical processes of generation and destruction of helical motions, which are decoupled by those of previous sequences.

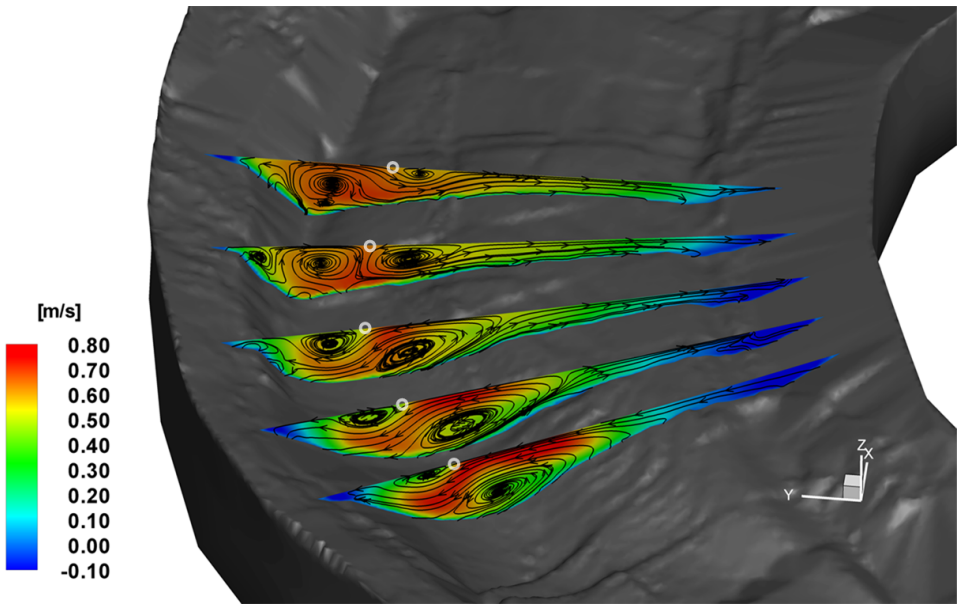

Figure 5.6: Contours of mean streamwise velocity and two-dimensional streamlines at cross sections near the apex (circles denote half saddle points; the flow direction is from bottom to top).

Also, the overall structure and relative location of the OBC in our simulations is in good agreement with previous laboratory and numerical findings with curved open channels of prismatic cross section (Blanckaert and de Vriend, 2004; Balen et al., 2009; Stoesser et al., 2010) as well as consistent with previous field observation (Hey and Thorne, 1975; Bathurst et al., 1979; Thorne et al., 1985).

The existence of the two secondary motion cells has a profound effect on the redistribution of mean streamwise momentum within the bend as seen in Figure 5.5(b). The fairly uniform in the lateral direction high mean streamwise momentum core that occupies almost the entire cross section at the end of the riffle gets distorted near the outer bank as it enters the bend, plunging sharply toward the streambed and giving rise to a region of reduced streamwise velocity near the water surface along the outer bank that extends up to the apex of the bend. To further elucidate the highly three-dimensional

structure of the flow in this region, we plot in Figure 5.6 contours of the streamwise velocity superimposed with two-dimensional streamlines at few cross sections near the apex. In addition to the clear depiction of the manner via which the IBC and OBC redistribute mean streamwise momentum within the cross section, this figure also clarifies the downstream evolution and interaction of the two cells. The size of the IBC is much larger than that of the OBC at the first cross section in Figure 5.6. At the second and third cross sections, the IBC still dominates the cross sectional flowfield but the OBC starts growing in size. At the fourth cross section, the OBC grows further and its size is now comparable to that of the IBC while an additional very small cell rotating in the counter-clockwise direction is observed near the corner of the outer bank. At the last cross section in Figure 5.6, which is located near the apex of the bend, the IBC has nearly disappeared while the OBC is still present. From the well mixed streamwise velocity contours at this last section, however, it is evident that the intensity of both cells has diminished a great deal as they are no longer capable of redistributing mean streamwise momentum.

Figure 5.6 also reveals that a key feature of the surface flow near the outer bank in the vicinity of the apex of the bend is the presence of a half saddle point in the secondary flow streamlines marked by a circle in the figure. Using terminology from topological fluid mechanics (Tobak and Peake, 1982), the stable manifolds of this saddle are defined by the inward directed OBC flow and the outward directed IBC flow along the water surface. Its unstable manifold, on the other hand, is defined by the downward directed common flow between the two secondary flow cells that transports high momentum flow from the water surface toward the streambed. Revisiting now the previously discussed Figure 5.3(a), it is evident that the locus of the half saddle points at the cross sectional streamlines plots is the outer bank line of convergence in the water surface streamlines, which also coincides with the high TKE values defining the outer bank shear layer. As we

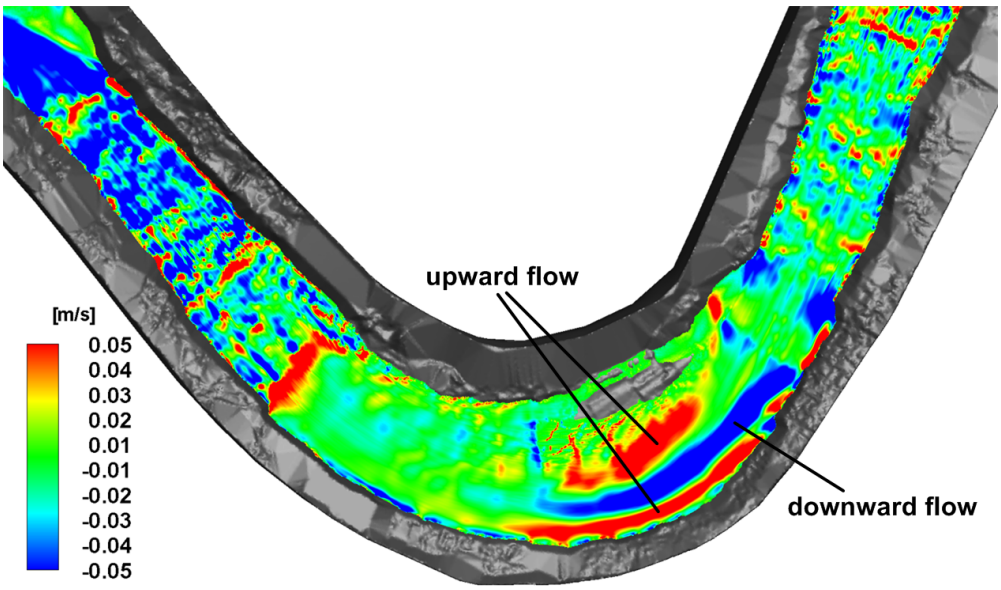

Figure 5.7: Contours of mean vertical velocity at the plane 12 cm below the water surface (the flow direction is from right to left).

already mentioned above, this line of convergence is the hallmark of three-dimensional flow separation at the water surface. The cross sectional streamline plots shown in Figure 5.6 clearly show that this three-dimensional separation is the result of the collision of the IBC and OBC flows along the line of convergence at the water-surface and the so induced downward common flow along the unstable manifold of the half saddle point at each cross section.

To highlight the structure and intensity of the vertical flow within the bend, we plot in Figure 5.7 contours of the mean vertical velocity at a plane 12 cm below the water surface. Near the point bar the flow moves upward both at the inner and outer banks, and it converges near the water surface by creating downward flow to the channel bed. As discussed above, converging flow at the water surface is the result of the two colliding counter-rotating cells that leads to the formation of the half saddle point at the surface. As seen in Figure 5.7, the downward flow motion is most intense above

the thalweg near the point bar, which suggests that the converging flow at the surface and the so induced strong downward flow are related to the deepening of the channel in support of the field observations of Hey and Thorne (1975) and Thompson (1986). As already discussed in the Introduction, Hey and Thorne (1975) observed two secondary cells in natural rivers exhibiting surface flow convergence, which gives rise to channel deepening, and Thompson (1986) investigated flow in a meandering gravel-bed stream and observed a zone of upwelling adjacent to the outer bank of the stream and inward flow towards a zone of convergence over the deepest part of the pool. The upward flow motion is intense near the point bar, which points to the conclusion that the IBC, which directs near-bed flow to the inner bank, contributes to the formation of the point bar.

Juxtaposing now Figures 5.5, 5.6 and 5.3(a) with Figure 5.3(a), a clear explanation about the mechanism that gives rise to the previously discussed outer bank shear layer emerges. The collision of the OBC and IBC flows along the water surface at the line of convergence marked in Figure 5.3(a) creates a downward directed flow toward the deep part of the pool that transports high momentum fluid from the surface toward the bed. As a result, a low mean streamwise momentum region emerges at the surface near the outer bank and a shear-layer is formed along the line where the two cells collide at the water surface. The mean velocity gradients across the shear layer increase the production of turbulence and give rise to the elongated pocket of high TKE observed in Figure 5.3(a) along the outer bank.

To elucidate the mechanisms via which turbulence is produced within the outer bank shear layer (see Figure 5.3(a) and related discussion above) we plot in Figure 5.8 contours of the TKE and the three velocity variances at the cross section located at the apex of the bend. At the apex, the x, y and z directions are the streamwise, transverse and vertical directions, respectively. It is evident from Figure 5.8, that the structure of turbulence in the vicinity of the half saddle point in the cross sectional

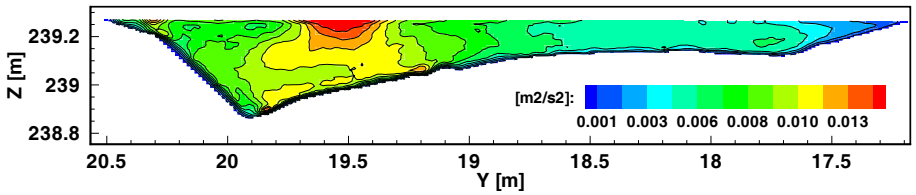

(a) TKE.

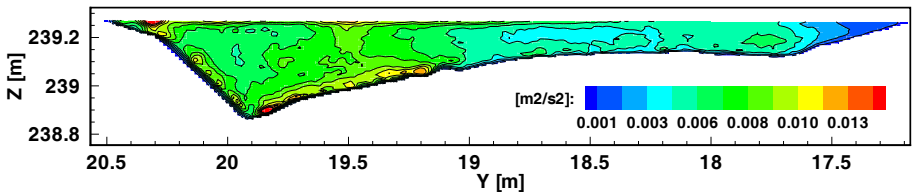

(b) $\overline{u'u'}$.

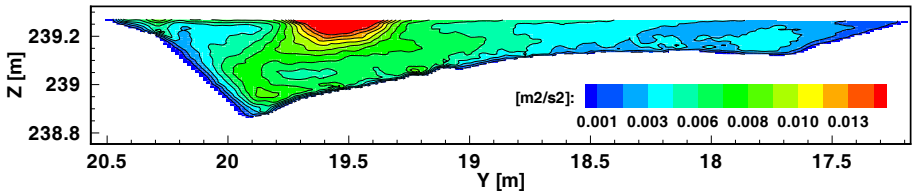

(c) $\overline{v'v'}$.

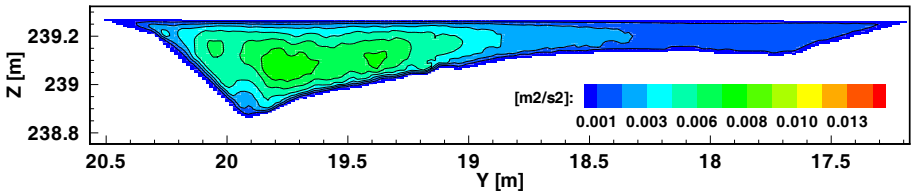

(d) $\overline{w'w'}$.

Figure 5.8: Computed TKE and velocity variance contours at the cross section located at the apex of the bend.

streamlines is highly anisotropic. At this point, the lateral velocity variance $\overline{v'v'}$ is much larger than $\overline{u'u'}$ and $\overline{w'w'}$, which shows that essentially all TKE produced in this region is the result of lateral velocity fluctuations at the point where the OBC and IBC flows collide at the water surface. The vertical velocity variance ($\overline{w'w'}$) approaches zero as the water surface is approached because the vertical velocity fluctuations are suppressed by the presence of the water surface. The nearly zero vertical velocity variance ($\overline{w'w'}$) and the high transverse velocity variance ($\overline{v'v'}$) around the half saddle point at the water surface, thus, increase the anisotropy of the transverse and vertical Reynolds stresses ($\overline{v'v'} - \overline{w'w'}$). Since the gradients of this anisotropy term appear in the mean streamwise vorticity transport equation and have been shown to contribute to the production of stress-driven secondary flows in straight channels (Perkins, 1970), the results presented in Figure 5.8 support previous findings that turbulence anisotropy is a major contributing factor in the generation of the OBC in meander bends (Blanckaert and de Vriend, 2004; Balen et al., 2009).

To further investigate the structure of turbulence anisotropy throughout the entire channel, we employ the second invariant of the anisotropy tensor (Lumley, 1978) defined as follows:

$$II = -\frac{1}{2} b_{ij} b_{ji}, \tag{5.2}$$

with

$$b_{ij} = \frac{\overline{u_i' u_j'}}{2k} - \frac{1}{3}\delta_{ij}, \tag{5.3}$$

where and u_i' denotes velocity fluctuations in the i^{th} direction, k is the TKE, δ_{ij} is the Kronecker delta, and the overbar denotes the temporal (or Reynolds) averaging. Note that II is a scalar quantity that is invariant to coordinate system transformation and as such it is not sensitive to the specific coordinate system selected to express the

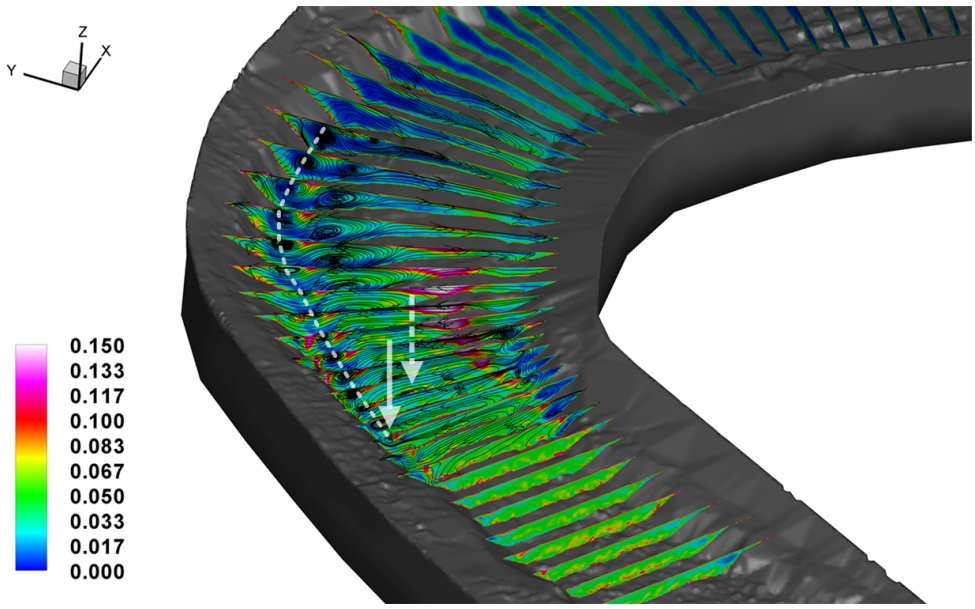

Figure 5.9: Contours of the second invariant of the turbulence anisotropy tensor and secondary flow streamlines in a series of cross sections through the stream. The solid arrow points the approximate origin of the outer bank cell while the dashed arrow points the approximate origin of the inner bank cell. Dashed white line traces the approximate streamwise extent of the outer bank cell. (the flow direction is from bottom to top).

velocity field and calculate the components of the Reynolds-stress tensor. In addition, this quantity is identically zero for isotropic turbulence and becomes large in regions where anisotropy becomes important.

Figure 5.9 shows contours of $-II$ superimposed with secondary flow streamlines at several cross sections through the channel. It is seen that the OBC originates near the entrance of the meander bend in a region at the water surface close to the outer bank where turbulence anisotropy is large. The sense of rotation of the OBC, however, is such that the near bed flow is directed toward the outer bank. As such, the centrifugal force, which is also directed along the same direction, acts to augment the OBC and sustain it further downstream even in regions where turbulence anisotropy has diminished– see cross sections downstream of the bend apex in Figure 5.9. When both turbulence

anisotropy and curvature effects diminish, however, as the end of the meander bend is approached, the OBC is seen in Figure 5.9 to decay as well and disappear completely upstream of the second riffle. Therefore, the picture that emerges from our simulations regarding the generation of the OBC in natural meander bends is consistent with that derived from previous experimental and computational studies with open channels of prismatic cross section (Blanckaert and de Vriend, 2004; Balen et al., 2009). Namely, both turbulence anisotropy effects and the curvature-induced centrifugal force contribute to generate and sustain the OBC in meander bends.

Figure 5.9 further provides some additional insights into the structure of turbulence in natural meandering streams. First, note that turbulence anisotropy is large overall across the entire cross section throughout the riffle region with pockets of very high anisotropy levels observed near the bed around individual roughness elements. This finding supports our previous discussion that the streamwise vortical structures observed in the helicity plot in Figure 5.5(a) within the riffles mark secondary flow cells driven by roughness-induced anisotropy. Perhaps the most striking new finding that emerges from Figure 5.9, however, is that the largest pocket of anisotropy within the stream is observed along the upstream edge of the point bar. This finding is consistent with the fact that the three-dimensional geometry of the point bar increases the complexity of the mean flow causing extra rates of strain, i.e. spatial gradients of all three velocity components along all three spatial directions, that act to enhance the anisotropy of turbulence. Overall, the results presented in Figure 5.9 show that turbulence anisotropy is important in several regions within natural meandering channels and point to the conclusion that accurate simulation of such flows requires the use of models that can accurately resolve the anisotropy of turbulence.

5.1.4 Recirculation zones

The instantaneous and mean velocity contours at the water surface presented in Figures 5.1(a), 5.2(a) and streamlines shown in Figure 5.3(a) above, revealed the presence of multiple recirculation zones along both the inner and outer banks. To further elucidate the structure of these flow features we plot in Figure 5.10 three-dimensional streamlines of the mean flow in the vicinity of the point bar superimposed with contour plots of bed elevation. The inner bank recirculation zone is clearly the dominant recirculating flow region in the stream. As seen in Figure 5.10, the flow in this region consists of a large primary eddy and two smaller, secondary, eddies that collectively span almost the entire point bar. A rather striking feature of the flow that emerges from this figure is that the center of the primary recirculation eddy, where the flow is stagnant in the mean, is located directly above the highest point of the point bar. This finding points to the conclusion that the inner bank flow recirculation plays an important role in the formation of the point bar. It provides a region of reduced velocities (see Figure 5.2(a)) and low turbulence mixing (see Figure 5.3(a) showing very low TKE levels within the inner bank recirculation region) within which fine sediments that are transported there by the IBC flow as bedload could be trapped and deposit. This assertion is consistent with and further supports the work of Schmidt (1990) who observed the formation of sand bars beneath recirculation zones at the water surface.

In addition to the inner bank recirculation zone, Figure 5.10 also reveals the presence of smaller recirculating flow regions along the outer bank. These appear to be linked to local features in the topography of the outer bank that give rise to pockets of adverse streamwise pressure gradients causing the observed flow separation patterns. As previously discussed, however, these are relatively small scale features of the flow linked to site-specific, local topographic irregularities that do not appear to have a major impact on the overall large-scale flow patterns within the stream. Nevertheless, their presence

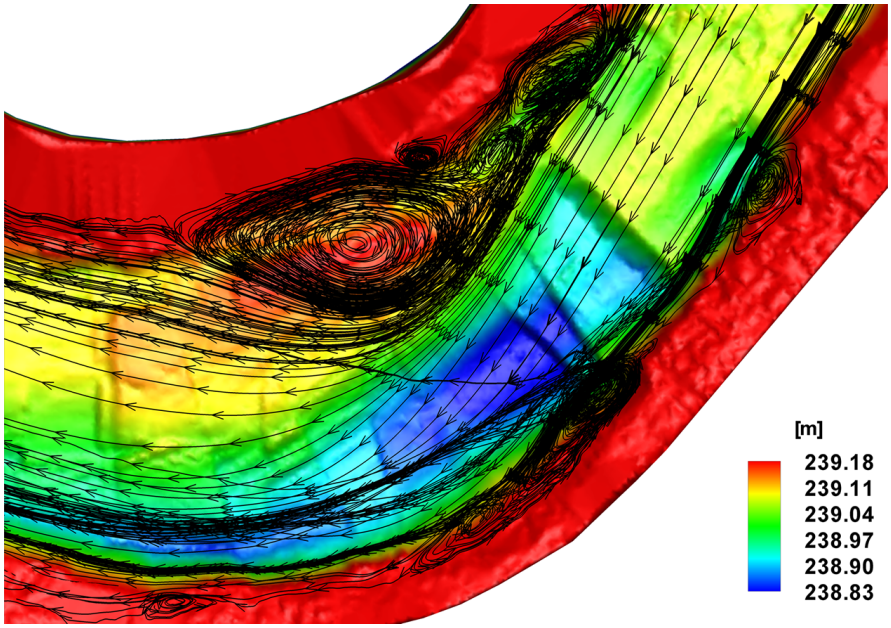

Figure 5.10: Mean three-dimensional streamlines near the apex of the meander bend superimposed with bed elevation contours (the flow direction is from right to left).

is important as such topographic variability is certainty present in natural streams and could further enhance the complexity of the flow relative to that obtained in simpler laboratory-scale flumes.

5.1.5 Bed shear stress

Bed shear stress is an important parameter in open-channel flows as it is associated with the potential of streambed erosion and scour and is also used as input to morphodynamic models. It is thus appropriate to conclude our discussion of the flow physics by considering how the previously discussed complex, three-dimensional hydrodynamic environment in the stream impacts the distribution of the bed shear stress. Figure 5.11 shows the calculated mean shear stress field along the streambed.

The shear stress distribution in the two riffles is characterized by larger overall magnitudes than in the pool, a trend consistent with the higher overall velocities found

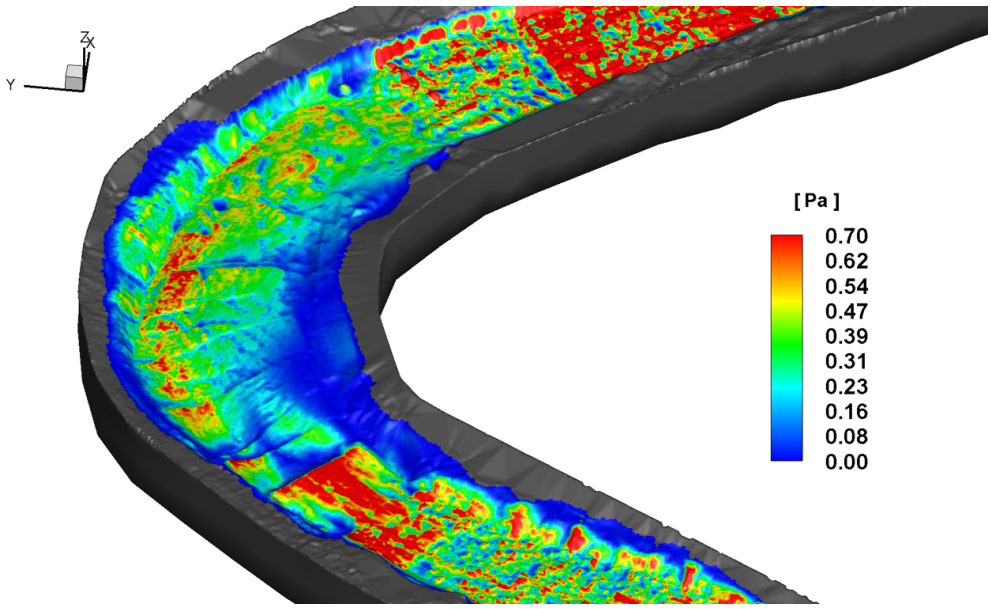

Figure 5.11: Contours of the mean bed shear stress (the flow direction is from bottom to top).

in the riffles across the entire water column. It is also evident from Figure 5.11 that the distribution of the shear stress within the riffle is highly heterogeneous. Multiple small pockets of increased shear stress levels are found that correlate well with the locations of the protruding roughness elements on the bed. The increase of bed shear stress at these locations should be attributed to the local acceleration of the flow induced by the presence of the roughness elements. Figure 5.11 further reveals several regions of very low shear stress values throughout the riffle. These regions generally occur in the wake of individual roughness elements, which would tend to be occupied by slower recirculating flow. Overall, however, the regions of very low shear stress in the riffle are considerably fewer than the pockets of very high shear values.

Figure 5.11 also shows that low bed shear stress values are observed within the scour pool formed at the riffle-pool transition. The shear stress in this region exhibits a sharp discontinuity from the very high values upstream of the scour pool to nearly zero values

in the pool. Such steep gradients can be easily understood in terms of the local bed bathymetry in this region that exhibits a steep, backward-facing-step like transition in bed elevation and induces a laterally-oriented recirculation eddy with very low velocities in the scour pool.

Low shear stress values are also found along the inner bank all along the point bar due to the influence of the inner bank recirculation zone that lowers flow velocities. Along the outer bank, on the other hand, the shear stress magnitude is significantly higher with very high values observed along the thalweg of the pool. The mechanism that causes such high shear stress values in the pool has already been discussed above and is linked to the transport of high momentum fluid from the water surface toward the bed by the strong downward flow induced by the combined action of the IBC and OBC in this region. Therefore, Figure 5.11 in conjunction with our previous discussion in Section 5.1.3 elucidate the impact that the complex and highly three-dimensional interaction between the secondary flow with the streamwise flow through the bend has on the distribution of the bed shear stress. Such interaction is essentially responsible for increasing the shear stress along the thalweg of the channel, enhancing erosion, and promoting channel deepening.

5.2 Base flow vs. bankfull flow

In this section we juxtapose the calculated flowfields for the base and bankfull flow cases in order to elucidate the impact of the increasing flowrate through the stream on the underlying flow phenomena and mechanisms. Figures 5.12 and 5.13 compare contours of mean streamwise velocity and TKE computed by LES for base and bankfull flows, respectively. A large inner bank recirculation zone is found in the bankfull flow (see Figure 5.12(b)), which is not observed in the base flow (see Figure 5.12(a)). This is probably due to the fact that, because of the shallower flow depth, the expansion of the flow area and the so-induced adverse streamwise pressure gradient are not large enough in the base flow to induce flow separation along the inner bank. The jet-like flow structure found in the bankfull flow (see Figure 5.12(b)), which, as we discussed above, is caused by the inner and outer bank shear layers, is not clearly observed in the base flow results (see Figure 5.12(a)). The TKE contours for the base flow (see Figure 5.13(a)) do not show the presence of intense inner and outer bank shear layers with high levels of TKE and it explains the absence of the jet-like flow for this case. Instead, a thin layer of high streamwise velocity is observed along the inner bank in the base flow (see Figure 5.12(a)). This thin layer starts from the boundary of the small recirculation zone attached to the inner bank near the interface between the first riffle and the pool (see Figure 5.14(a)) and moves along the inner bank of the bend. Figure 5.13(a) shows that this thin layer separates the zones with low and high levels of TKE at the inner bank outer banks, respectively, and it suggests that the thin layer of the high streamwise velocity along the inner bank is formed by a weak free shear layer generated by the flow separation at inner bank.

Another important difference between the two cases follows from the TKE contours shown in Figure 5.13 in the riffle region. For the base flow case multiple pockets of large TKE values appear on the water surface, which are essentially the surface footprints of

individual roughness elements in the riffle. No such structure is observed, however, in the TKE contours for the bankfull flow case, which appear to be relatively homogeneous within the central part of the riffle. This trend should be attributed to the differences in the flow depth between the base and bankfull cases. For the former case the riffle flow is sufficiently shallow for the roughness elements to penetrate well into the outer layer of the flow ($k > 0.2h$), where k and h denote the roughness height and flow depth, respectively, thus, leaving clear footprints in the TKE field on the surface. For the bankfull case, on the other hand, the roughness elements do not penetrate as deep in the outer layer and the mean flow above them becomes more mixed and spatially homogeneous. Typical values of the roughness height-to-channel-depth ratio for base and bankfull flows are as high as 50 percent of the flow depth in the riffle.

Figure 5.14 compares the two-dimensional streamlines at the water surface for the base and bankfull flow cases. The streamlines for the bankfull flow (see Figure 5.14(b)) reveal a large recirculation zone along the inner bank and show the distinct line of convergence near the outer bank – see the previous section for the mechanisms giving rise to these features. The streamlines of the base flow (see Figure 5.14(a)), on the other hand, show several smaller recirculation zones along the inner banks, which is consistent with the previously discussed absence of a large recirculation region for this case along the inner bank. In fact for the base flow case, the streamlines in Figure 5.14(a) suggest that the recirculation zones observed along the inner bank are primarily the result of local topographic features of the inner bank bathymetry (similar to those observed along the outer bank for both cases) rather than a large-scale feature of the flow as for the bankfull flow case. A line of convergence is also present in the base flow case (see Figure 5.14(a)) but compared to the bankfull flow case this line remains closely attached to the outer bank. Figure 5.15 compares the helicity contours at the water surface for the base and bank flow cases. In base flow, a thin layer with positive helicity (see Figure 5.15(a))

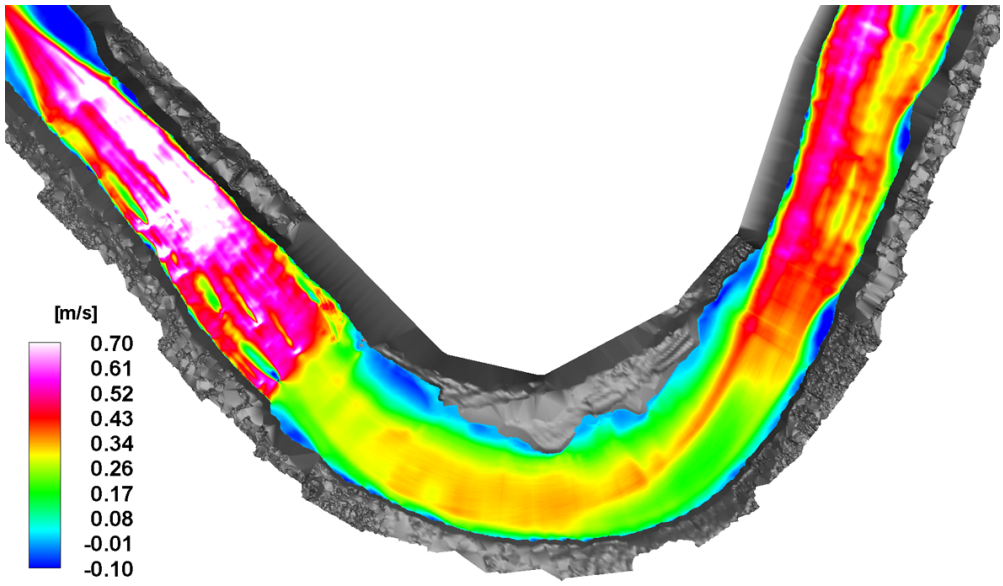

(a) Base flow.

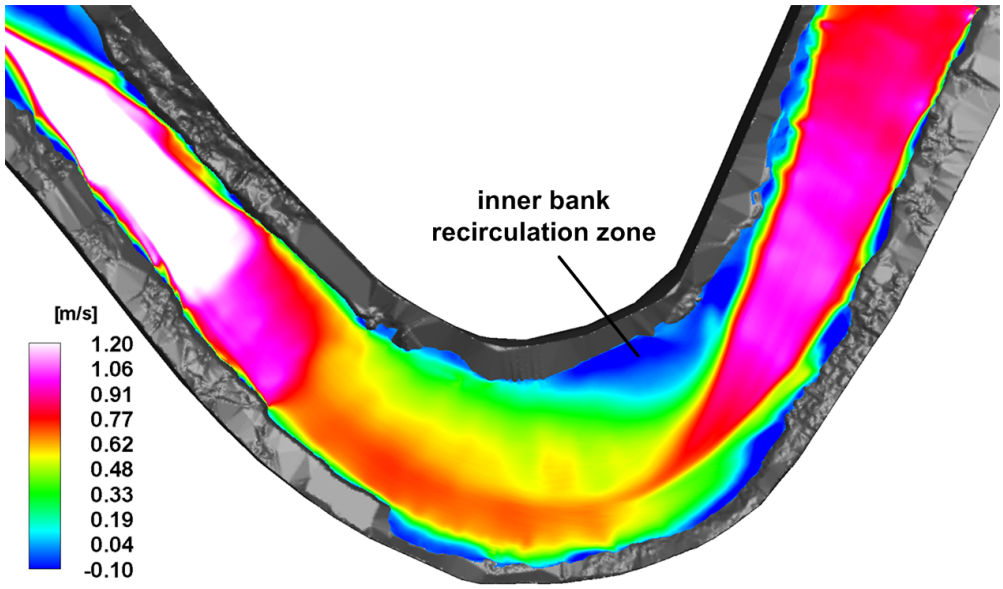

(b) Bankfull flow.

Figure 5.12: Comparison of mean streamwise velocity contours at the water surface computed by LES for base (top) and bankfull (bottom) flows (the flow direction is from right to left).

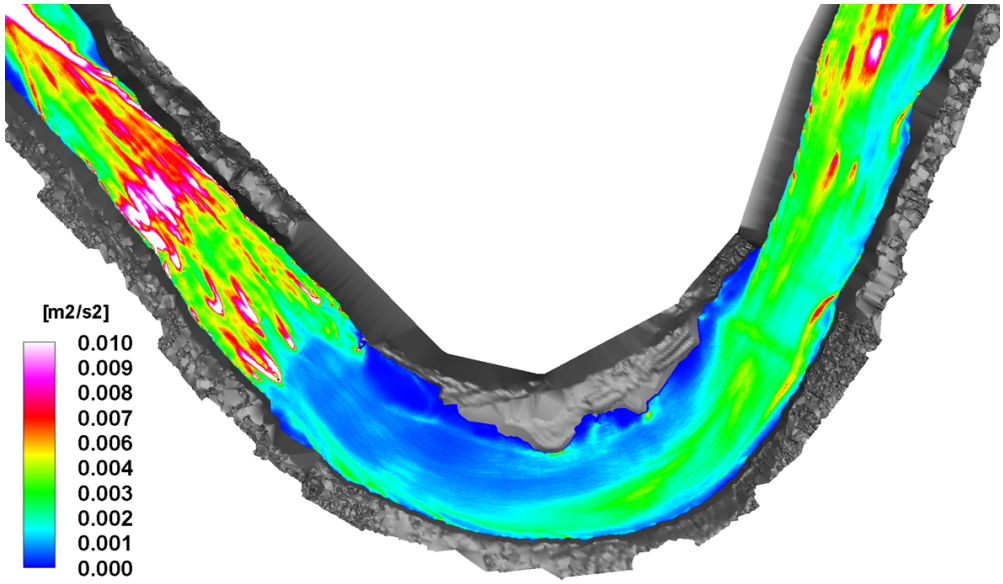

(a) Base flow.

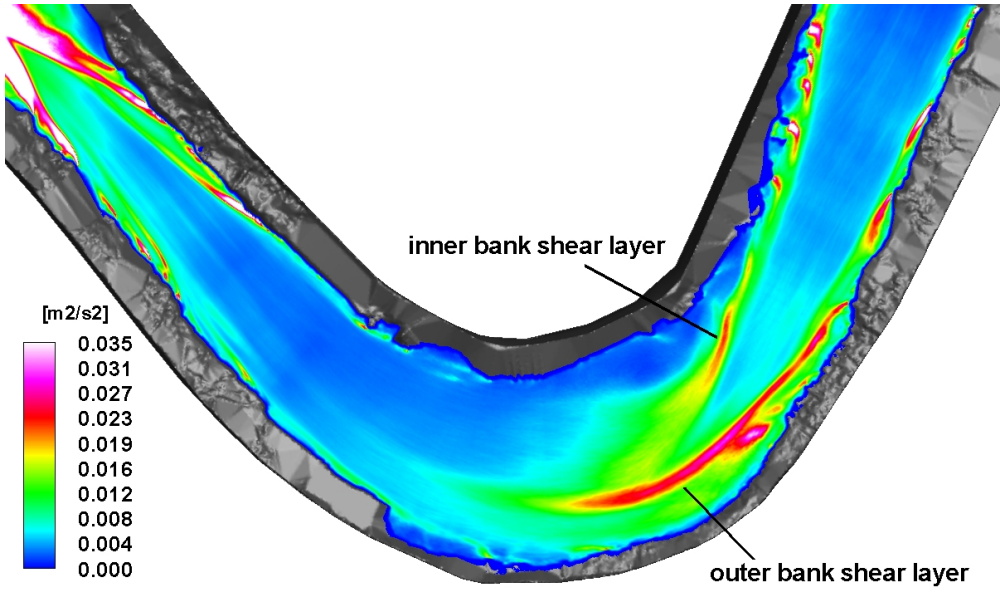

(b) Bankfull flow.

Figure 5.13: Comparison of TKE contours at the water surface computed by LES for base (top) and bankfull (bottom) flows (the flow direction is from right to left).

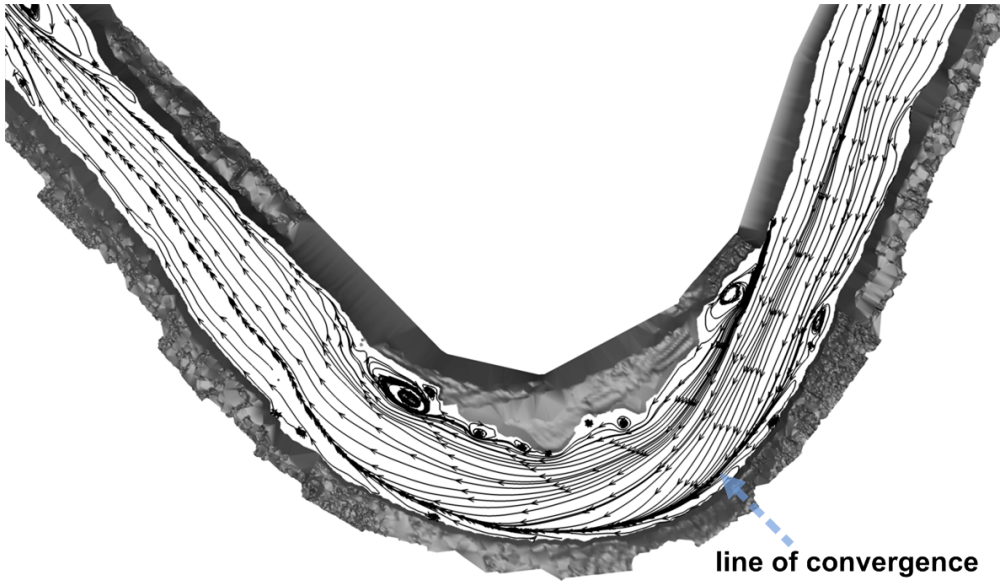

(a) Base flow.

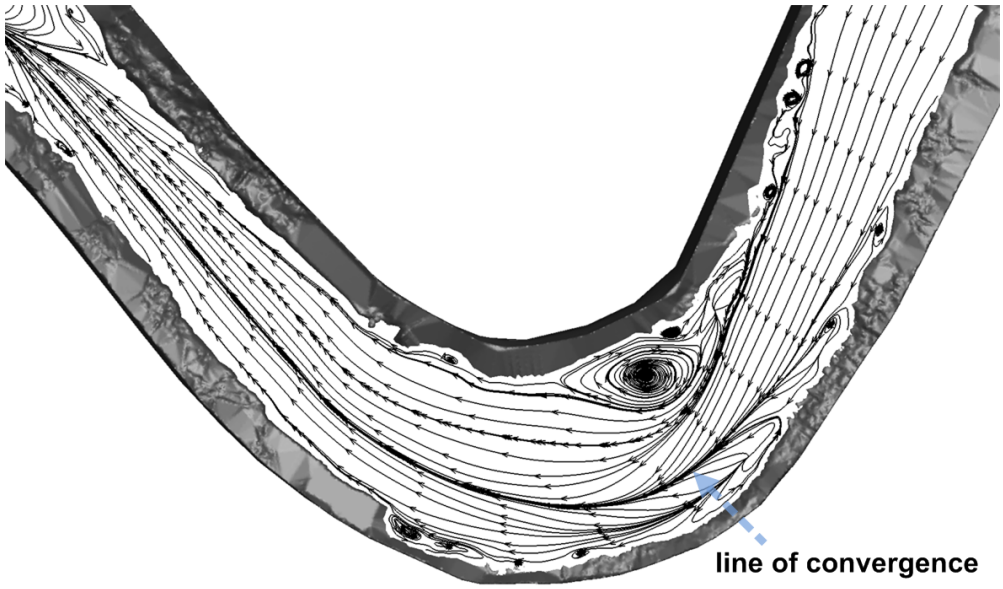

(b) Bankfull flow.

Figure 5.14: Comparison of two-dimensional streamlines at the water surface computed by LES for base (top) and bankfull (bottom) flows (the flow direction is from right to left).

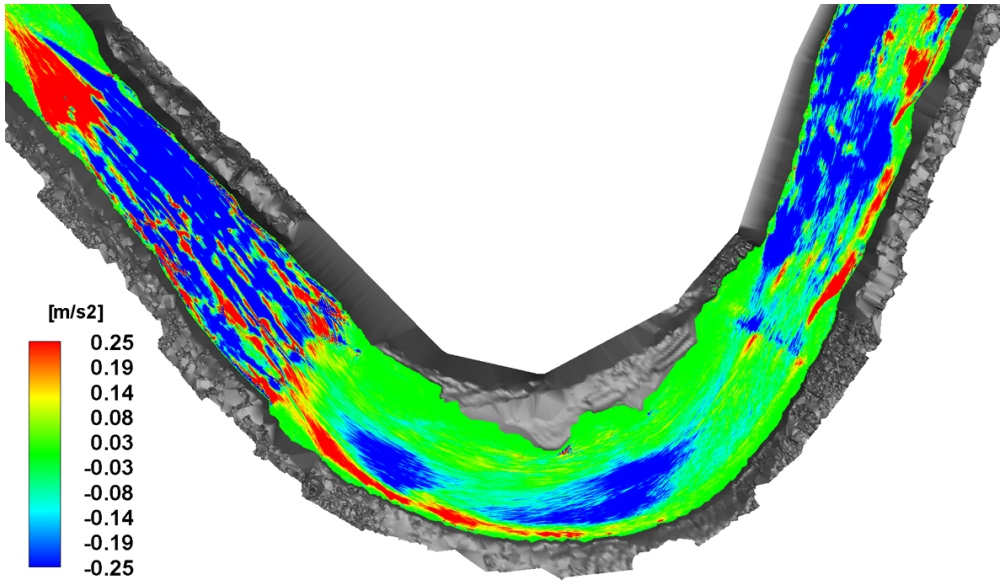

(a) Base flow.

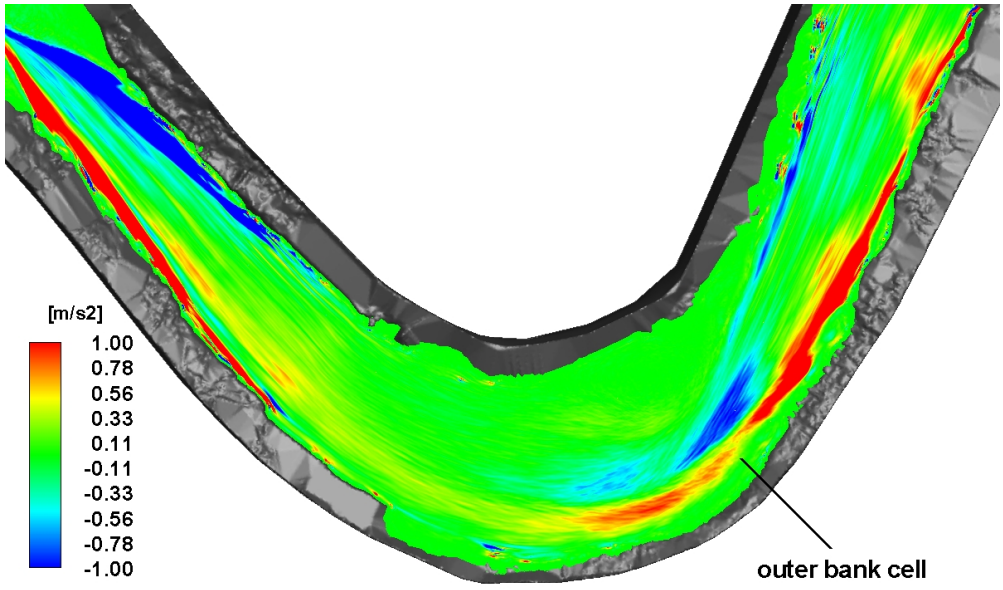

(b) Bankfull flow.

Figure 5.15: Comparison of helicity contours at the water surface computed by LES for base (top) and bankfull (bottom) flows (the flow direction is from right to left).

is positioned along the line of convergence (see Figure 5.14(a)) which is closely attached to the outer bank. This figure shows that the outer bank cell also exists in the base flow but its size is much smaller than that of the bankfull flow. Given the discussion in the previous section concerning the mechanism that generates this line of convergence in the bankfull case and the secondary flow patterns for the base flow case shown in Figure 4.8, it is evident that this feature of the base flow case should be attributed to the shallow flow depth for the base flow case which limits the growth of the outer bank cell.

Chapter 6

Modeling of flow with a rock vane instream structure

Instream structures for stream restoration have been studied and assessed (Gray and Sotir, 1996; Maryland Department of the Environment, 2000; Rosgen, 2001; Johnson et al., 2001; Harman et al., 2001; Johnson et al., 2002a,b) over ten years. However, few of the previous studies focused on detailed flow physics around instream structures. Most of previous works studied the performance of the instream structures in the field or laboratory by investigating deposition and scour patterns in the vicinity of structures or failure rates of the structures. However, in-depth understanding of flow physics occurring in natural streams around instream structures is essential to enable science-based approaches to stream restoration.

To study flow physics around instream structures, a rock vane instream structure was installed along the outer bank of the bend and near the apex of the OSL (see Figure 6.1) in the bankfull flow condition. The installed rock vane was composed of several rocks and the length of the rock vane structure was approximately 2 m. Rock vanes are known to direct oncoming flow away from the bank in order to create quiescent local

flow conditions to mitigate erosive flow patterns by reducing the bed shear stress along the streambank (Maryland Department of the Environment, 2000; Harman et al., 2001). However, detailed mean flow patterns and turbulence statistics near rock vanes have not been reported yet in the literature. LES was carried out to reproduce the experimental flow condition and elucidate flow physics around the rock vanes. The same background mesh and inlet boundary conditions as the simulation of bankfull flow without a rock vane (see Chapters 4 and 5) are employed in the present case. Figure 6.1 shows the immersed body reconstructed from the measured bed topography. Deeper scour pool at the upstream of the vane and smaller point bar at the inner bank are observed compared to the bankfull flow without the rock vane (see Figure 4.11).

Figure 6.2 shows the comparison of mean streamwise velocity contours for the bankfull flow with (Figure 6.2(a)) and without (Figure 6.2(b)) the rock vane. Quite different mean streamwise flow patterns are observed for the two cases. In the case without the rock vane, the jet-like flow entering from the riffle to the pool approaches and ultimately impinges on the outer bank near the apex of the bend. However, as shown in Figure 6.2(a), the rock vane prevents the jet from impinging on the outer bank near the apex. It rather deflects the oncoming high velocity core away from the wall of the outer bank and creates low velocity regions near the outer bank past the apex. Such low velocities are expected to mitigate erosion of the outer bank by reducing the bed shear stress along the streambank. It is also observed from the figure that the local flow velocity above the rock vane is increased due to the contraction of the flow area.

Figure 6.3 shows the comparison of TKE contours for the bankfull flow with (see Figure 6.3(a)) and without (see Figure 6.3(b)) the rock vane. Both simulations clearly show the presence of the inner and outer bank shear layers. As shown in Figure 6.3(a), the presence of the rock vane strengthens the outer bank shear layer, by increasing the levels of TKE, and displaces its location toward the channel center. It is shown

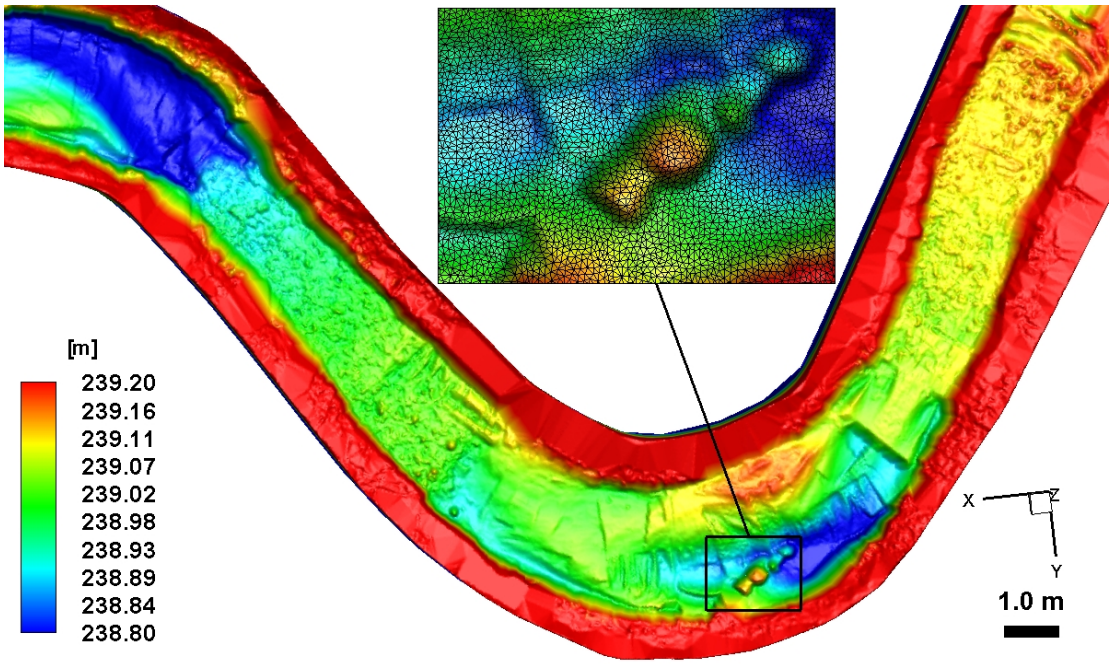

Figure 6.1: Immersed body generated from the measured bed topography of the bankfull flow with a rock vane (the contour levels denote the bed elevation; the flow direction is from right to left).

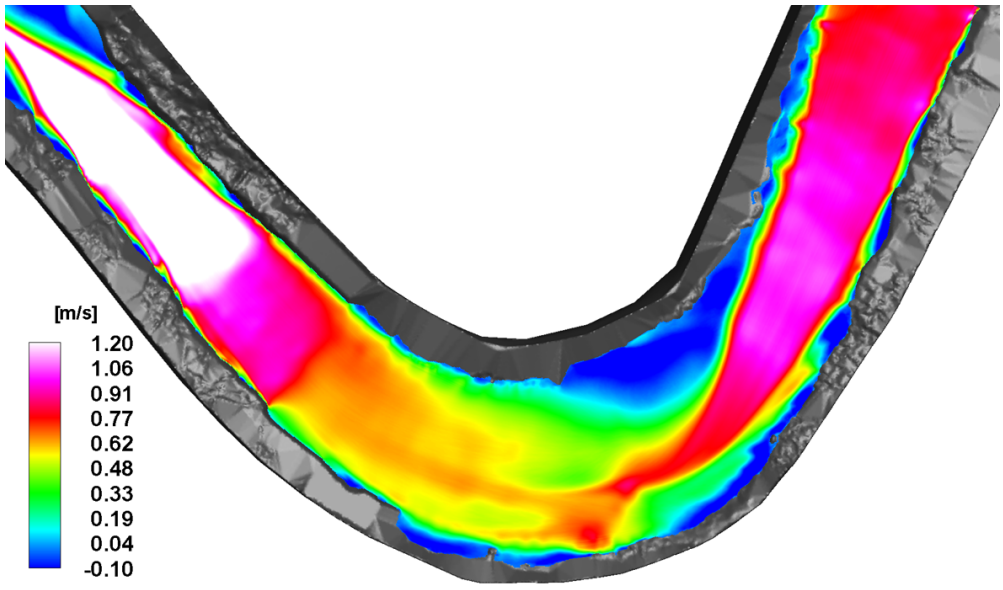

(a) With the rock vane.

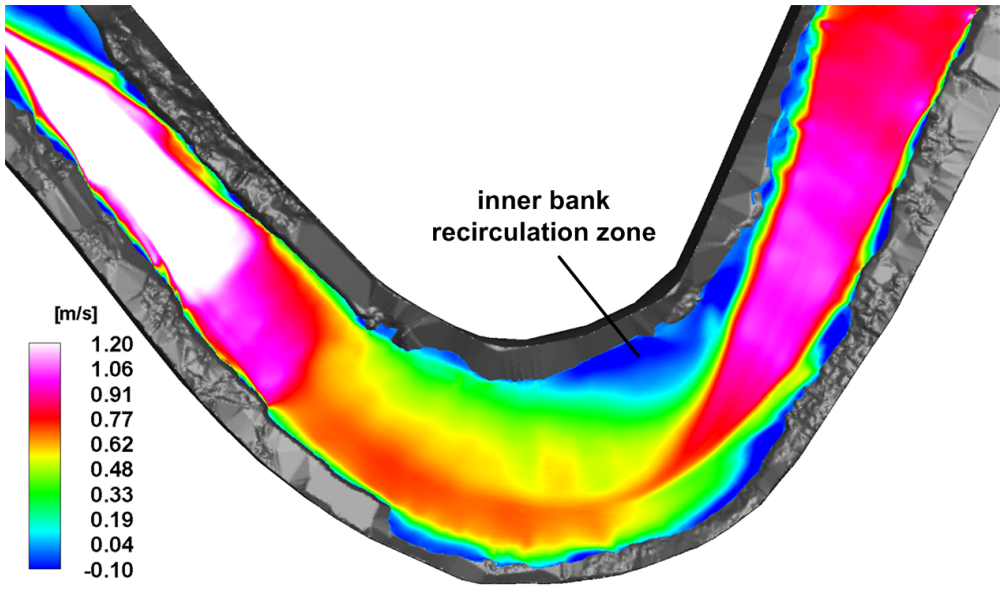

(b) Without the rock vane.

Figure 6.2: Comparison of mean streamwise velocity contours for the bankfull flow with (top) and without (bottom) the rock vane computed by LES (the flow direction is from right to left).

in Chapter 5 that the line of convergence is formed along the outer bank shear layer, and we can infer that the displacement of the location of the outer bank shear layer may displace the location of the line of the convergence toward the channel center as well. It is confirmed in Figure 6.4 which compares the two-dimensional streamlines at the water surface for bankfull and base flows and clearly shows the displacement of the line of convergence toward the channel center. As discussed in Chapter 5, the outer bank shear layer is the footprint of the two counter-rotating secondary flow cells which create strong downward flow from the water surface toward the channel bed. Moreover, the downward common flow between the two cells provides the driving mechanism for increased erosion and channel deepening along the channel thalweg. The location where the outer and inner bank flows collide at the surface is marked by the line of convergence in the surface streamlines, which for the case with the rock vane structure are shown in Figure 6.4(a). Comparing this figure with the figure for the no-structure case (Figure 6.4(b)) as well the respective figures showing the TKE distribution on the surface (Figure 6.3(a) and 6.3(b)), would lead to the conclusion that the installation of the rock vane structure would ultimately cause the channel thalweg to be displaced toward the inner bank. Some evidence in support of this conjecture are provided by the measured stream bathymetries for the two cases. Comparing Figure 4.11 with Figure 6.1 shows that when the structure is installed the channel thalweg near the apex is indeed displaced toward the center of the channel.

To highlight the effect of a single rock vane structure on the secondary flow patterns within the meander bend, we plot in Figure 6.5 two-dimensional streamlines at several cross sections near the apex both with and without the structure. The streamline patterns in Figure 6.5(a) confirms that the main function of the rock vane is to displace the outer bank shear layer toward the channel center.

Figure 6.6 shows the comparison of mean bed shear stress contours with and without

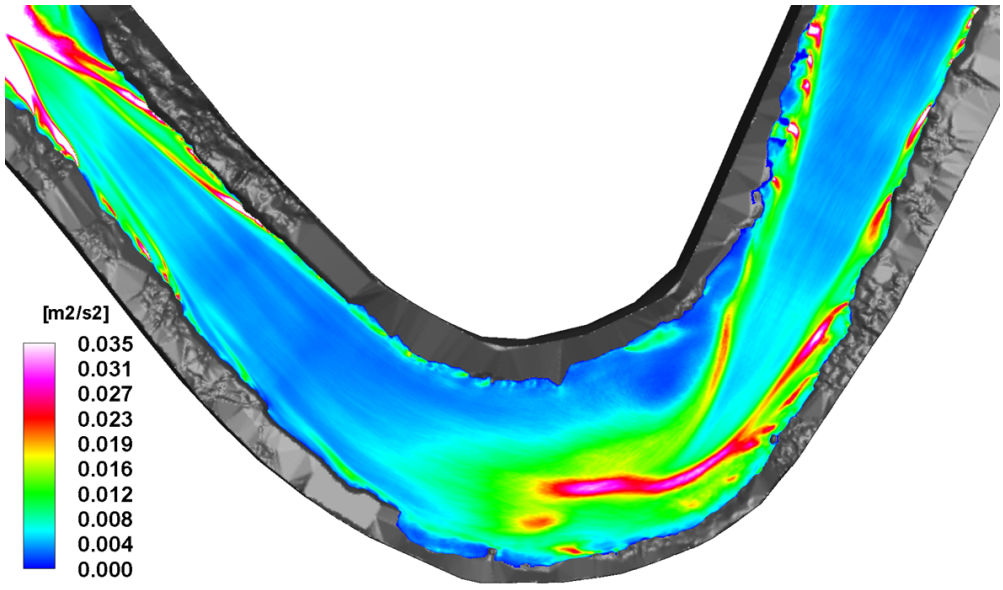

(a) With the rock vane.

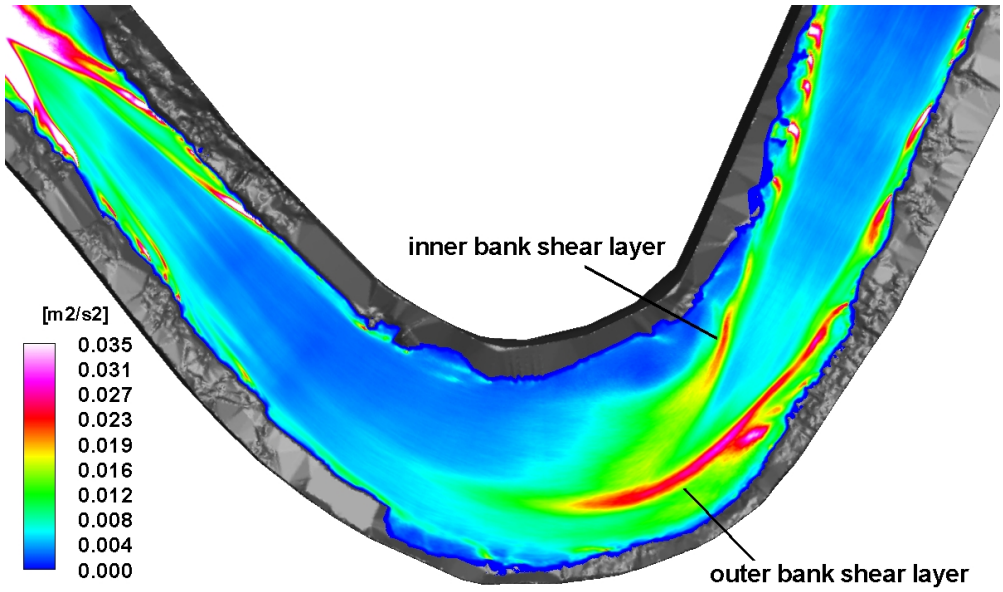

(b) Without the rock vane.

Figure 6.3: Comparison of TKE contours at the water surface for the bankfull flow with (top) and without (bottom) the rock vane computed by LES (the flow direction is from right to left).

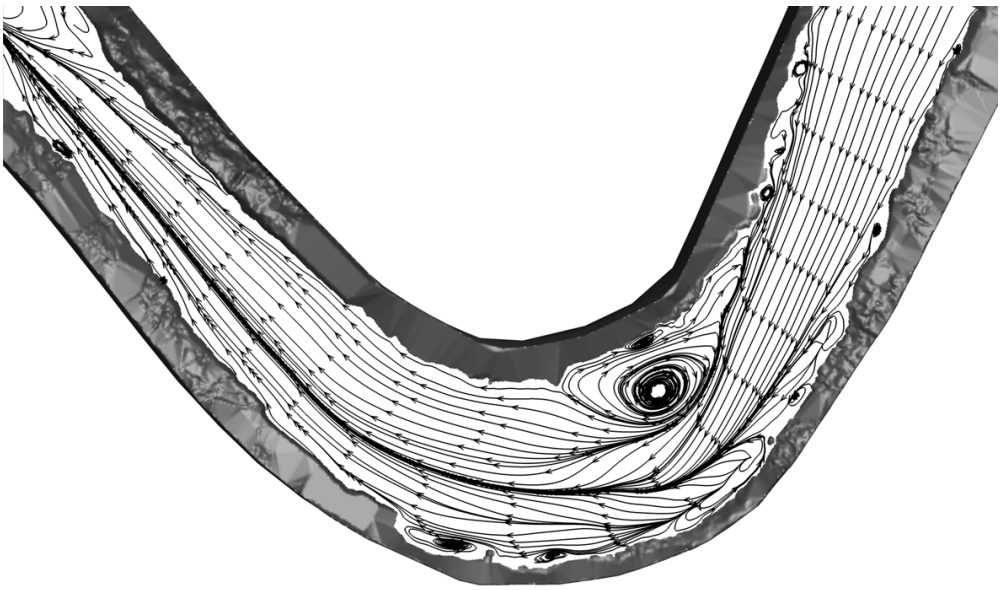

(a) With the rock vane.

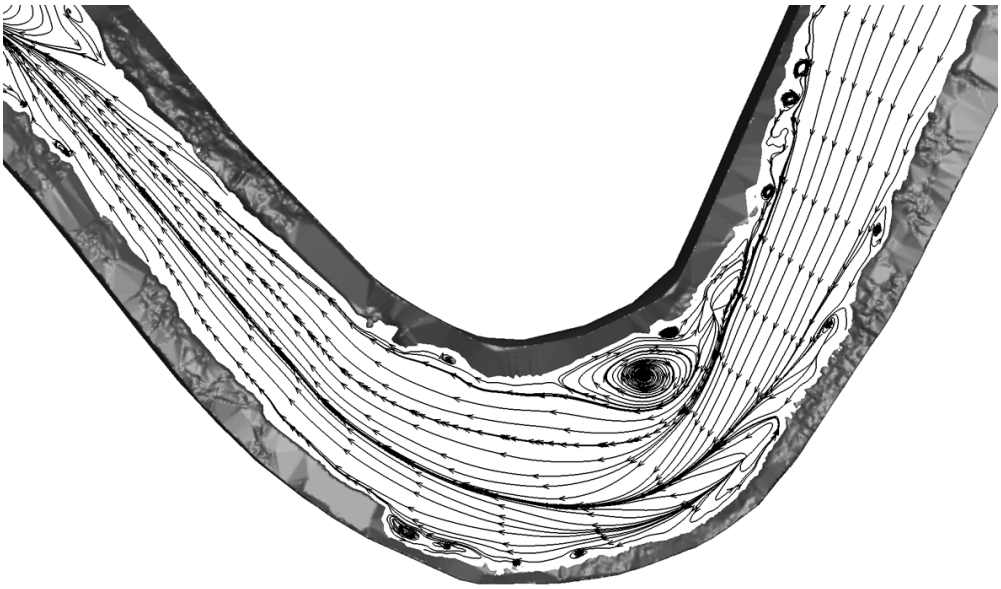

(b) Without the rock vane.

Figure 6.4: Comparison of two-dimensional streamlines at the water surface for the bankfull flow with (top) and without (bottom) the rock vane computed by LES (the flow direction is from right to left).

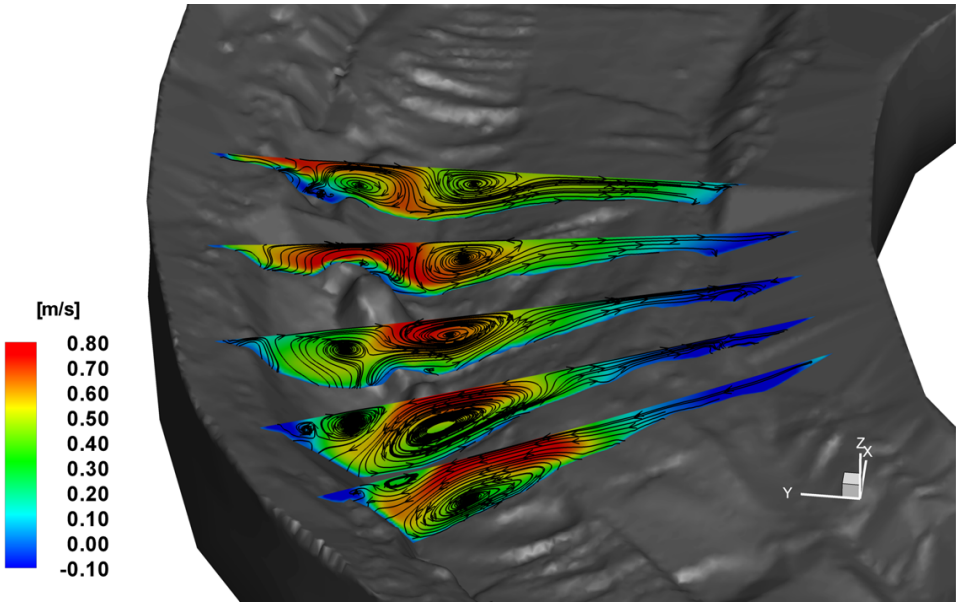

(a) With the rock vane.

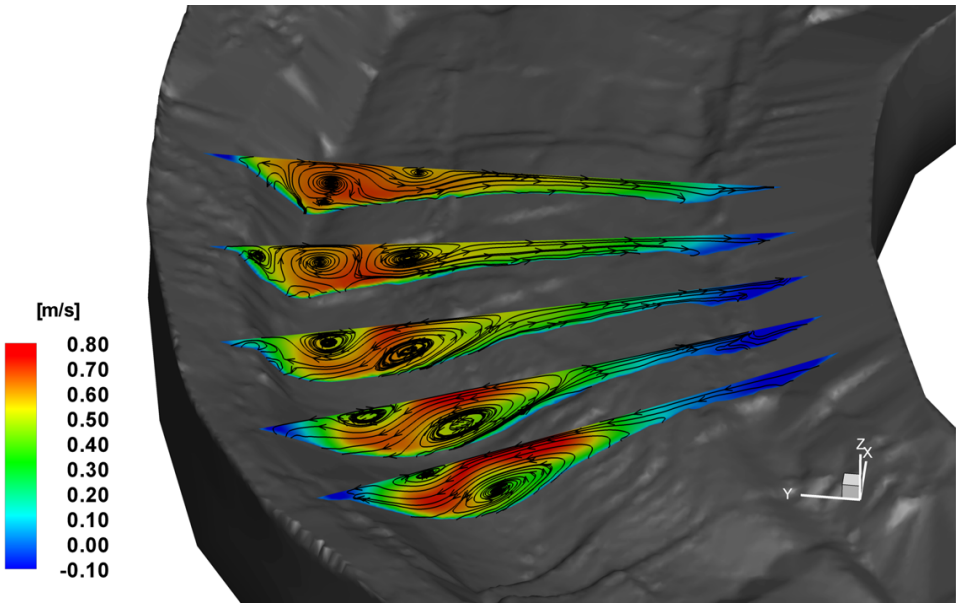

(b) Without the rock vane.

Figure 6.5: Comparison of contours of mean streamwise velocity and two-dimensional streamlines at cross sections near the apex for the bankfull flow with (top) and without (bottom) the rock vane computed by LES. (the flow direction is from bottom to top).

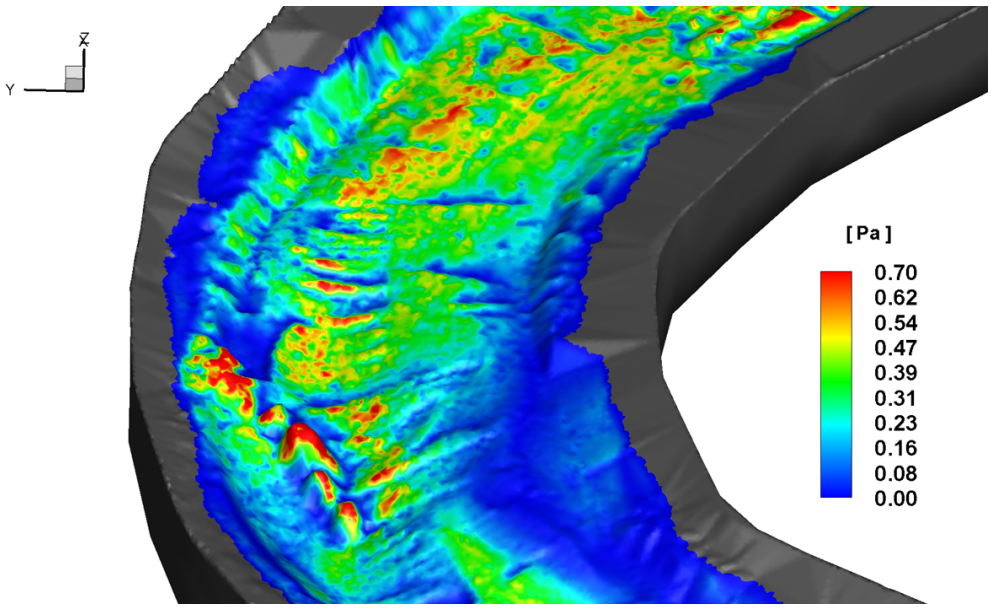

(a) With the rock vane.

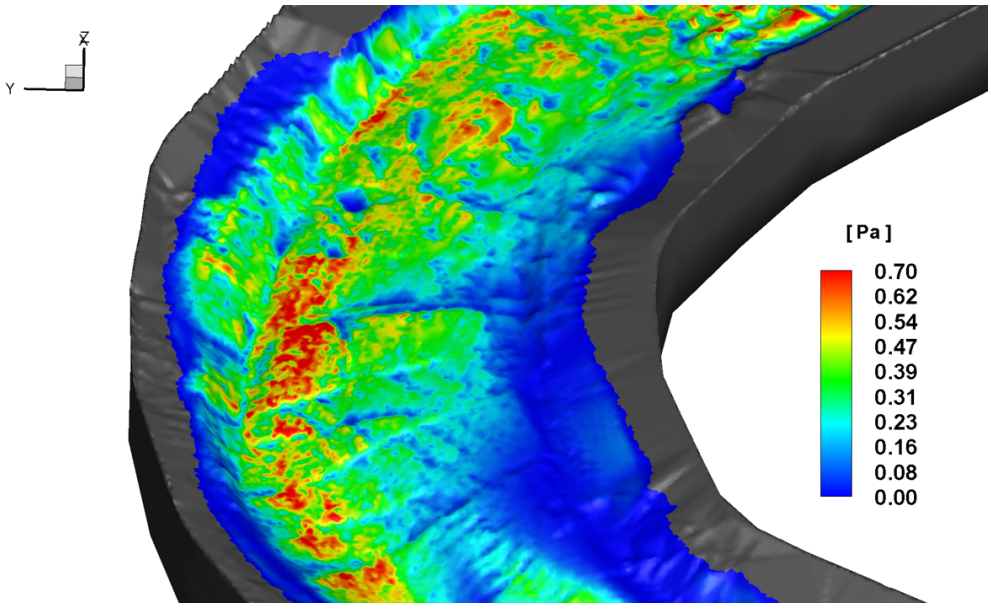

(b) Without the rock vane.

Figure 6.6: Comparison of mean bed shear stress contours for the bankfull flow with (top) and without (bottom) the rock vane computed by LES (the flow direction is from bottom to top).

the vane. The figure shows that with the vane installed the high shear stress regions at the thalweg near the outer bank (see Figure 6.6(b)) are displaced toward the channel center (see Figure 6.6(a)) and a pocket of overall lower bed shear stress is formed along the outer streambank past the apex. These observations are consistent with the mean velocity patterns shown above.

The LES results shown above and subsequent discussions demonstrate that even a single rock vane structure can have a profound effect on the hydrodynamics within the meander bend. These results also show that the numerical method developed in this work can be used to identify the physical mechanisms via which the vane, or any structure or a series of structures for that matter, impacts the flow. By doing so the method can serve as a powerful engineering tool for evaluating the performance of various types of structures and developing design guidelines based on detailed understanding of the flow physics rather than on ad hoc empirical arguments, as typically done in stream restoration practice today.

Chapter 7

Summary and conclusions

A versatile numerical model for carrying out coherent-structure resolving simulations (URANS or LES) of turbulent flows in real-life natural streams has been developed and validated. A major feature of the model is that it employs a sharp-interface immersed boundary modeling framework, the CURVIB method, and can thus handle the arbitrarily complex bathymetry of natural streams resulting from roughness elements and/or embedded natural and man-made structures. Wall modeling was incorporated in the the context of the CURVIB method to enable LES and URANS simulations of turbulent flows on grids that are not sufficiently fine to resolve the laminar sublayer. An important feature of the method is its computational efficiency, which made high-resolution three-dimensional unsteady simulations in long and shallow open channels discretized with stretched, high-aspect-ratio meshes feasible. The efficiency of the method is derived from the fractional step approach employed to solve the incompressible Navier-Stokes equations in conjunction with the algebraic multigrid strategy implemented to accelerate the convergence of the Poisson equation for the pressure.

High resolution measurements of the SAFL OSL streambed were collected and used to construct a computational grid that resolves cm-scale roughness elements on the

bed. No attempt was made to calibrate the numerical model for roughness since the simulations were able to resolve directly vortex shedding from individual small-scale roughness elements in the two riffle zones.

Even though both URANS and LES yielded overall similar results for the mean velocity field some important discrepancies were observed in the predicted TKE fields. Namely, the $k-\omega$ model yielded TKE levels at the water surface in the riffle zones nearly one order of magnitude higher than those measured and calculated with LES and the SST model. This striking finding is attributed to the inherent limitation of two-equation, isotropic eddy viscosity models in flows with regions of flow stagnation–the so-called stagnation point anomaly. The SST model does not suffer from this anomaly since it incorporates a limiter in the TKE production term.

In the pool region in between the two riffles of the bankfull flow the LES and URANS models yielded similar overall flow patterns on the free-surface but the LES did predict the existence of sharp shear layers along inner and outer banks, which were not evident in the two URANS predictions. The sharp shear layers are found to be associated with the high level of anisotropy of turbulence, which cannot be handled by the isotropic RANS models.

Comparisons between mean velocity and turbulence statistics measurements obtained in the pool region and the simulations showed that all three models yielded similar results for the mean velocity profiles but the $k-\omega$ model over-predicted the TKE near the bed. Overall, however, and given the uncertainties involved in obtaining measurements in a field-scale facility, such as the OSL, and the fact that no calibration of any of the three turbulence models was attempted the computed results were in reasonable agreement with the measurements. It is important to note, however, that the comparisons between measurements and simulations underscore the difficulties in

validating computational models at field scale where typically measurements are feasible only at relatively few locations. In fact, such comparisons could lead to erroneous results about the predictive capabilities of the various models. While from the mean velocity and TKE profile comparisons it follows that both the LES and RANS-SST model appear to give satisfactory results, there are major qualitative and quantitative differences among the two flowfields in several regions of the flow. As discussed above, the RANS models fail to capture the jet-like flow at the free-surface, the existence of the inner bank recirculation for the bankfull case, and the inner bank secondary flow cell. Even though not resolved by the present measurements, all these are important features of flows in natural meander bends, which have significant implications in terms of both hydrodynamics and morphodynamics. Only the LES was able to resolve these flow phenomena, which underscores the major computational challenge for obtaining accurate predictions of turbulent flows in natural waterways.

The computed results were analyzed to probe the complexity of the three-dimensional flow within the stream, elucidate the underlying physical mechanisms, and provide, at least for the simulated flow conditions, a complete description of meander bend hydrodynamics. The most important findings regarding the physics of the flow in a natural meander bend as they emerge from the LES results are summarized as follows.

The flowfield in the riffle for base and bankfull flows is dominated by the heterogeneously distributed, large-scale roughness elements, which: 1) increase turbulence anisotropy; 2) give rise to multiple streamwise vortices driven by the anisotropy of the Reynolds stresses; and 3) produce a highly heterogeneous bed shear stress field characterized by multiple pockets of high shear stress intertwined with regions of nearly zero shear stress.

The good comparison between computations and the measurements, in spite of oversimplified inflow conditions, suggests that the riffles act to diminish the effect of inflow

velocity boundary conditions on downstream flow development. This is attributed to the intense turbulent motions induced within the riffle by large-scale roughness elements, which render the flowfield well mixed and rapidly disintegrate upstream flow structures. This finding has important implications for the numerical simulation of natural stream flows for which accurate inflow conditions are difficult to specify numerically. It should be pointed out, however, that this favorable function of the riffle in our case is enhanced by the shallowness of the flow and the fact that the roughness elements on the bed are high enough to protrude well into the outer layer of the flowfield. Therefore, riffles may not be as effective in diminishing upstream memory effects as in the present case in deeper flow situations, such as those that can occur during flooding events.

In the bankfull flow case, the flow at the water surface in the pool downstream of the riffle is characterized by the formation of a high velocity jet that shifts toward the outer bank and appears to start diffusing laterally downstream of the bend apex. The high velocity jet is outlined by two well defined shear layers, marked by increased levels of TKE, along the inner and outer banks. The inner bank shear layer is associated with the recirculation zone that develops above the point bar and is shown to decay immediately downstream of the apex of the inner bank recirculation bubble. The outer bank shear layer, on the other hand, is shown to be linked to the complex and highly three-dimensional interaction between the secondary flow patterns with the streamwise flow within the bend. The two shear layers are not evident in the base flow case for which the levels of TKE at the water-surface in the pool region are significantly lower than those observed for the bankfull flow case. This should be attributed to the fact that for the base flow case there is no large recirculation zone along the inner bank and the outer bank secondary flow cell is weaker and located closer to the outer ban compared to the bankfull case flowfields.

A complex secondary flow emerges within the bend that consists of the previously

observed in field studies, laboratory experiments and numerical simulations, inner and outer bank cells. Our results support previous findings regarding the mechanisms that give rise to the outer bank cell (OBC), which were derived from laboratory experiments with simple, prismatic channel cross sections. Namely, it was shown that the OBC originates near the outer bank at the downstream end of the riffle in a region of increased turbulence anisotropy but is sustained well downstream of the apex of the bend even in regions where the anisotropy is negligible, presumably due to the action of the curvature induced centrifugal force that acts in the same direction as the near-bed OBC flow. The inner bank cell, on the other hand, appears suddenly as the flow passes around the point bar but decays rapidly at the downstream end of the point bar. This finding, along with the sense of rotation of this cell, is consistent previous findings that the formation of the IBC is driven by the classical secondary flow mechanism in curved open channels associated with the imbalance of the centrifugal force and the lateral pressure gradient. It is presumably because of this reason that the local increase in streamline curvature induced by the presence of the point bar along the inner bank appears to have a profound effect on the formation, growth and downstream evolution of the OBC.

An important finding from the bankfull flow simulation, which to the best of our knowledge has not yet been reported in previous studies, is that for the bankfull flow case the OBC persists further downstream than the IBC well after the flow passes the apex. Nevertheless, both secondary flow cells were found to decay well before the flow reaches the next riffle. This finding implies that each pool-riffle sequence in natural meander bends involves its own physical processes of generation and destruction of helical motions, which are decoupled from those in previous sequences.

The relative location and sense of rotation of the OBC and IBC leads to the formation of a half saddle point at the water surface near the outer bank in the cross sectional flow streamlines. This saddle marks the point where the counter-rotating IBC and OBC

flows collide at the water surface giving rise to a strong downward flow from the surface toward the channel thalweg. Such flow pattern transports high momentum flow from the surface toward the bed reducing the surface velocities near the outer bank and giving rise to the inner bank shear layer while increasing the bed shear stress in the thalweg. Therefore, the complex interaction between the OBC and IBC could be an important factor determining stream morphodynamics by promoting channel deepening.

For the bankfull flow case the half saddle point in the cross sectional streamlines at the water surface coincides with the region of increased TKE that marks the outer bank shear layer. Turbulence in this region is highly anisotropic as most of the TKE is shown to be produced by transverse velocity fluctuations, presumably due to the lateral, low frequency flapping of the point where the IBC and OBC flows collide at the surface. Turbulence anisotropy is also shown to be important in several other regions within the stream, such as throughout the riffles and around the point bar. This finding has important implications for numerical simulations of turbulence in natural waterways pointing to the need for adopting turbulence models that can accurately account for the anisotropy of the Reynolds stresses.

In the bankfull flow case, recirculation zones are observed along both the inner and outer banks of the bend. The outer bank recirculation zones are relatively minor features of the flow induced by local topography, i.e. sudden area expansions. The inner bank recirculation zone, on the other hand, is a dominant large-scale feature of the mean flow and is shown to consist of multiple recirculation eddies that span almost the entire area above the point bar. A striking finding in this regard is that the center of the primary recirculation eddy is located directly above the crest of the point bar, which points to the conclusion that recirculation zones play an important role in the formation of bars in alluvial streams. The slowly moving, low velocity flow within the inner bank recirculation zone provides the ideal hydrodynamic environment for fine

sediments transported there by the IBC as bedload to be trapped and eventually deposit forming the point bar.

Recirculation or dead zones are important factors in several biogeochemical processes in waterways (Reynolds, 2000; Engelhardt et al., 2004). Such zones are typically characterized by low velocities and can thus increase significantly the residence time of pollutants, nutrients, or suspended sediment loads. It also known that turbulence mixing or velocity can influence the distribution of aquatic organisms such as phytoplankton (Huisman et al., 2002; Engelhardt et al., 2004; Hondzo and Wüest, 2009) or fish (Cotel et al., 2006). Therefore, the low turbulence mixing rate in recirculating regions coupled with the low overall mean flow velocities could significantly impact the quality of aquatic habitats and the ability of streams to support life and process nutrients. The results presented in this work show that the arbitrarily complex topography of natural streams could induce several regions of flow recirculation both along the inner and outer banks of the stream. As such, the developed numerical method, coupled with high-resolution topographic measurements, could be a useful tool for understanding the role of hydrodynamics on stream biogeochemical processes and developing science-based approaches for restoring waterways.

Comparing the results of base and bankfull flow cases shows that a line of convergence is also present in the base flow case but compared to the bankfull flow case this line remains closely attached to the outer bank. The size of the outer bank cell in the base flow case is much smaller than that in the bankfull flow case. Formation of the smaller outer bank cell can be attributed to the shallow flow depth for the base flow case which limits the growth of the outer bank cell. An important difference between the two cases follows from the TKE contours in the riffle region. For the base flow case multiple pockets of large TKE values appear on the water surface, which are essentially the surface footprints of individual roughness elements in the riffle. No such structure is

observed, however, in the TKE contours for the bankfull flow case, which appear to be relatively homogeneous within the central part of the riffle. This trend is attributed to the differences in the flow depth between the base and bankfull cases. For very shallow flows over rough beds, the roughness elements penetrate well into the outer layer of the flow and consequently leaves clear footprints in the TKE field on the surface.

To study flow physics around instream structures, LES was carried out for the bankfull flow case with a rock vane instream structure installed along the outer bank of the bend. The results shows that the rock vane prevents the jet-like flow from impinging on the outer bank near the apex and deflects the oncoming high velocity core away from the wall of the outer bank. Moreover, it creates low velocity regions near the outer bank past the apex. Such low velocity regions are expected to mitigate erosion of the outer bank by reducing the bed shear stress along the streambank. The results also reveals that the main function of the rock vane is to displace the outer bank shear layer toward the channel center and to cause the channel thalweg to be displaced toward the inner bank as well. This simulation demonstrates the utility of the model as a powerful tool for developing science-based design guidelines for stream restoration.

The numerical method developed herein is a powerful tool both for obtaining fundamental insights into the complex three-dimensional structure of turbulence in natural waterways and for improving the designs of hydraulic structures. It has great potential for future applications. For instance, this model can be used to design hydraulic or coastal structures such as bridge foundations, stream-restoration structures, spillways, breakwaters, etc. The nonlinear three-dimensional free-surface model in conjunction with RANS and LES models can be used to predict complex free-surface motions in rivers, coasts and oceans. Moreover, the flow solver coupled with the sediment transport model enables geomorphodynamics simulations (Khosronejad et al., 2010).

Bibliography

J. D. Abad, B. L. Rhoads, I. Güneralp, and M. H. García. Flow structure at different stages in a meander-bend with bendway weirs. *Journal of Hydraulic Engineering*, 134 (8):1052–1063, 2008.

V. Armenio and U. Piomelli. A Lagrangian mixed subgrid-scale model in generalized coordinates. *Flow Turbulence and Combustion*, 65(1):51–81, 2000.

R. A. Bagnold. Some aspects of the shape of river meanders. *U.S. Geological Survey Professional Paper*, 282-E:135–144, 1960.

W. V. Balen, W. S. J. Uijttewaal, and K. Blanckaert. Large-eddy simulation of a mildly curved open-channel flow. *Journal of Fluid Mechanics*, 630:413–442, 2009.

J. C. Bathurst, C. R. Thorne, and R. D. Hey. Secondary flow and shear stress at river bends. *Journal of the Hydraulics Division, ASCE*, 105(HY10):1277–1295, 1979.

E. S. Bernhardt, M. A. Palmer, J. D. Allan, G. Alexander, K. Barnas, S. Brooks, J. Carr, S. Clayton, C. Dahm, J. Follstad-Shah, D. Galat, S. Gloss, P. Goodwin, D. Hart, B. Hassett, R. Jenkinson, S. Katz, G. M. Kondolf, P. S. Lake, R. Lave, J. L. Meyer, T. K. O'Donnell, L. Pagano, B. Powell, and E. Sudduth. Synthesizing U.S. River Restoration Efforts. *Science*, 308(5722):636–637, 2005.

K. Blanckaert and H. J. de Vriend. Secondary flow in sharp open-channel bends. *Journal of Fluid Mechanics*, 498:353–380, 2004.

I. Borazjani and F. Sotiropoulos. Numerical investigation of the hydrodynamics of carangiform swimming in the transitional and inertial flow regimes. *Journal of Experimental Biology*, 211(10):1541–1558, 2008.

I. Borazjani and F. Sotiropoulos. On the role of form and kinematics on the hydrodynamics of self-propelled body/caudal fin swimming. *Journal of Experimental Biology*, 213(1):89–107, 2010.

I. Borazjani, L. Ge, and F. Sotiropoulos. Curvilinear immersed boundary method for simulating fluid structure interaction with complex 3D rigid bodies. *Journal of Computational Physics*, 227(16):7587 – 7620, 2008.

I. Borazjani, F. Sotiropoulos, E. Malkiel, and J. Katz. On the role of copepod antenna in the production of hydrodynamic force during hopping. *Journal of Experimental Biology*, accepted, 2010.

W. L. Briggs, V. E. Henson, and S. F. McCormick. *A multigrid tutorial (2nd ed.)*. Society for Industrial and Applied Mathematics, Philadelphia, PA, USA, 2000.

P. N. Brown and Y. Saad. Hybrid Krylov methods for nonlinear systems of equations. *SIAM Journal on Scientific and Statistical Computing*, 11(3):450–481, 1990.

W. Cabot and P. Moin. Approximate wall boundary conditions in the large-eddy simulation of high reynolds number flow. *Flow Turbulence and Combustion*, 63(1-4): 269–291, 2000.

H. C. Chen, V. C. Patel, and S. Ju. Solutions of reynolds-averaged Navier-Stokes equations for three-dimensional incompressible flows. *Journal of Computational Physics*, 88(2):305 – 336, 1990.

Q. Chen, G. Dai, and H. Liu. Volume of fluid model for turbulence numerical simulation of stepped spillway overflow. *Journal of Hydraulic Engineering*, 128(7):683–688, 2002.

D. C. Chu and G. E. Karniadakis. A direct numerical simulation of laminar and turbulent flow over riblet-mounted surfaces. *Journal of Fluid Mechanics*, 250:1–42, 1993.

A. J. Cotel, P. W. Webb, and H. Tritico. Do brown trout choose locations with reduced turbulence? *Transactions of the American Fisheries Society*, 135(3):610–619, 2006.

A. O. Demuren and W. Rodi. Calculation of turbulence-driven secondary motion in non-circular ducts. *Journal of Fluid Mechanics*, 140:189–222, 1984.

J. E. Dennis and R. B. Schnabel. *Numerical Methods for Unconstrained Optimization and Nonlinear Equations*. Prentice-Hall, Englewood Cliffs, NJ, 1983.

D. L. Derrick. Four years later, harland creek bendway weir/willow post bank stabilization demonstration project. In *Proceedings of 1998 International Water Resources Engineering Conference, ASCE.*, Memphis, TN, August 1998.

W. J. Devenport and R. L. Simpson. Time-dependent and time-averaged turbulence structure near the nose of a wing-body junction. *Journal of Fluid Mechanics*, 210: 23–55, 1990.

W. E. Dietrich and J. D. Smith. Influence of the point bar on flow through curved channels. *Water Resources Research*, 19:1173–1192, 1983.

W. E. Dietrich, J. D. Smith, and T. Dunne. Flow and sediment transport in a sand bedded meander. *The Journal of Geology*, 87(3):305–315, 1979.

B. A. Doll, G. L. Grabow, K. L. Hall, J. Halley, W. A. Harman, G. D. Jennings, and D. E. Wise. *Stream Restoration: A Natural Channel Design Handbook*. NC Stream Restoration Institute, NC State University, 2003.

S. Dong, G. E. Karniadakis, A. Ekmekci, and D. Rockwell. A combined direct numerical simulation-particle image velocimetry study of the turbulent near wake. *Journal of Fluid Mechanics*, 569:185–207, 2006.

P. A. Durbin. On the k-3 stagnation point anomaly. *International Journal of Heat and Fluid Flow*, 17(1):89 – 90, 1996.

S. C. Eisenstat and H. F. Walker. Choosing the forcing terms in an inexact newton method. *SIAM Journal on Scientific Computing*, 17(1):16–32, 1996.

C. Engelhardt, A. Kruger, A. Sukhodolov, and A. Nicklisch. A study of phytoplankton spatial distributions, flow structure and characteristics of mixing in a river reach with groynes. *Journal of Plankton Research*, 26(11):1351–1366, 2004.

C. Escauriaza and F. Sotiropoulos. Initial stages of erosion and bed-form development in turbulent junction flows. *Journal of Geophysical Research*, under review, 2010.

E. A. Fadlun, R. Verzicco, P. Orlandi, and J. Mohd-Yusof. Combined immersed-boundary finite-difference methods for three-dimensional complex flow simulations. *Journal of Computational Physics*, 161(1):35 – 60, 2000.

F. N. Felten and T. S. Lund. Kinetic energy conservation issues associated with the collocated mesh scheme for incompressible flow. *Journal of Computational Physics*, 215(2):465–484, 2006.

J. C. Fischenich. Effects of riprap on riverine and riparian ecosystems. Technical Report ERDC/EL TR-03-4, Army Corps of Engineers Environmental Laboratory, 2003.

K. M. Frothingham and B. L. Rhoads. Three-dimensional flow structure and channel change in an asymmetrical compound meander loop, Embarras River, Illinois. *Earth Surface Processes and Landforms*, 28(6):625–644, 2003.

L. Ge and F. Sotiropoulos. 3D unsteady RANS modeling of complex hydraulic engineering flows. I: Numerical model. *Journal of Hydraulic Engineering*, 131(9):800–808, 2005.

L. Ge and F. Sotiropoulos. A numerical method for solving the 3D unsteady incompressible Navier-Stokes equations in curvilinear domains with complex immersed boundaries. *Journal of Computational Physics*, 225(2):1782–1809, 2007.

L. Ge, S. O. Lee, F. Sotiropoulos, and T. Sturm. 3D unsteady RANS modeling of complex hydraulic engineering flows. II: Model validation and flow physics. *Journal of Hydraulic Engineering*, 131(9):809–820, 2005.

M. Germano, U. Piomelli, P. Moin, and W. H. Cabot. A dynamic subgrid-scale eddy viscosity model. *Physics of Fluids A*, 3(7):1760–1765, 1991.

A. Gilmanov and F. Sotiropoulos. A hybrid cartesian/immersed boundary method for simulating flows with 3D, geometrically complex, moving bodies. *Journal of Computational Physics*, 207(2):457 – 492, 2005.

D. H. Gray and R. B. Sotir. *Biotechnical and soil bioengineering-slope stabilization: a practical guide for erosion control.* John Wiley and Sons, New York, NY., 1996.

W. A. Harman, G. D. Jennings, K. R. Tweedy, J. Buck, and D. L. Taylor. Lessons learned from designing and constructing in-stream structures. In *Proc., Wetland Engineering and River Restoration Conf. 2001 CD-ROM, ASCE*, Reston, VA, 2001.

R. D. Henderson and G. E. Karniadakis. Unstructured spectral element methods for

simulation of turbulent flows. *Journal of Computational Physics*, 122(2):191–217, 1995.

V. E. Henson and U. M. Yang. BoomerAMG: A parallel algebraic multigrid solver and preconditioner. *Applied Numerical Mathematics*, 41(1):155–177, 2002.

R. D. Hey and C. R. Thorne. Secondary flows in river channels. *Area*, 7:191–195, 1975.

C. W. Hirt and B. D. Nichols. Volume of fluid (vof) method for the dynamics of free boundaries. *Journal of Computational Physics*, 39(1):201 – 225, 1981.

B. R. Hodges and R. L. Street. On simulation of turbulent nonlinear free-surface flows. *Journal of Computational Physics*, 151(2):425–457, 1999.

M. Hondzo and A. Wüest. Do microscopic organisms feel turbulent flows? *Environmental Science & Technology*, 43:764–768, 2009.

J. Huisman, M. Arrayás, U. Ebert, and B. Sommeijer. How do sinking phytoplankton species manage to persist? *The American Naturalist*, 159(3):245–254, 2002.

J. A. C. Humphrey, J. H. Whitelaw, and G. Yee. Turbulent flow in a square duct with strong curvature. *Journal of Fluid Mechanics*, 103:443–463, 1981.

G. Iaccarino and R. Verzicco. Immersed boundary technique for turbulent flow simulations. *Applied Mechanics Reviews*, 56(3):331–347, 2003.

J. Jeong and F. Hussain. On the identification of a vortex. *Journal of Fluid Mechanics*, 285:69–94, 1995.

G.-S. Jiang and C.-W. Shu. Efficient implementation of weighted ENO schemes. *Journal of Computational Physics*, 126(1):202 – 228, 1996. ISSN 0021-9991.

H. Johannesson and G. Parker. Secondary flow in mildly sinuous channel. *Journal of Hydraulic Engineering*, 115(3):289–308, 1989.

P. A. Johnson, R. D. Hey, M. Tessier, and D. L. Rosgen. Use of vanes for control of scour at vertical wall abutments. *Journal of Hydraulic Engineering*, 127(9):772–778, 2001.

P. A. Johnson, R. D. Hey, E. R. Brown, and D. L. Rosgen. Stream restoration in the vicinity of bridges. *Journal of the American Water Resources Association*, 38(1): 55–67, 2002a.

P. A. Johnson, R. L. Tereska, and E. R. Brown. Using technical adaptive management to improve design guidelines for urban instream structures. *Journal of the American Water Resources Association*, 38(4):1143–1152, 2002b.

S. A. Jordan. A large-eddy simulation methodology in generalized curvilinear coordinates. *Journal of Computational Physics*, 148(2):322 – 340, 1999.

J. P. T. Kalkwijk and H. J. de Vriend. Computation of the flow in shallow river bends. *Journal of Hydraulic Research*, 18(4):327 – 342, 1980.

S. Kang and F. Sotiropoulos. Flow phenomena and mechanisms in a natural meandering stream with a pool-riffle sequence: Insights gained via numerical simulation. *Journal of Geophysical Research*, under review, 2010.

S. Kang, A. Lightbody, C. Hill, and F. Sotiropoulos. High-resolution numerical simulation of turbulence in natural waterways. *Advances in Water Resources*, under review, 2010.

G.-S. Karamanos and G. E. Karniadakis. A spectral vanishing viscosity method for large-eddy simulations. *Journal of Computational Physics*, 163(1):22 – 50, 2000.

J. B. Kauffman, R. L. Beschta, N. Otting, and D. Lytjen. An ecological perspective of riparian and stream restoration in the western united states. *Fisheries*, 22(5):12–24, 1997.

E. A. Keller. Development of alluvial stream channels: A five-stage model. *Geological Society of America Bulletin*, 83:1531–1536, 1972.

C. J. Keylock, R. J. Hardy, D. R. Parsons, R. I. Ferguson, S. N. Lane, and K. S. Richards. The theoretical foundations and potential for large-eddy simulation (LES) in fluvial geomorphic and sedimentological research. *Earth-Science Reviews*, 71(3-4): 271 – 304, 2005.

A. Khosronejad, S. Kang, I. Borazjani, and F. Sotiropoulos. Curvilinear immersed boundary method for simulating flow field and sediment transport phenomena. *Advances in Water Resources*, in preparation, 2010.

G. Kirkil, S. G. Constantinescu, and R. Ettema. Coherent structures in the flow field around a circular cylinder with scour hole. *Journal of Hydraulic Engineering*, 134(5): 572–587, 2008.

D. A. Knoll and D. E. Keyes. Jacobian-free Newton-Krylov methods: a survey of approaches and applications. *Journal of Computational Physics*, 193(2):357–397, 2004. ISSN 0021-9991.

M. Koken and G. Constantinescu. An investigation of the dynamics of coherent structures in a turbulent channel flow with a vertical sidewall obstruction. *Physics of Fluids*, 21(8):085104, 2009.

Y. G. Lai, L. J. Weber, and V. C. Patel. Nonhydrostatic three-dimensional model for hydraulic flow simulation. I: Formulation and verification. *Journal of Hydraulic Engineering*, 129(3):196–205, 2003.

J. Larsson, F. Lien, and E. Yee. Conditional semicoarsening multigrid algorithm for the Poisson equation on anisotropic grids. *Journal of Computational Physics*, 208(1): 368–383, 2005.

J. Laufer. The structure of turbulence in fully developed pipe flow. Technical Report 1174, NACA, 1954.

H. Le, P. Moin, and J. Kim. Direct numerical simulation of turbulent flow over a backward-facing step. *Journal of Fluid Mechanics*, 330:349–374, 1997.

M. R. Leeder and P. H. Bridges. Flow separation in meander bends. *Nature*, 253: 338–339, 1975.

L. B. Leopold and M. G. Wolman. River meanders. *Geological Society of America Bulletin*, 71(6):769–793, 1960.

L. B. Leopold, R. A. Bagnold, M. G. Wolman, and L. M. Brush. Flow resistance in sinuous and irregular channels. *U.S. Geological Survey Professional Paper*, 282D: 111–134, 1960.

M.-H. Li and K. E. Eddleman. Biotechnical engineering as an alternative to traditional engineering methods: A biotechnical streambank stabilization design approach. *Landscape and Urban Planning*, 60(4):225–242, 2002.

P. Lin and P. L.-F. Liu. A numerical study of breaking waves in the surf zone. *Journal of Fluid Mechanics*, 359(-1):239–264, 1998.

J. L. Lumley. Computational modelling of turbulent flows. *Advances in Applied Mechanics*, 18:126–176, 1978.

K. Mahesh, G. Constantinescu, and P. Moin. A numerical method for large-eddy simulation in complex geometries. *Journal of Computational Physics*, 197(1):215–240, 2004.

R. Martinuzzi and C. Tropea. The flow around surface-mounted, prismatic obstacles placed in a fully developed channel flow. *Journal of Fluids Engineering*, 115(1):85–92, 1993.

Maryland Department of the Environment. *Maryland's waterway construction guidelines*. Water Management Administration, 2000.

A. McCoy, G. Constantinescu, and L. J. Weber. Numerical investigation of flow hydrodynamics in a channel with a series of groynes. *Journal of Hydraulic Engineering*, 134(2):157–172, 2008.

J. J. Mcguirk and W. Rodi. A depth-averaged mathematical model for the near field of side discharges into open-channel flow. *Journal of Fluid Mechanics*, 86(4):761–781, 1978.

F. R. Menter, M. Kuntz, and R. Langtry. Ten years of industrial experience with the SST turbulence model. *Turbulence, Heat and Mass Transfer 4*, pages 625 – 632, 2003.

E. A. Meselhe and F. Sotiropoulos. Three-dimensional numerical model for open-ehannels with free-surfaee variations. *Journal of Hydraulic Research*, 38:115–121, 2000.

H. K. Moffatt. The degree of knottedness of tangled vortex lines. *Journal of Fluid Mechanics*, 35(1):117–129, 1969.

T. Möller and B. Trumbore. Fast, minimum storage ray-triangle intersection. *Journal of Graphics Tools*, 2(1):21–28, 1997.

R. D. Moser, J. Kim, and N. N. Mansour. Direct numerical simulation of turbulent channel flow up to $\mathrm{Re}_\tau = 590$. *Physics of Fluids*, 11(4):943–945, 1999.

N. Nagata, T. Hosoda, T. Nakato, and Y. Muramoto. Three-dimensional numerical model for flow and bed deformation around river hydraulic structures. *Journal of Hydraulic Engineering*, 131(12):1074–1087, 2005.

N. H. Naik and J. V. Rosendale. The improved robustness of multigrid elliptic solvers based on multiple semicoarsened grids. *SIAM Journal on Numerical Analysis*, 30(1): 215–229, 1993. ISSN 00361429.

G. C. Nanson. Point bar and floodplain formation of the meandering Beatton River, northeastern British Columbia, Canada. *Sedimentology*, 27(1):3–29, 1980.

D. Naot. Response of channel flow to roughness heterogeneity. *Journal of Hydraulic Engineering*, 110(11):1568–1587, 1984.

V. S. Neary, F. Sotiropoulos, and A. J. Odgaard. Three-dimensional numerical model of lateral-intake inflows. *Journal of Hydraulic Engineering*, 125(2):126–140, 1999.

J. O'Neil and L. Fitch. Performance audit of instream habitat structures constructed during the period 1982-1990 in southwestern Alberta. *Abstract for meeting of the American Fisheries Society, Rapid City , South Dakota*, 1992.

S. Osher and R. Fedkiw. *The Level Set Method and Dynamic Implicit Surfaces*. Springer-Verlag, New York, 2002.

S. Osher and J. A. Sethian. Fronts propagating with curvature-dependent speed: Algorithms based on hamilton-jacobi formulations. *Journal of Computational Physics*, 79 (1):12 – 49, 1988.

J. Paik and F. Sotiropoulos. Coherent structure dynamics upstream of a long rectangular block at the side of a large aspect ratio channel. *Physics of Fluids*, 17(11):115104, 2005.

J. Paik, C. Escauriaza, and F. Sotiropoulos. On the bimodal dynamics of the turbulent horseshoe vortex system in a wing-body junction. *Physics of Fluids*, 19(4):045107, 2007.

J. Paik, F. Sotiropoulos, and F. Porté-Agel. Detached eddy simulation of flow around two wall-mounted cubes in tandem. *International Journal of Heat and Fluid Flow*, 30(2):286 – 305, 2009.

J. Paik, C. Escauriaza, and F. Sotiropoulos. Coherent structure dynamics in turbulent flows past in-stream structures: Some insights gained via numerical simulation. *Journal of Hydraulic Engineering*, accepted, 2010.

S. V. Patankar. *Numerical Heat Transfer and Fluid Flow*. McGraw-Hill, New York, 1980.

H. J. Perkins. The formation of streamwise vorticity in turbulent flow. *Journal of Fluid Mechanics*, 44(4):721–740, 1970.

B. Ramaswamy and M. Kawahara. Arbitrary lagrangian-eulerianc finite element method for unsteady, convective, incompressible viscous free surface fluid flow. *International Journal for Numerical Methods in Fluids*, 7(10):1053–1075, 1987.

C. S. Reynolds. Hydroecology of river plankton: the role of variability in channel flow. *Hydrological Processes*, 14(16-17):3119–3132, 2000.

J. F. Rodriguez, F. A. Bombardelli, M. H. Garcia, K. M. Frothingham, B. L. Rhoads,

and J. D. Abad. High-resolution numerical simulation of flow through a highly sinuous river reach. *Water Resources Management*, 18(3):1573–1650, 2004.

P. Roni, T. J. Beechie, R. E. Bilby, F. E. Leonetti, M. M. Pollock, and G. R. Pess. A review of stream restoration techniques and a hierarchical strategy for prioritizing restoration in pacific northwest watersheds. *North American Journal of Fisheries Management*, 22(1):1–20, 2002.

M. Rosenfeld, D. Kwak, and M. Vinokur. A fractional step solution method for the unsteady incompressible Navier-Stokes equations in generalized coordinate systems. *Journal of Computational Physics*, 94(1):102–137, 1991.

D. L. Rosgen. The cross vane, W-weir and J-hook structures: Their description, design and application for stream stabilization and river restoration. *Proceedings, Wetland Engineering and River Restoration Conference CD-ROM, ASCE, Reston, VA.*, 2001.

D. M. Rubin, J. C. Schmidt, and J. N. Moore. Origin, structure, and evolution of a reattachment bar, Colorado River, Grand Canyon, Arizona. *Journal of Sedimentary Research*, 60(6):982–991, 1990.

J. W. Ruge and K. Stüben. *Algebraic multigrid, in: S.F. McCormick (Ed.), Multigrid Methods, Frontiers in Applied Mathematics*, volume 3. SIAM, Philadelphia, 1987.

N. Rüther and N. R. B. Olsen. Three-dimensional modeling of sediment transport in a narrow 90° channel bend. *Journal of Hydraulic Engineering*, 131(10):917–920, 2005.

Y. Saad. *Iterative methods for sparse linear systems*. Society for Industrial and Applied Mathematics, Philadelphia, PA, USA, 2003.

Y. Saad and M. H. Schultz. GMRES: A generalized minimal residual algorithm for

solving nonsymmetric linear systems. *SIAM Journal on Scientific and Statistical Computing*, 7(3):856–869, 1986.

P. Sagaut. *Large Eddy Simulation for Incompressible Flows*. Springer, Berlin, 1988.

J. C. Schmidt. Changes in alluvial deposits, upper grand canyon. In *Proceedings of the Fourth Federal Interagency Sedimentation Conference: Water Resources Council*, pages 2–48 to 2–57, 1986.

J. C. Schmidt. Recirculating flow and sedimentation in the Colorado River in Grand Canyon, Arizona. *The Journal of Geology*, 98(5):709–724, 1990.

S. K. Sinha, F. Sotiropoulos, and A. J. Odgaard. Three-dimensional numerical model for flow through natural rivers. *Journal of Hydraulic Engineering*, 124(1):13–24, 1998.

J. S. Smagorinsky. General circulation experiments with the primitive equations. *Monthly Weather Review*, 91:99–164, 1963.

F. Sotiropoulos and V. C. Patel. Prediction of turbulent flow through a transition duct using a second-moment closure. *AIAA Journal*, 32(11):2194–2204, 1994.

F. Sotiropoulos and Y. Ventikos. Flow through a curved duct using nonlinear two-equation turbulence models. *AIAA Journal*, 36(7):1256–1262, 1998.

F. Sotiropoulos, A. Lightbody, and P. Diplas. Development of design methods for in-stream flow control structures. Technical Report Project No. 24-33 interim report, The National Cooperative Highway Research Program, 2009.

P. R. Spalart. Trends in turbulence treatments. *AIAA Paper 2000-2306*, 2000.

P. R. Spalart, W.-H. Jou, M. Strelets, and S. R. Allmaras. Comments on the feasibility of les for wings, and on a hybrid RANS/LES approach. In *Advances in DNS/LES, edited by C. Liu and Z. Liu (Greyden, Columbus, OH, 1997)*, August 1997.

H. D. Sterck, U. M. Yang, and J. J. Heys. Reducing complexity in parallel algebraic multigrid preconditioners. *SIAM Journal on Matrix Analysis and Applications*, 27 (4):1019–1039, 2006.

T. Stoesser, N. Ruether, and N. R. B. Olsen. Calculation of primary and secondary flow and boundary shear stresses in a meandering channel. *Advances in Water Resources*, 33(2):158 – 170, 2010.

M. Sussman and E. Fatemi. An efficient, interface-preserving level set redistancing algorithm and its application to interfacial incompressible fluid flow. *SIAM Journal on Scientific Computing*, 20(4):1165–1191, 1999.

M. Sussman, P. Smereka, and S. Osher. A level set approach for computing solutions to incompressible two-phase flow. *Journal of Computational Physics*, 114(1):146 – 159, 1994.

M. Sussman, E. Fatemi, P. Smereka, and S. Osher. An improved level set method for incompressible two-phase flows. *Computers Fluids*, 27(5-6):663 – 680, 1998.

H. S. Tang, S. C. Jones, and F. Sotiropoulos. An overset-grid method for 3D unsteady incompressible flows. *Journal of Computational Physics*, 191(2):567 – 600, 2003.

T. G. Thomas and J. J. R. Williams. Large eddy simulation of turbulent flow in an asymmetric compound open channel. *Journal of Hydraulic Research*, 33:27–41, 1995.

A. Thompson. Secondary flows and the pool-riffle unit: A case study of the processes of meander development. *Earth Surface Processes and Landforms*, 11(6):631–641, 1986.

J. Thomson. On the origin of windings of rivers in alluvial plains, with remarks on the flow of water round bends in pipes. *Proceedings of the Royal Society of London*, 25: 5–8, 1876.

C. R. Thorne, L. W. Zevenbergen, J. C. Pitlick, S. Rais, J. B. Bradley, and P. Y. Julien. Direct measurements of secondary currents in a meandering sand-bed river. *Nature*, 315:746–747, 1985.

M. Tobak and D. J. Peake. Topology of three-dimensional separated flows. *Annual Review of Fluid Mechanics*, 14(1):61–85, 1982.

A. Tominaga, I. Nezu, K. Ezaki, and H. Nakagawa. Three-dimensional turbulent structure in straight open channel flows. *Journal of Hydraulic Research*, 27:149–173, 1989.

G. Tryggvason, B. Bunner, A. Esmaeeli, D. Juric, N. Al-Rawahi, W. Tauber, J. Han, S. Nas, and Y. J. Jan. A front-tracking method for the computations of multiphase flow. *Journal of Computational Physics*, 169(2):708 – 759, 2001.

S. O. Unverdi and G. Tryggvason. A front-tracking method for viscous, incompressible, multi-fluid flows. *Journal of Computational Physics*, 100(1):25 – 37, 1992.

V. A. Vanoni. *Sedimentation engineering*. American Society of Civil Engineers, New York, 1975.

M. Wang and P. Moin. Dynamic wall modeling for large-eddy simulation of complex turbulent flows. *Physics of Fluids*, 14(7):2043–2051, 2002.

D. C. Wilcox. Reassessment of the scale-determining equation for advanced turbulence models. *AIAA Journal*, 26:1299–1310, 1988.

D. C. Wilcox. *Turbulence Modeling for CFD*. La Cañada, CA: DCW Industries, 1993.

C. A. M. E. Wilson, J. B. Boxall, I. Guymer, and N. R. B. Olsen. Validation of a three-dimensional numerical code in the simulation of pseudo-natural meandering flows. *Journal of Hydraulic Engineering*, 129(10):758–768, 2003.

P. R. Wormleaton and M. Ewunetu. Three-dimensional $k - \epsilon$ numerical modelling of overbank flow in a mobile bed meandering channel with floodplains of different depth, roughness and planform. *Journal of Hydraulic Research*, 44:18–32, 2006.

G. X. Wu and R. Eatock Taylor. Finite element analysis of two-dimensional non-linear transient water waves. *Applied Ocean Research*, 16(6):363 – 372, 1994.

W. Wu, W. Rodi, and T. Wenka. 3d numerical modeling of flow and sediment transport in open channels. *Journal of Hydraulic Engineering*, 126(1):4–15, 2000.

J. Y. Yoon and V. C. Patel. Numerical model of turbulent flow over sand dune. *Journal of Hydraulic Engineering*, 122(1):10–18, 1996.

D. L. Youngs. Time-dependent multi-material flow with large fluid distortion, Numerical methods for fluid dynamics, K. W. Morton and M. J. Bianes (Eds.), Academic Press, New York . 1982.

W. Yue, C.-L. Lin, and V. C. Patel. Numerical simulation of unsteady multidimensional free surface motions by level set method. *International Journal for Numerical Methods in Fluids*, 42(8):853–884, 2003.

W. Yue, C.-L. Lin, and V. C. Patel. Large eddy simulation of turbulent open-channel flow with free surface simulated by level set method. *Physics of Fluids*, 17(2):025108, 2005a.

W. Yue, C.-L. Lin, and V. C. Patel. Coherent structures in open-channel flows over a fixed dune. *Journal of Fluids Engineering*, 127(5):858–864, 2005b.

Y. Zang, R. L. Street, and J. R. Koseff. A non-staggered grid, fractional step method for time-dependent incompressible Navier-Stokes equations in curvilinear coordinates. *Journal of Computational Physics*, 114(1):18–33, 1994.

E. A. Zedler and R. L. Street. Large-eddy simulation of sediment transport: Currents over ripples. *Journal of Hydraulic Engineering*, 127(6):444–452, 2001.

J. Zeng, G. Constantinescu, K. Blanckaert, and L. Weber. Flow and bathymetry in sharp open-channel bends: Experiments and predictions. *Water Resources Research*, 44(9):W09401, 2008.

X. Zhang, D. Schmidt, and B. Perot. Accuracy and conservation properties of a three-dimensional unstructured staggered mesh scheme for fluid dynamics. *Journal of Computational Physics*, 175(2):764–791, 2002.

Appendix A – Transformation and discretization of Navier-Stokes equations

A.1 Transformation of Navier-Stokes equations

Navier-Stokes equations in the Cartesian coordinates $\{x_i\}$ (Eqs. (2.1) and (2.2)) are transformed into curvilinear coordinates $\{\xi_i\}$ typically by means of a generalized curvilinear coordinate transformation defined as:

$$\xi_i = \xi_i(x_1, x_2, x_3) \qquad (i = 1, 2, 3). \tag{A.1}$$

By using the chain rule the derivatives in Cartesian coordinates are transformed into curvilinear coordinates as follows:

$$\frac{\partial}{\partial x_j} = \xi_j^i \frac{\partial}{\partial \xi_i} = \xi_j^1 \frac{\partial}{\partial \xi_1} + \xi_j^2 \frac{\partial}{\partial \xi_2} + \xi_j^3 \frac{\partial}{\partial \xi_3}, \tag{A.2}$$

where $\xi_j^i = \partial \xi_i / \partial x_j$ are the transformation metrics.

There are two choices, however, to employ the transformation: the partial transformation and the full transformation. In the full transformation all the variables (dependent and independent) are transformed into the curvilinear coordinates. In contrast, in partial transformation only the independent variables x_i are transformed into curvilinear coordinates, while the dependent variables, the velocity vector components u_i, are retained in the Cartesian coordinates. With partial transformation the Christoffel symbols, which are found in the full transformation, are avoided (Ge and Sotiropoulos, 2007). The partially transformed equations read in compact tensor notation (repeated indices imply summation) as follows

$$J\frac{\partial U_j}{\partial \xi_j} = 0, \tag{A.3}$$

$$\begin{aligned}\frac{1}{J}\frac{\partial U_i}{\partial t} = \frac{\xi_l^i}{J}\left(-\frac{\partial}{\partial \xi_j}(U_j u_l) + \frac{1}{\rho}\frac{\partial}{\partial \xi_j}(\mu\frac{g^{jk}}{J}\frac{\partial u_l}{\partial \xi_k}) - \frac{1}{\rho}\frac{\partial \tau_{lj}}{\partial \xi_j} + \frac{1}{\rho}G_l + \frac{1}{\rho}H_l\right) \\ - \frac{1}{\rho}\frac{\xi_l^i}{J}\frac{\partial}{\partial \xi_j}(\frac{\xi_l^j p}{J}),\end{aligned} \tag{A.4}$$

where p is the pressure, ρ is the density, μ is the dynamic viscosity, τ_{ij} is the subgrid stress of LES models or Reynolds stress of RANS models, and G_i and H_i are the external stresses due to the gravity and the surface tension, respectively, J is the Jacobian of the geometric transformation $J = \partial(\xi_1, \xi_2, \xi_3)/\partial(x_1, x_2, x_3)$, u_i is the i^{th} Cartesian velocity component, $U_i{=}(\xi_m^i/J)u_m$ is the contravariant volume flux, and $g^{jk} = \xi_l^j \xi_l^k$ are the components of the contravariant metric tensor.

A.2 Discretization of momentum equations

The hybrid staggered/non-staggered approach of Gilmanov and Sotiropoulos Gilmanov and Sotiropoulos (2005) and Ge and Sotiropoulos Ge and Sotiropoulos (2007) have been adopted to discretize the Navier-Stokes equations. Using this approach with partial transformation in the curvilinear coordinate enables satisfying the discrete continuity equation similar to the full transformation but without the need to calculate Christoffel symbols. The contravariant volume fluxes U_i are stored at the respective surface centers while the pressure is stored at the volume centers.

The convection term in the equation for the first component of contravariant volume flux (U_1) are discretized as

$$\frac{\xi_l^1}{J}\frac{\partial}{\partial\xi_j}(U_j u_l)\bigg|_{i+\frac{1}{2},j,k} = \frac{\xi_l^1}{J}\left(\frac{\partial}{\partial\xi_1}(U_1u_l)+\frac{\partial}{\partial\xi_2}(U_2u_l)+\frac{\partial}{\partial\xi_3}(U_3u_l)\right)\bigg|_{i+\frac{1}{2},j,k}, \tag{A.5}$$

where

$$\frac{\partial}{\partial\xi_1}(U_1u_l)\bigg|_{i+\frac{1}{2},j,k} = \frac{1}{2}\,\frac{\partial}{\partial\xi_1}(U_1u_l)\bigg|_{i,j,k} + \frac{1}{2}\,\frac{\partial}{\partial\xi_1}(U_1u_l)\bigg|_{i+1,j,k}, \tag{A.6}$$

$$\frac{\partial}{\partial\xi_2}(U_2u_l)\bigg|_{i+\frac{1}{2},j,k} = \frac{1}{2}\,\frac{\partial}{\partial\xi_2}(U_2u_l)\bigg|_{i,j,k} + \frac{1}{2}\,\frac{\partial}{\partial\xi_2}(U_2u_l)\bigg|_{i+1,j,k}, \tag{A.7}$$

$$\frac{\partial}{\partial\xi_3}(U_3u_l)\bigg|_{i+\frac{1}{2},j,k} = \frac{1}{2}\,\frac{\partial}{\partial\xi_3}(U_3u_l)\bigg|_{i,j,k} + \frac{1}{2}\,\frac{\partial}{\partial\xi_3}(U_3u_l)\bigg|_{i+1,j,k}, \tag{A.8}$$

with

$$\begin{aligned}\frac{\partial}{\partial\xi_1}(U_1u_l)\bigg|_{i,j,k} &= \frac{(U_1u_l)_{i+\frac{1}{2},j,k}-(U_1u_l)_{i-\frac{1}{2},j,k}}{\Delta\xi_1}\\ &= (U_1)_{i+\frac{1}{2},j,k}\,\frac{(u_l)_{i+1,j,k}+(u_l)_{i,j,k}}{2\Delta\xi_1} - (U_1)_{i-\frac{1}{2},j,k}\,\frac{(u_l)_{i,j,k}+(u_l)_{i-1,j,k}}{2\Delta\xi_1},\end{aligned} \tag{A.9}$$

$$\left.\frac{\partial}{\partial\xi_2}(U_2u_l)\right|_{i,j,k} = (U_2)_{i+\frac{1}{2},j,k}\,\frac{(u_l)_{i+1,j,k}+(u_l)_{i,j,k}}{2\Delta\xi_2} - (U_2)_{i-\frac{1}{2},j,k}\,\frac{(u_l)_{i,j,k}+(u_l)_{i-1,j,k}}{2\Delta\xi_2}, \tag{A.10}$$

$$\left.\frac{\partial}{\partial\xi_3}(U_3u_l)\right|_{i,j,k} = (U_3)_{i+\frac{1}{2},j,k}\,\frac{(u_l)_{i+1,j,k}+(u_l)_{i,j,k}}{2\Delta\xi_3} - (U_3)_{i-\frac{1}{2},j,k}\,\frac{(u_l)_{i,j,k}+(u_l)_{i-1,j,k}}{2\Delta\xi_3}. \tag{A.11}$$

The discretization of convection terms in the equations for two other components can be done in the same way as shown above. Central differencing is employed above, however, other differencing schemes, such as QUICK scheme (see Ge and Sotiropoulos (2007)), can readily be employed to discretize the convection terms.

The diffusion term in the equation for the first component of contravariant volume flux (U_1) are discretized with the central differencing as

$$\begin{aligned}&\frac{1}{\rho}\frac{\xi_l^1}{J}\frac{\partial}{\partial\xi_j}(\mu\frac{g^{jm}}{J}\frac{\partial u_l}{\partial\xi_m})\Big|_{i+\frac{1}{2},j,k}\\ &= \frac{1}{\rho}\frac{\xi_l^1}{J}\left(\frac{\partial}{\partial\xi_1}(\mu\frac{g^{1m}}{J}\frac{\partial u_l}{\partial\xi_m}) + \frac{\partial}{\partial\xi_2}(\mu\frac{g^{2m}}{J}\frac{\partial u_l}{\partial\xi_m}) + \frac{\partial}{\partial\xi_3}(\mu\frac{g^{3m}}{J}\frac{\partial u_l}{\partial\xi_m})\right)\Big|_{i+\frac{1}{2},j,k}\end{aligned} \tag{A.12}$$

where

$$\left.\frac{\partial}{\partial\xi_1}(\mu\frac{g^{1m}}{J}\frac{\partial u_l}{\partial\xi_m})\right|_{i+\frac{1}{2},j,k} = \frac{1}{2}\frac{\partial}{\partial\xi_1}(\mu\frac{g^{1m}}{J}\frac{\partial u_l}{\partial\xi_m})\Big|_{i+1,j,k} + \frac{1}{2}\frac{\partial}{\partial\xi_1}(\mu\frac{g^{1m}}{J}\frac{\partial u_l}{\partial\xi_m})\Big|_{i,j,k}, \tag{A.13}$$

$$\left.\frac{\partial}{\partial\xi_2}(\mu\frac{g^{2m}}{J}\frac{\partial u_l}{\partial\xi_m})\right|_{i+\frac{1}{2},j,k} = \frac{1}{2}\frac{\partial}{\partial\xi_2}(\mu\frac{g^{2m}}{J}\frac{\partial u_l}{\partial\xi_m})\Big|_{i+1,j,k} + \frac{1}{2}\frac{\partial}{\partial\xi_2}(\mu\frac{g^{2m}}{J}\frac{\partial u_l}{\partial\xi_m})\Big|_{i,j,k}, \tag{A.14}$$

$$\left.\frac{\partial}{\partial\xi_3}(\mu\frac{g^{3m}}{J}\frac{\partial u_l}{\partial\xi_m})\right|_{i+\frac{1}{2},j,k} = \frac{1}{2}\frac{\partial}{\partial\xi_3}(\mu\frac{g^{3m}}{J}\frac{\partial u_l}{\partial\xi_m})\Big|_{i+1,j,k} + \frac{1}{2}\frac{\partial}{\partial\xi_3}(\mu\frac{g^{3m}}{J}\frac{\partial u_l}{\partial\xi_m})\Big|_{i,j,k}, \tag{A.15}$$

and

$$\frac{\partial}{\partial\xi_1}(\mu\frac{g^{1m}}{J}\frac{\partial u_l}{\partial\xi_m})\bigg|_{i,j,k} = \frac{\partial}{\partial\xi_1}\left(\mu\frac{g^{11}}{J}\frac{\partial u_l}{\partial\xi_1}+\mu\frac{g^{12}}{J}\frac{\partial u_l}{\partial\xi_2}+\mu\frac{g^{13}}{J}\frac{\partial u_l}{\partial\xi_3}\right)\bigg|_{i,j,k}, \tag{A.16}$$

$$\frac{\partial}{\partial\xi_2}(\mu\frac{g^{2m}}{J}\frac{\partial u_l}{\partial\xi_m})\bigg|_{i,j,k} = \frac{\partial}{\partial\xi_2}\left(\mu\frac{g^{21}}{J}\frac{\partial u_l}{\partial\xi_1}+\mu\frac{g^{22}}{J}\frac{\partial u_l}{\partial\xi_2}+\mu\frac{g^{23}}{J}\frac{\partial u_l}{\partial\xi_3}\right)\bigg|_{i,j,k}, \tag{A.17}$$

$$\frac{\partial}{\partial\xi_3}(\mu\frac{g^{3m}}{J}\frac{\partial u_l}{\partial\xi_m})\bigg|_{i,j,k} = \frac{\partial}{\partial\xi_3}\left(\mu\frac{g^{31}}{J}\frac{\partial u_l}{\partial\xi_1}+\mu\frac{g^{32}}{J}\frac{\partial u_l}{\partial\xi_2}+\mu\frac{g^{33}}{J}\frac{\partial u_l}{\partial\xi_3}\right)\bigg|_{i,j,k}. \tag{A.18}$$

Three terms in the right hand side of Eq. (A.16) are discretized as

$$\frac{\partial}{\partial\xi_1}(\mu\frac{g^{11}}{J}\frac{\partial u_l}{\partial\xi_1})\bigg|_{i,j,k} = \frac{\left(\mu\frac{g^{11}}{J}\frac{\partial u_l}{\partial\xi_1}\right)_{i+\frac{1}{2},j,k}-\left(\mu\frac{g^{11}}{J}\frac{\partial u_l}{\partial\xi_1}\right)_{i-\frac{1}{2},j,k}}{\Delta\xi_1}, \tag{A.19}$$

$$\frac{\partial}{\partial\xi_1}(\mu\frac{g^{12}}{J}\frac{\partial u_l}{\partial\xi_2})\bigg|_{i,j,k} = \frac{\left(\mu\frac{g^{12}}{J}\frac{\partial u_l}{\partial\xi_2}\right)_{i+\frac{1}{2},j,k}-\left(\mu\frac{g^{12}}{J}\frac{\partial u_l}{\partial\xi_2}\right)_{i-\frac{1}{2},j,k}}{\Delta\xi_1}, \tag{A.20}$$

$$\frac{\partial}{\partial\xi_1}(\mu\frac{g^{13}}{J}\frac{\partial u_l}{\partial\xi_3})\bigg|_{i,j,k} = \frac{\left(\mu\frac{g^{13}}{J}\frac{\partial u_l}{\partial\xi_3}\right)_{i+\frac{1}{2},j,k}-\left(\mu\frac{g^{13}}{J}\frac{\partial u_l}{\partial\xi_3}\right)_{i-\frac{1}{2},j,k}}{\Delta\xi_1}. \tag{A.21}$$

with

$$\left(\frac{\partial u_l}{\partial\xi_1}\right)_{i+\frac{1}{2},j,k} = \frac{(u_l)_{i+1,j,k}-(u_l)_{i,j,k}}{\Delta\xi_1}, \tag{A.22}$$

$$\left(\frac{\partial u_l}{\partial\xi_2}\right)_{i+\frac{1}{2},j,k} = \frac{(u_l)_{i+1,j+1,k}+(u_l)_{i,j+1,k}-(u_l)_{i+1,j,k}-(u_l)_{i,j,k}}{4\Delta\xi_2}, \tag{A.23}$$

$$\left(\frac{\partial u_l}{\partial\xi_3}\right)_{i+\frac{1}{2},j,k} = \frac{(u_l)_{i+1,j,k+1}+(u_l)_{i,j,k+1}-(u_l)_{i+1,j,k}-(u_l)_{i,j,k}}{4\Delta\xi_3}. \tag{A.24}$$

Eqs. (A.17) and (A.18) can be discretized in a similar manner. The discretization of diffusion terms in the equations for two other components can be done in the same way as shown above.

The pressure gradient terms in the equation for the three components of contravariant volume flux (U_1, U_2, U_3) are discretized with the central differencing as

$$\left.\frac{\xi_l^1}{J}\frac{\partial}{\partial\xi_j}(\frac{\xi_l^j p}{J})\right|_{i+\frac{1}{2},j,k} = \left.\left(g^{11}\frac{\partial p}{\partial\xi_1} + g^{12}\frac{\partial p}{\partial\xi_2} + g^{13}\frac{\partial p}{\partial\xi_3}\right)\right|_{i+\frac{1}{2},j,k}, \tag{A.25}$$

$$\left.\frac{\xi_l^2}{J}\frac{\partial}{\partial\xi_j}(\frac{\xi_l^j p}{J})\right|_{i,j+\frac{1}{2},k} = \left.\left(g^{21}\frac{\partial p}{\partial\xi_1} + g^{22}\frac{\partial p}{\partial\xi_2} + g^{23}\frac{\partial p}{\partial\xi_3}\right)\right|_{i,j+\frac{1}{2},k}, \tag{A.26}$$

$$\left.\frac{\xi_l^3}{J}\frac{\partial}{\partial\xi_j}(\frac{\xi_l^j p}{J})\right|_{i,j,k+\frac{1}{2}} = \left.\left(g^{31}\frac{\partial p}{\partial\xi_1} + g^{32}\frac{\partial p}{\partial\xi_2} + g^{33}\frac{\partial p}{\partial\xi_3}\right)\right|_{i,j,k+\frac{1}{2}}, \tag{A.27}$$

with

$$\left(\frac{\partial p}{\partial\xi_1}\right)_{i+\frac{1}{2},j,k} = \frac{p_{i+1,j,k} - p_{i,j,k}}{\Delta\xi_1}, \tag{A.28}$$

$$\left(\frac{\partial p}{\partial\xi_2}\right)_{i+\frac{1}{2},j,k} = \frac{p_{i+1,j+1,k} + p_{i,j+1,k} - p_{i+1,j,k} - p_{i,j,k}}{4\Delta\xi_2}, \tag{A.29}$$

$$\left(\frac{\partial p}{\partial\xi_3}\right)_{i+\frac{1}{2},j,k} = \frac{p_{i+1,j,k+1} + p_{i,j,k+1} - p_{i+1,j,k} - p_{i,j,k}}{4\Delta\xi_3}, \tag{A.30}$$

$$\left(\frac{\partial p}{\partial\xi_1}\right)_{i,j+\frac{1}{2},k} = \frac{p_{i+1,j+1,k} + p_{i+1,j,k} - p_{i,j+1,k} - p_{i,j,k}}{4\Delta\xi_1}, \tag{A.31}$$

$$\left(\frac{\partial p}{\partial\xi_2}\right)_{i,j+\frac{1}{2},k} = \frac{p_{i,j+1,k} - p_{i,j,k}}{\Delta\xi_2}, \tag{A.32}$$

$$\left(\frac{\partial p}{\partial\xi_3}\right)_{i,j+\frac{1}{2},k} = \frac{p_{i,j+1,k+1} + p_{i,j,k+1} - p_{i,j+1,k} - p_{i,j,k}}{4\Delta\xi_3}, \tag{A.33}$$

$$\left(\frac{\partial p}{\partial \xi_1}\right)_{i,j,k+\frac{1}{2}} = \frac{p_{i+1,j,k+1} + p_{i+1,j,k} - p_{i,j,k+1} - p_{i,j,k}}{4\Delta\xi_1}, \tag{A.34}$$

$$\left(\frac{\partial p}{\partial \xi_2}\right)_{i,j,k+\frac{1}{2}} = \frac{p_{i,j+1,k+1} + p_{i,j+1,k} - p_{i,j,k+1} - p_{i,j,k}}{4\Delta\xi_2}, \tag{A.35}$$

$$\left(\frac{\partial p}{\partial \xi_3}\right)_{i,j,k+\frac{1}{2}} = \frac{p_{i,j,k+1} - p_{i,j,k}}{\Delta\xi_3}. \tag{A.36}$$

A.3 Discretization of Poisson equation

The Poisson equation, which results from the fractional step method, in generalized curvilinear coordinates is given as

$$-J\frac{\partial}{\partial\xi_i}\left(\frac{1}{\rho}\frac{\xi_l^i}{J}\frac{\partial}{\partial\xi_j}(\frac{\xi_l^j\Pi}{J})\right)=\frac{3}{2\Delta t}J\frac{\partial U_j^*}{\partial\xi_j}. \tag{A.37}$$

where Π is the pressure increment and U^* is the intermediate contravariant volume flux that does not satisfy continuity (see Section 2.2).

The left hand side of Eq. (A.37) is discretized as

$$\begin{aligned}
& J\frac{\partial}{\partial\xi_m}\left(\frac{1}{\rho}\frac{\xi_l^m}{J}\frac{\partial}{\partial\xi_n}(\frac{\xi_l^n\Pi}{J})\right)\Big|_{i,j,k} \\
= \;& J\frac{\partial}{\partial\xi_m}\left(\frac{1}{\rho}\frac{\xi_l^m}{J}\frac{\xi_l^n}{J}\frac{\partial\Pi}{\partial\xi_n}\right)\Big|_{i,j,k} \\
= \;& J\frac{\partial}{\partial\xi_m}\left(\frac{1}{\rho}g^{mn}\frac{\partial\Pi}{\partial\xi_n}\right)\Big|_{i,j,k} \\
= \;& J\,\frac{\partial}{\partial\xi_1}\left(\frac{1}{\rho}g^{11}\frac{\partial\Pi}{\partial\xi_1}\right)\Big|_{i,j,k}+J\,\frac{\partial}{\partial\xi_1}\left(\frac{1}{\rho}g^{12}\frac{\partial\Pi}{\partial\xi_2}\right)\Big|_{i,j,k}+J\,\frac{\partial}{\partial\xi_1}\left(\frac{1}{\rho}g^{13}\frac{\partial\Pi}{\partial\xi_3}\right)\Big|_{i,j,k} \\
& +J\,\frac{\partial}{\partial\xi_2}\left(\frac{1}{\rho}g^{21}\frac{\partial\Pi}{\partial\xi_1}\right)\Big|_{i,j,k}+J\,\frac{\partial}{\partial\xi_2}\left(\frac{1}{\rho}g^{22}\frac{\partial\Pi}{\partial\xi_2}\right)\Big|_{i,j,k}+J\,\frac{\partial}{\partial\xi_2}\left(\frac{1}{\rho}g^{23}\frac{\partial\Pi}{\partial\xi_3}\right)\Big|_{i,j,k} \\
& +J\,\frac{\partial}{\partial\xi_3}\left(\frac{1}{\rho}g^{31}\frac{\partial\Pi}{\partial\xi_1}\right)\Big|_{i,j,k}+J\,\frac{\partial}{\partial\xi_3}\left(\frac{1}{\rho}g^{32}\frac{\partial\Pi}{\partial\xi_2}\right)\Big|_{i,j,k}+J\,\frac{\partial}{\partial\xi_3}\left(\frac{1}{\rho}g^{33}\frac{\partial\Pi}{\partial\xi_3}\right)\Big|_{i,j,k},
\end{aligned} \tag{A.38}$$

where

$$\frac{\partial}{\partial\xi_1}\left(\frac{1}{\rho}g^{11}\frac{\partial\Pi}{\partial\xi_1}\right)\bigg|_{i,j,k}=\frac{\left(\frac{1}{\rho}g^{11}\frac{\partial\Pi}{\partial\xi_1}\right)_{i+\frac{1}{2},j,k}-\left(\frac{1}{\rho}g^{11}\frac{\partial\Pi}{\partial\xi_1}\right)_{i-\frac{1}{2},j,k}}{\Delta\xi_1}, \tag{A.39}$$

$$\frac{\partial}{\partial\xi_1}\left(\frac{1}{\rho}g^{12}\frac{\partial\Pi}{\partial\xi_2}\right)\bigg|_{i,j,k}=\frac{\left(\frac{1}{\rho}g^{12}\frac{\partial\Pi}{\partial\xi_2}\right)_{i+\frac{1}{2},j,k}-\left(\frac{1}{\rho}g^{12}\frac{\partial\Pi}{\partial\xi_2}\right)_{i-\frac{1}{2},j,k}}{\Delta\xi_1}, \tag{A.40}$$

$$\frac{\partial}{\partial\xi_1}\left(\frac{1}{\rho}g^{13}\frac{\partial\Pi}{\partial\xi_3}\right)\bigg|_{i,j,k}=\frac{\left(\frac{1}{\rho}g^{13}\frac{\partial\Pi}{\partial\xi_3}\right)_{i+\frac{1}{2},j,k}-\left(\frac{1}{\rho}g^{13}\frac{\partial\Pi}{\partial\xi_3}\right)_{i-\frac{1}{2},j,k}}{\Delta\xi_1}, \tag{A.41}$$

with

$$\left(\frac{\partial\Pi}{\partial\xi_1}\right)_{i+\frac{1}{2},j,k}=\frac{\Pi_{i+1,j,k}-\Pi_{i,j,k}}{\Delta\xi_1}, \tag{A.42}$$

$$\left(\frac{\partial\Pi}{\partial\xi_2}\right)_{i+\frac{1}{2},j,k}=\frac{\Pi_{i+1,j+1,k}+\Pi_{i,j+1,k}-\Pi_{i+1,j,k}-\Pi_{i,j,k}}{4\Delta\xi_2}, \tag{A.43}$$

$$\left(\frac{\partial\Pi}{\partial\xi_3}\right)_{i+\frac{1}{2},j,k}=\frac{\Pi_{i+1,j,k+1}+\Pi_{i,j,k+1}-\Pi_{i+1,j,k}-\Pi_{i,j,k}}{4\Delta\xi_3}, \tag{A.44}$$

$$\left(\frac{\partial\Pi}{\partial\xi_1}\right)_{i,j+\frac{1}{2},k}=\frac{\Pi_{i+1,j+1,k}+\Pi_{i+1,j,k}-\Pi_{i,j+1,k}-\Pi_{i,j,k}}{4\Delta\xi_1}, \tag{A.45}$$

$$\left(\frac{\partial\Pi}{\partial\xi_2}\right)_{i,j+\frac{1}{2},k}=\frac{\Pi_{i,j+1,k}-\Pi_{i,j,k}}{\Delta\xi_2}, \tag{A.46}$$

$$\left(\frac{\partial\Pi}{\partial\xi_3}\right)_{i,j+\frac{1}{2},k}=\frac{\Pi_{i,j+1,k+1}+\Pi_{i,j,k+1}-\Pi_{i,j+1,k}-\Pi_{i,j,k}}{4\Delta\xi_3}, \tag{A.47}$$

$$\left(\frac{\partial\Pi}{\partial\xi_1}\right)_{i,j,k+\frac{1}{2}}=\frac{\Pi_{i+1,j,k+1}+\Pi_{i+1,j,k}-\Pi_{i,j,k+1}-\Pi_{i,j,k}}{4\Delta\xi_1}, \tag{A.48}$$

$$\left(\frac{\partial\Pi}{\partial\xi_2}\right)_{i,j,k+\frac{1}{2}}=\frac{\Pi_{i,j+1,k+1}+\Pi_{i,j+1,k}-\Pi_{i,j,k+1}-\Pi_{i,j,k}}{4\Delta\xi_2}, \tag{A.49}$$

$$\left(\frac{\partial\Pi}{\partial\xi_3}\right)_{i,j,k+\frac{1}{2}}=\frac{\Pi_{i,j,k+1}-\Pi_{i,j,k}}{\Delta\xi_3}. \tag{A.50}$$

The density at the cell face is calculated as

$$\left.\frac{1}{\rho}\right|_{i+\frac{1}{2},j,k} = \frac{1}{2}\left(\left.\frac{1}{\rho}\right|_{i+1,j,k} + \left.\frac{1}{\rho}\right|_{i,j,k}\right), \tag{A.51}$$

$$\left.\frac{1}{\rho}\right|_{i,j+\frac{1}{2},k} = \frac{1}{2}\left(\left.\frac{1}{\rho}\right|_{i,j+1,k} + \left.\frac{1}{\rho}\right|_{i,j,k}\right), \tag{A.52}$$

$$\left.\frac{1}{\rho}\right|_{i,j,k+\frac{1}{2}} = \frac{1}{2}\left(\left.\frac{1}{\rho}\right|_{i,j,k+1} + \left.\frac{1}{\rho}\right|_{i,j,k}\right). \tag{A.53}$$

The right hand side of Eq. (A.37) is discretized as

$$\left.\frac{\partial U_m^*}{\partial \xi_m}\right|_{i,j,k} = \frac{U_1^*|_{i+\frac{1}{2},j,k} - U_1^*|_{i-\frac{1}{2},j,k}}{\Delta\xi_1} + \frac{U_2^*|_{i,j+\frac{1}{2},k} - U_2^*|_{i,j-\frac{1}{2},k}}{\Delta\xi_2} + \frac{U_3^*|_{i,j,k+\frac{1}{2}} - U_3^*|_{i,j,k-\frac{1}{2}}}{\Delta\xi_3}. \tag{A.54}$$

Appendix B – Test filtering for large-eddy simulation

In this appendix, the test filtering procedure employed by the present numerical code is presented. The dynamic Smagorinsky model (Germano et al., 1991) for large-eddy simulation requires the filtering of solution variables (velocities) over the test filter which is larger than the grid filter. Figure B.1 shows the schematic description of the test filtering volume in two dimensions. The test filter is set to span two grid cells in each direction. In other words, the test filtering volume is composed of the volume of the grid filter itself and parts of the volume of 8 (26 in three dimensions) surrounding grid cells. For instance, the test filtered value of the variable ϕ at the cell (i, j) is given as

$$\hat{\phi} = \frac{\omega_{i-\frac{1}{2},j-\frac{1}{2}}\phi_{i-\frac{1}{2},j-\frac{1}{2}} + \omega_{i+\frac{1}{2},j-\frac{1}{2}}\phi_{i+\frac{1}{2},j-\frac{1}{2}} + \omega_{i-\frac{1}{2},j+\frac{1}{2}}\phi_{i-\frac{1}{2},j+\frac{1}{2}} + \omega_{i+\frac{1}{2},j+\frac{1}{2}}\phi_{i+\frac{1}{2},j+\frac{1}{2}}}{\omega_{i-\frac{1}{2},j-\frac{1}{2}} + \omega_{i+\frac{1}{2},j-\frac{1}{2}} + \omega_{i-\frac{1}{2},j+\frac{1}{2}} + \omega_{i+\frac{1}{2},j+\frac{1}{2}}}, \tag{B.1}$$

where ω is the weighting factor, and the subscripts $i \pm \frac{1}{2}, j \pm \frac{1}{2}$ denote locations at the four (eight in three dimensions) corners around the cell (i, j) (filled squares in Figure B.1). For instance, ϕ at the top right corner is computed by

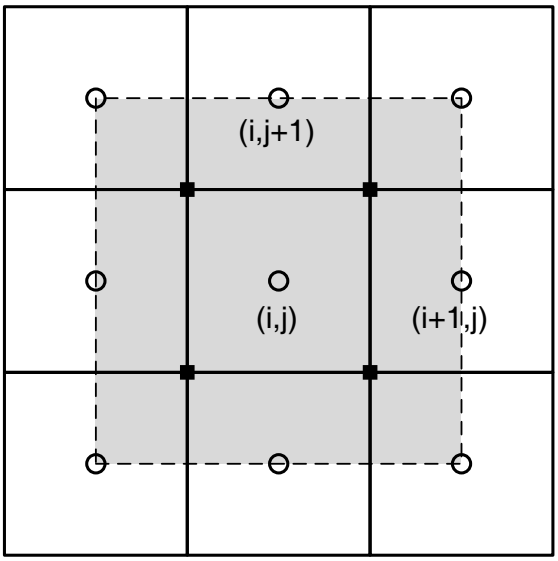

Figure B.1: Schematic description of the test filtering volume (shaded area with dashed lines) in two dimensions.

$$\phi_{i+\frac{1}{2},j+\frac{1}{2}} = \frac{A_{i,j}\phi_{i,j} + A_{i+1,j}\phi_{i+1,j} + A_{i,j+1}\phi_{i,j+1} + A_{i+1,j+1}\phi_{i+1,j+1}}{A_{i,j} + A_{i+1,j} + A_{i,j+1} + A_{i+1,j+1},} \tag{B.2}$$

$$\omega_{i+\frac{1}{2},j+\frac{1}{2}} = A_{i,j} + A_{i+1,j} + A_{i,j+1} + A_{i+1,j+1}, \tag{B.3}$$

where $A_{i,j}$ denotes the shaded portion of the area (or the volume in three dimensions) of the grid cell (i, j).

Extension of the above mentioned procedure to the three dimensions is straightforward.

Appendix C – Free-surface modeling

There are broadly three ways to numerically handle the free-surface motion: 1) the arbitrary Lagrangian-Eulerian (ALE) method; 2) the front tracking method; and 3) the front capturing method.

In the ALE method one of the boundaries of the computational domain is fitted to and continuously moves to track the location of the free-surface. Consequently the computational grid is being deformed and re-meshing is required. The underlying assumption in the ALE method is that the interface should be kept connected each other, and the grid deformation should be small. Hence, violent free-surface motions such as wave breaking or splashing free-surface cannot be modeled. Ramaswamy and Kawahara (1987) used the ALE approach to solve the two-dimensional sloshing problem on triangular meshes and Hodges and Street (1999) solved three-dimensional turbulent flow in an open channel with a finite-amplitude surface wave on a boundary-orthogonal curvilinear grid. The work of Hodges and Street (1999) showed the possibility of applying the ALE method for solving the three-dimensional turbulent free-surface flow simulation.

The front tracking method was first introduced by Unverdi and Tryggvason (1992). In this method a closed curve (or a closed triangular surface mesh for three-dimensional problems) is generated to represent the interface between two immiscible fluids. The

curve (or the surface mesh) is immersed in the background computational domain and moves at every time step to track the interface. The advantage of the front tracking method is that the location and the shape of the interface are captured more accurately than those of Eulerian methods, such as front-capturing methods. However, this method is computationally more expensive than Eulerian methods because the computational cost for re-meshing of the surface mesh in three-dimensional problems is not trivial.

Front tracking methods have been applied to a large range of multiphase flow problems. A recent review of the method is found in Tryggvason et al. (2001). In the front capturing methods, the position of the interface is captured by the scalar marker function. In these methods no assumption is made about the connectivity of the interface and therefore topologically complex liquid/gas transitions can be modeled in a straightforward manner. Two important methods in this category are the volume-of-fluid (VOF) method of Hirt and Nichols (1981) and the level-set method of Osher and Sethian (1988). In the VOF method, the value of the marker function is one in the liquid phase and zero in the gas phase, respectively, and only the liquid phase is solved numerically. At each time step, the interface is reconstructed using the values of the marker function of the neighboring cells to prevent the non-physical behavior of the interface (Youngs, 1982). Special care is necessary to prevent numerical instabilities when advecting the marker function, which could arise because the function is discontinuous across the interface. Chen et al. (2002) solved the two-dimensional RANS equations over a stepped spillway using the VOF method and predicted correctly the water surface and the pressure profile. Lin and Liu (1998) also used a RANS model to simulate two-dimensional breaking of waves in the surf zone with the VOF method. Their results were in reasonable agreement with measured water surface, velocity, and turbulent kinetic energy. Even though VOF-type methods have been successful in solving two-dimensional problems, their extension to three-dimensional problems, especially with

generalized curvilinear grids, is not straightforward. This is because the reconstruction of the interface in a three-dimensional curvilinear mesh is extremely complicated. In the level-set method, on the other hand, the value of the marker function is the distance from the interface, which is zero at the interface, positive in the liquid phase, and negative in the gas phase. Yue et al. (2003) solved two-dimensional and three-dimensional dam break problems with the level-set method and could capture complex free-surface patterns such as air entrainment in the water and air splashing of the water surge front. Yue et al. (2005a) studied turbulent open-channel flow over a two-dimensional laboratory-scale dune using large-eddy simulation.

The major differences between VOF and level-set methods are as follows.

- While the thickness of the interface is one grid cell in VOF methods, the thickness of the interface in level-set methods is usually greater. This feature makes the transition of the level-set function across the interface smoother and improves the accuracy of the spatial discretization of the terms for the curvature of the interface, which are used for calculating the surface tension terms.

- The marker function is continuous across the interface in level-set methods, which prevents numerical oscillations due to the presence of discontinuity.

- No reconstruction of the interface is required in the level-set methods and as such these methods are straightforward to extend to three-dimensional problems.

Because of these advantages of the level-set approach relative to the VOF method, and since our emphasis is on simulating three-dimensional flows in curvilinear grids, we develop a level-set framework for simulating the free-surface deformation. In what follows we present the numerical method, present validation studies for simple flow and apply it to simulate the flow in the OSL.

C.1 Governing equations

The filtered/averaged Navier-Stokes equations for two immiscible and incompressible fluids read in Cartesian coordinates and in tensor notation (where repeated indices imply summation) as follows ($i, j = 1, 2, 3$):

$$\frac{\partial u_j}{\partial x_j} = 0, \tag{C.1}$$

$$\frac{\partial u_i}{\partial t} + u_j \frac{\partial u_i}{\partial x_j} = -\frac{1}{\rho}\frac{\partial p}{\partial x_i} + \frac{1}{\rho}\frac{\partial}{\partial x_j}\left(\mu \frac{\partial u_i}{\partial x_j}\right) - \frac{1}{\rho}\frac{\partial \tau_{ij}}{\partial x_j} + \frac{1}{\rho}G_i + \frac{1}{\rho}H_i, \tag{C.2}$$

where u_i is the velocity vector, p is the pressure, ρ is the density, μ is the dynamic viscosity, τ_{ij} is the subgrid stress tensor of LES models or Reynolds stress tensor for RANS models, and G_i and H_i are the external forces due to the gravity and the surface tension, respectively.

In the level-set method, the interface between two fluids is captured by the level-set function. The value of the level-set function denotes the distance from the interface, and it is positive in the liquid region, negative in the gas region, and zero at the interface. The level-set function is advected by the following Hamilton-Jacobi equation

$$\frac{D\phi}{Dt} = \frac{\partial \phi}{\partial t} + u_j \frac{\partial \phi}{\partial x_j} = 0, \tag{C.3}$$

where ϕ is the level-set function. The density and viscosity in Navier-Stokes equations are given by

$$\rho(\phi) = \rho_g + (\rho_l - \rho_g)h(\phi), \tag{C.4}$$

$$\mu(\phi) = \mu_g + (\mu_l - \mu_g)h(\phi), \tag{C.5}$$

where the subscripts g and l denote the phase of gas and liquid and h is the Heaviside function.

C.2 Two-phase level-set method

The values of the density and dynamic viscosity are stored at the center of the cell. However, when solving Eqs. (2.4) and (2.34), we need to know their values at the cell face. The following interpolation is used to get values of the density and dynamic viscosity at the cell face which is located between (i, j, k) and $(i + 1, j, k)$

$$\rho_{i+\frac{1}{2}} = \frac{2\rho_{i,j,k}\rho_{i+1,j,k}}{\rho_{i,j,k} + \rho_{i+1,j,k}}, \tag{C.6}$$

$$\mu_{i+\frac{1}{2},j,k} = \frac{1}{2}\left(\mu_{i,j,k} + \mu_{i+1,j,k}\right), \tag{C.7}$$

and values in other directions are calculated in the same way.

h in Eqs. (C.4) and (C.5) is the smoothed Heaviside function given by (Osher and Fedkiw, 2002)

$$h(\phi) = \begin{cases} 0 & \phi < -\epsilon, \\ \frac{1}{2} + \frac{\phi}{2\epsilon} + \frac{1}{2\pi}\sin\left(\frac{\pi\phi}{\epsilon}\right) & -\epsilon \le \phi \le \epsilon, \\ 1 & \epsilon < \phi, \end{cases} \tag{C.8}$$

where ϵ is a tunable parameter that determines the size of the bandwidth numerical smearing (Osher and Fedkiw, 2002). The value of ϵ is usually between one and two grid spacings. Smoothed interface renders the density, velocity and pressure continuous across the interface, and it prevents numerical instability from occurring. Then the delta function is defined as the derivative of the Heaviside function

$$\delta(\phi) = \begin{cases} 0 & \phi < -\epsilon, \\ \frac{1}{2\epsilon} + \frac{1}{2\epsilon}\cos\left(\frac{\pi\phi}{\epsilon}\right) & -\epsilon \le \phi \le \epsilon, \\ 0 & \epsilon < \phi. \end{cases} \tag{C.9}$$

The delta function is used in Eq. (C.12).

While Eq. (C.3) accurately moves the zero level-set according to the given velocity field (Osher and Sethian, 1988), the level-set function off the interface, in general, is not a distance function which satisfies $|\nabla\phi| = 0$. Keeping the level-set function as a distance function, at least near the interface, is very important for modeling multiphase flows, because the gradient of ϕ can become large if the distance function is not preserved. It leads to a loss of accuracy. To preserve the distance function, the level-set function is reinitialized after Eq. (C.3) is solved. Sussman et al. (1994) introduced the following reinitialization equation

$$\frac{\partial\phi}{\partial\tau} + S(\phi_0)(|\nabla\phi| - 1) = 0, \tag{C.10}$$

where τ is the pseudo-time, ϕ_0 is the level-set function at the beginning of the pseudo-time, and S is the smoothed sign function. The smoothed sign function is given by

$$S(\phi_0) = \begin{cases} 1 & \phi_0 \geq \epsilon, \\ -1 & \phi_0 \leq -\epsilon, \\ \frac{\phi_0}{\epsilon} - \frac{1}{\pi}\sin(\frac{\pi\phi_0}{\epsilon}) & \text{otherwise}, \end{cases} \tag{C.11}$$

where ϵ is the same parameter used in Eq. (C.8).

The steady-state solutions of Eq. (C.10) satisfy the distance function requirement, but it does not conserve mass. A mass conserving formulation was proposed by Sussman and Fatemi (1999) by adding a mass correction term to the right-hand side of Eq. (C.10) as follows:

$$\frac{\partial\phi}{\partial\tau} + S(\phi_0)(|\nabla\phi| - 1) = \lambda\delta(\phi)\,|\nabla\phi|\,. \tag{C.12}$$

λ in Eq. (C.12) is defined as (Osher and Fedkiw, 2002)

$$\lambda_{i,j,k} = -\frac{\int_{\Omega_{i,j,k}} \delta(\phi)S(\phi_o)(1 - |\nabla\phi|)dV}{\int_{\Omega_{i,j,k}} \delta^2(\phi)|\nabla\phi|dV}, \tag{C.13}$$

where $\Omega_{i,j,k}$ denotes the volume of an individual grid cell.

The level-set method described above, which employs the smoothed interface, cannot directly account for the surface tension because the pressure is continuous across the interface. However, the surface tension can be included as the source term, H_i in Eq. (C.2), in the Navier-Stokes equations (Sussman et al., 1994) as

$$H_i = -\sigma\kappa(\phi)\delta(\phi)\frac{\partial\phi}{\partial x_i}, \tag{C.14}$$

where σ is the surface tension, and κ is the curvature defined as

$$\kappa = \nabla \cdot \left(\frac{\nabla\phi}{|\nabla\phi|}\right). \tag{C.15}$$

The spatial derivatives in Eqs. (C.14) and (C.15) are calculated by using standard second-order central differences.

C.3 Numerical solution of the Hamilton-Jacobi equation

In generalized curvilinear coordinates, Eq. (C.3) is written as

$$\frac{1}{J}\frac{\partial \phi}{\partial t} + U_k \frac{\partial \phi}{\partial \xi_k} = 0. \tag{C.16}$$

The spatial derivative term in the ξ_1 direction is discretized as

$$\left.\frac{\partial \phi}{\partial \xi_1}\right|_{i,j,k} = \frac{\phi_{i+\frac{1}{2},j,k} - \phi_{i-\frac{1}{2},j,k}}{\Delta \xi_1}. \tag{C.17}$$

$\phi_{i\pm\frac{1}{2},j,k}$ in the above equation is calculated by using a third-order WENO scheme (Jiang and Shu, 1996). $\phi_{i+\frac{1}{2},j,k}$, for instance, is computed as

$$\phi_{i+\frac{1}{2},j,k} = \frac{\alpha_1}{\alpha_1+\alpha_2}\left(\frac{\phi_C}{2} + \frac{\phi_R}{2}\right) + \frac{\alpha_2}{\alpha_1+\alpha_2}\left(-\frac{\phi_L}{2} + \frac{3\phi_C}{2}\right), \tag{C.18}$$

where

$$\alpha_1 = \frac{2}{3}\frac{1}{\left((\phi_C - \phi_R)^2 + \epsilon_0\right)^2}, \tag{C.19}$$

$$\alpha_2 = \frac{1}{3}\frac{1}{\left((\phi_L - \phi_C)^2 + \epsilon_0\right)^2}, \tag{C.20}$$

and

$$(\phi_L, \phi_C, \phi_R)_{i+\frac{1}{2},j,k} = \begin{cases} (\phi_{i-1,j,k}, \phi_{i,j,k}, \phi_{i+1,j,k}) & U_1 > 0, \\ (\phi_{i+2,j,k}, \phi_{i+1,j,k}, \phi_{i,j,k}) & U_1 \le 0. \end{cases} \tag{C.21}$$

with $\epsilon_0 = 10^{-6}$. Values of $\phi_{i-\frac{1}{2},j\pm\frac{1}{2},k\pm\frac{1}{2}}$ can be calculated in the same way, and the temporal derivative term in Eq. (C.16) can be discretized by Runge-Kutta methods.

C.4 Numerical solution of the reinitialization equation

The gradient term in Eq. (C.12) is expressed in generalized curvilinear coordinates as

$$|\nabla\phi| = \sqrt{\left(\xi_x^i \frac{\partial\phi}{\partial\xi_i}\right)^2 + \left(\xi_y^i \frac{\partial\phi}{\partial\xi_i}\right)^2 + \left(\xi_z^i \frac{\partial\phi}{\partial\xi_i}\right)^2}. \tag{C.22}$$

The spatial derivatives in the above equation are discretized by the second-order ENO scheme (Sussman et al., 1998). The numerical scheme is extended to handle generalized curvilinear coordinates in this study, and the spatial derivative in the ξ_1 direction is given by

$$\frac{\partial\phi}{\partial\xi_1} = \begin{cases} \frac{\partial\phi}{\partial\xi_1}^+ & \text{sgn}(\phi)(\phi_{i+1,j,k} - \phi_{i,j,k}) < 0 \ \text{ and} \\ & \text{sgn}(\phi)(\phi_{i,j,k} - \phi_{i-1,j,k}) < -\text{sgn}(\phi)(\phi_{i+1,j,k} - \phi_{i,j,k}), \\ \frac{\partial\phi}{\partial\xi_1}^- & \text{sgn}(\phi)(\phi_{i,j,k} - \phi_{i-1,j,k}) > 0 \ \text{ and} \\ & \text{sgn}(\phi)(\phi_{i+1,j,k} - \phi_{i,j,k}) > -\text{sgn}(\phi)(\phi_{i,j,k} - \phi_{i-1,j,k}), \\ \frac{1}{2}\left(\frac{\partial\phi}{\partial\xi_1}^+ + \frac{\partial\phi}{\partial\xi_1}^-\right) & \text{otherwise,} \end{cases} \tag{C.23}$$

where $\text{sgn}(\phi_0)$ is the sign function defined as

$$sgn(\phi_0) = \begin{cases} -1 & \phi_0 < 0, \\ 0 & \phi_0 = 0, \\ 1 & \phi_0 > 0, \end{cases} \tag{C.24}$$

and $\frac{\partial\phi}{\partial\xi_1}^+$ and $\frac{\partial\phi}{\partial\xi_1}^-$ are defined as

$$\begin{aligned} \frac{\partial\phi}{\partial\xi_1}^+ =& (\phi_{i+1,j,k} - \phi_{i,j,k}) - \frac{1}{2}M\left((\phi_{i+1,j,k} - 2\phi_{i,j,k} + \phi_{i-1,j,k}),\right. \\ & \left.(\phi_{i+2,j,k} - 2\phi_{i+1,j,k} + \phi_{i,j,k})\right), \end{aligned} \tag{C.25}$$

$$\frac{\partial \phi}{\partial \xi_1}^{-} = (\phi_{i,j,k} - \phi_{i-1,j,k}) + \frac{1}{2} M \left((\phi_{i+1,j,k} - 2\phi_{i,j,k} + \phi_{i-1,j,k}), \right.$$
$$\left. (\phi_{i,j,k} - 2\phi_{i-1,j,k} + \phi_{i-2,j,k}) \right). \tag{C.26}$$

In the above equations, M is defined by

$$M(a,b) = \begin{cases} a & |a| < |b|, \\ b & |b| \leq |a|. \end{cases} \tag{C.27}$$

Spatial derivatives in ξ_2 and ξ_3 directions are calculated in the same way as described above. A first-order backward Euler method is employed to discretize the temporal derivative in Eq. (C.12) is discretized by the first-order forward Euler scheme.

C.5 Summary of the two-phase flow level-set algorithm

The procedure for solving the two-phase flow is as follows.

1. Advect the level-set function by solving Eq. (C.3).

2. Reinitialize the level-set function by solving Eq. (C.12) (4-5 fixed number of iterations).

3. Solve the momentum equations (Eq. (2.33)).

4. Solve the Poisson equation (Eq. (2.34)).

5. Update the pressure (Eq. (2.35)).

6. Update the velocities (Eq. (2.36)).

7. If in RANS mode, solve $k-\omega$ (Eqs. (2.6) and (2.7)) or SST (Eqs. (2.9) and (2.10)) model equations.

8. Go to 1.

C.6 Free-surface modeling of nonlinear sloshing in a two-dimensional rectangular tank

To verify the accuracy of the free-surface model, a nonlinear sloshing of inviscid fluid in a two-dimensional rectangular tank is solved. The initial free-surface elevations are given as

$$\zeta(x) = d + \eta = d + a\cos(k_2 x), \tag{C.28}$$

where ζ is the free-surface elevation, η is the wave amplitude, a is the initial free-surface disturbance, b is the width of the rectangular tank, d is the mean flow depth, and $k_m = m\pi/b$. Wu and Eatock Taylor (1994) derived the analytic solution of the wave amplitude (η) up to second-order by using the perturbation expansion method. The analytic solution of the wave amplitude at the center of the tank is given by

$$\eta(\frac{b}{2}, t) = \eta_1(\frac{b}{2}, t) + \eta_2(\frac{b}{2}, t), \tag{C.29}$$

where

$$\eta_1(\frac{b}{2}, t) = a\cos(\omega_2 t)\cos(\frac{k_2 b}{2}), \tag{C.30}$$

and

$$\eta_2(\frac{b}{2}, t) = \frac{1}{8g}\left(2(\omega_2 a)^2\cos(2\omega_2 t) + \frac{a^2}{\omega_2^2}(k_2^2 g^2 + \omega_2^4) - \frac{a^2}{\omega_2^2}(k_2^2 g^2 + 3\omega_2^4)\cos(\omega_4 t)\right), \tag{C.31}$$

where g is the acceleration due to gravity, and $\omega_m = \sqrt{k_m g \tanh(k_m d)}$.

The computational domain and initial free-surface elevations are shown in Figure C.1. The contour levels denote the values of the level-set function. The width (b) of

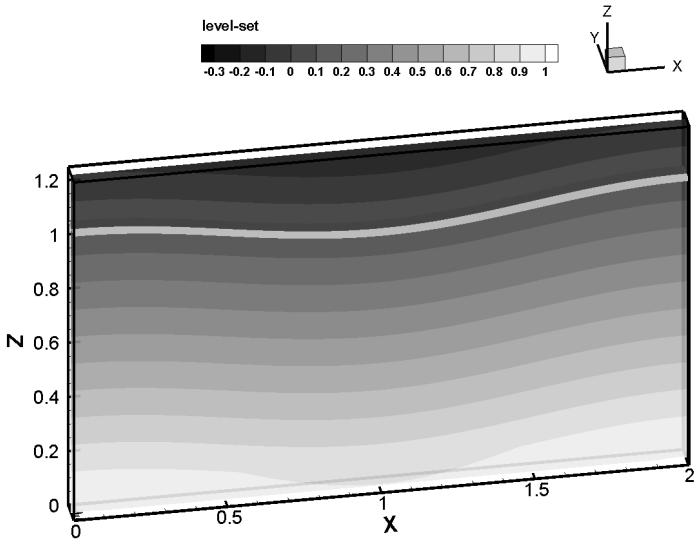

Figure C.1: The computational domain and the initial level-set function (contour levels) of the nonlinear sloshing problem (the gray surface denotes the free-surface).

the tank, the mean flow depth (d), and the initial disturbance (a) are set to 2, 1, and 0.05 respectively, and the length of the domain in the y direction is set to 0.1. The density of liquid and gas was given as 1 and 0.001, respectively. Even though this is a two-dimensional problem, it was solved using the three-dimensional code. $108 \times 11 \times 130$ computational grid points are used in x, y and z directions, respectively. The free-slip velocity boundary condition is given at $x = 0$, $x = 2$, $z = 0$ and $z = 1.2$, and the periodic boundary condition is specified in the y direction. The initial velocities are set to zero, and the acceleration due to gravity is given by $\vec{G} = (0, 0, -1)$.

Figure C.2 shows time history of the computed and analytic wave amplitude at the center of the tank. The peak value of the wave amplitude varies over cycles because of the nonlinear effect. The agreement between computed and analytic solutions is very good, and it verifies the accuracy of the present free-surface model. The volume of the liquid at times $t = 0$ and $t = 20$ is 0.2 and 0.20011, respectively. This implies an error

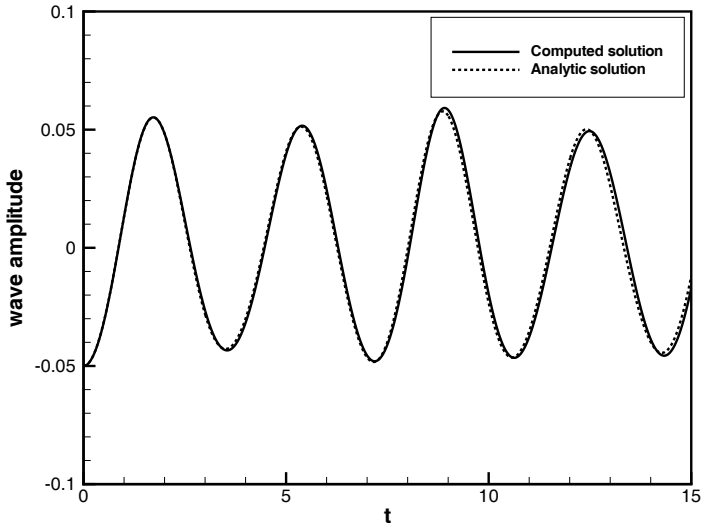

Figure C.2: Time history of computed and analytic wave amplitude at the center of the tank.

in mass conservation of about 0.05 %, which is quite satisfactory. Figure C.3 shows the computed free-surface elevations and contours of the vertical velocity at different times.

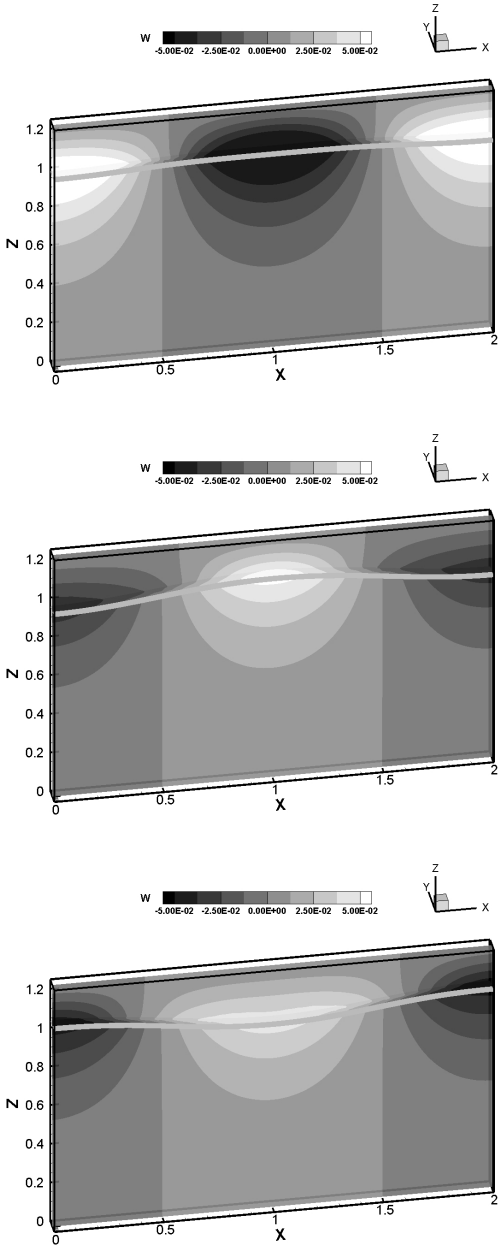

Figure C.3: Computed free-surface elevations and contours of the vertical velocity at time t=2.5 (top), 5.0 (middle) and 7.5 (bottom).

C.7 Free-surface modeling of the OSL

In this section, we apply the level-set free-surface model to carry out coupled air/water simulations for the bankfull flow condition in the OSL. The SST RANS model (see Section 2.1.2.1) is used for turbulence closure. The reason why the RANS model using coarse grids is employed in this work instead of the LES model using fine grids is because the computational cost for solving two-phase free-surface flows with the LES is more expensive.

The computational grid consists of $191 \times 51 \times 96$ cells in the streamwise, spanwise and vertical directions, respectively. The immersed body shown in Figure 4.11 is employed to handle the complex bed topography, and the wall model described in Section 2.1.3 is used to apply boundary conditions for the velocity near the solid walls. The constant water surface elevation (239.11 m) obtained from the field measurements is used to specify the level-set boundary condition at the outlet, and the zero-gradient boundary condition in the streamwise direction is employed at the inlet. The initial computational domain consists of two domains with air and water. Each phase occupies approximately half of the domain.

Figure C.4 shows the measured and computed water surface elevation. It is seen that the present model gives reasonably correct values of the water surface elevations throughout the channel compared with the measured values. The computed elevation near the inlet (239.30 m) agrees very well with the measured value, which implies that the free-surface model correctly predicts the energy slope of the water surface.

The above results suggest that the free-surface model coupled with the URANS model can effectively be used to predict water surface elevations in field scale streams with arbitrarily complex bathymetry especially when the measured water surface elevations are not available. The water surface elevation obtained from the coarse resolution URANS simulation can be used as an input for the high resolution LES or URANS

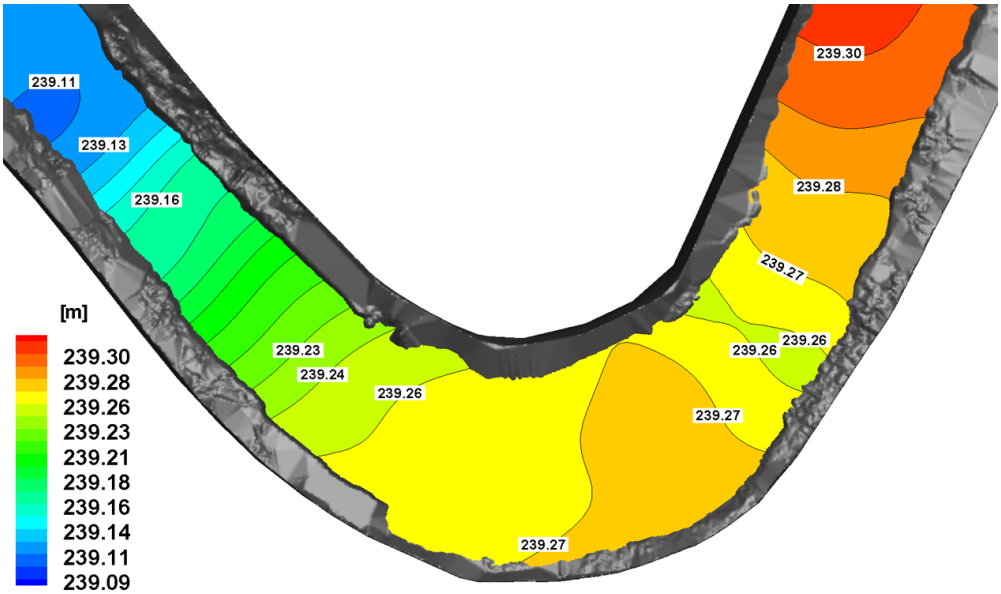

(a) Measured water surface elevations.

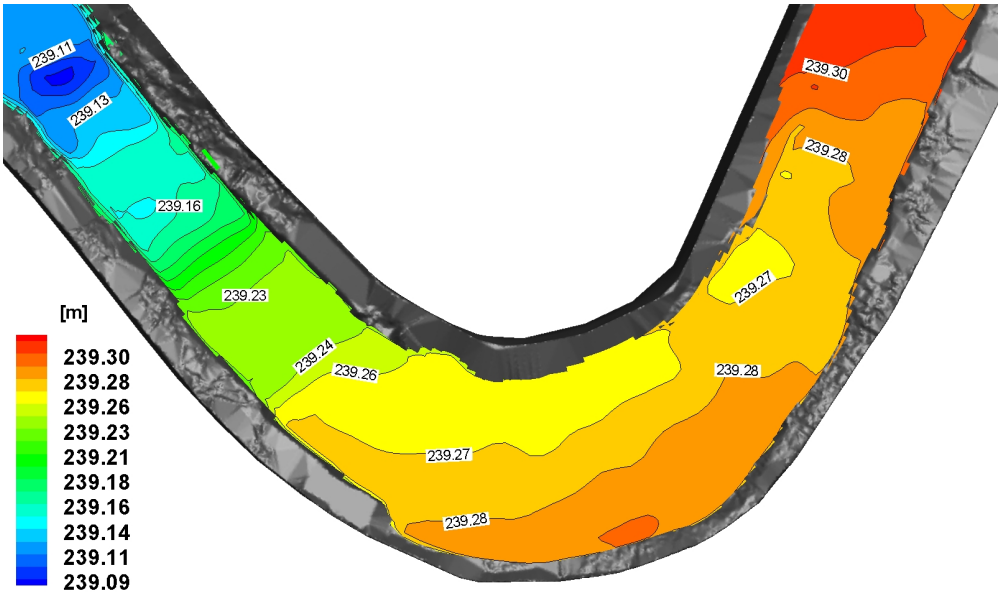

(b) Predicted water surface elevations.

Figure C.4: Measured (top) and predicted (bottom) water surface elevations of the bankfull flow (the flow direction is from right to left).

simulations.

Appendix D – Third-order WENO scheme

The governing equations for the k-ω model (Wilcox, 1988) are formulated in generalized curvilinear coordinates as follows:

$$\frac{1}{J}\frac{\partial(\rho k)}{\partial t} + \frac{\partial}{\partial \xi_j}(\rho k U_j) = \tau_{ij}\frac{\xi_j^k}{J}\frac{\partial u_i}{\partial \xi_k} - \frac{1}{J}\beta^*\rho k\omega + \frac{\partial}{\partial \xi_j}\left((\mu + \sigma^*\mu_t)\frac{g^{jk}}{J}\frac{\partial k}{\partial \xi_k}\right), \quad \text{(D.1)}$$

$$\frac{1}{J}\frac{\partial(\rho \omega)}{\partial t} + \frac{\partial}{\partial \xi_j}(\rho \omega U_j) = \alpha\frac{\rho\omega}{k}\tau_{ij}\frac{\xi_j^k}{J}\frac{\partial u_i}{\partial \xi_k} - \frac{1}{J}\beta\rho\omega^2 + \frac{\partial}{\partial \xi_j}\left((\mu + \sigma^*\mu_t)\frac{g^{jk}}{J}\frac{\partial \omega}{\partial \xi_k}\right). \quad \text{(D.2)}$$

where the closure coefficients are given as $\alpha = 5/9$, $\beta = 3/40$, $\beta^* = 9/100$, $\sigma = 1/2$, and $\sigma^* = 1/2$.

Unlike the discretization of the Navier-Stokes equations (Eq.(A.4)), the third-order WENO scheme is employed to discretize the convection terms in the above equations. The convection term in Eq. (D.1) is discretized as follows:

$$\left.\frac{\partial}{\partial \xi_j}(\rho k U_j)\right|_{i,j,k} = \left.\left(\frac{\partial}{\partial \xi_1}(\rho k U_1) + \frac{\partial}{\partial \xi_2}(\rho k U_2) + \frac{\partial}{\partial \xi_3}(\rho k U_3)\right)\right|_{i,j,k}. \quad \text{(D.3)}$$

The spatial derivative term in the ξ_1 direction is discretized as

$$\left.\frac{\partial}{\partial \xi_1}(\rho k U_1)\right|_{i,j,k} = \frac{(\rho k)_{i+\frac{1}{2},j,k}(U_1)_{i+\frac{1}{2},j,k} - (\rho k)_{i-\frac{1}{2},j,k}(U_1)_{i-\frac{1}{2},j,k}}{\Delta \xi_1} \tag{D.4}$$

In the above equation, $\phi_{i+\frac{1}{2},j,k} = (\rho k)_{i+\frac{1}{2},j,k}$ is calculated by using a third-order WENO scheme (Jiang and Shu, 1996) as follows:

$$\phi_{i+\frac{1}{2},j,k} = \frac{\alpha_1}{\alpha_1+\alpha_2}(\frac{\phi_C}{2} + \frac{\phi_R}{2}) + \frac{\alpha_2}{\alpha_1+\alpha_2}(-\frac{\phi_L}{2} + \frac{3\phi_C}{2}), \tag{D.5}$$

where

$$\alpha_1 = \frac{2}{3}\frac{1}{((\phi_C - \phi_R)^2 + \epsilon_0)^2}, \tag{D.6}$$

$$\alpha_2 = \frac{1}{3}\frac{1}{((\phi_L - \phi_C)^2 + \epsilon_0)^2}, \tag{D.7}$$

and

$$(\phi_L, \phi_C, \phi_R)_{i+\frac{1}{2},j,k} = \begin{cases} (\phi_{i-1,j,k}, \phi_{i,j,k}, \phi_{i+1,j,k}) & U_1 > 0, \\ (\phi_{i+2,j,k}, \phi_{i+1,j,k}, \phi_{i,j,k}) & U_1 \leq 0. \end{cases} \tag{D.8}$$

with $\epsilon_0 = 10^{-6}$.

The spatial derivative terms in ξ_2 and ξ_3 directions can be computed in the same manner as shown above.

Appendix E – GMRES method

The generalized minimal residual method (GMRES) developed by Saad and Schultz (1986) is an iterative method for the numerical solution of a system of linear equations. Denote the system of linear equations to be solved by

$$Ax = b, \tag{E.1}$$

where A is an invertible matrix of size $m \times m$.

The Krylov subspaces are the subspaces of the form (Saad, 2003)

$$K_m = (A, v) = span\{v, Av, A^2v, ..., A^{m-1}v\}. \tag{E.2}$$

GMRES seeks the solution of the vector $x_n \in K_m$ that minimizes the norm of the residual $Ax_m - b$.

Any vector x can be written as

$$x = x_0 + V_m y, \tag{E.3}$$

The algorithm for solving Eq. (E.1) is as follows (Saad, 2003):

1. Compute $r_0 = b - Ax_0$ (x_0 being the first trial vector), $\beta := ||r_0||_2$, and $v_1 := r_0/\beta$
2. For $j = 1, 2, ..., m$, Do
3. Compute $w_j := Av_j$

4. For $i = 1, ..., j$ Do
5. $h_{ij} := (w_j, v_i)$
6. $w_j := w_j - h_{ij} v_i$
7. EndDo
8. $h_{j+1,j} = ||w_j||_2$. If $h_{j+1,j} = 0$ set $m := j$ and go to 11
9. $v_{j+1} = w_j / h_{j+1,j}$
10. EndDo
11. Define the $(m+1) \times m$ matrix $H_m = \{h_{ij}\}_{1 \leq i \leq m+1, 1 \leq j \leq m}$
12. Compute y_m, the minimizer of $||\beta e_1 - H_m y||_2$
13. $x_m = x_0 + V_m y_m$

In the above algorithm, e_1 is the first column of the $m \times m$ identity matrix.